Dept. of Mathematics and Numerical Modeling.

TECHNICAL REPORT

Parameter Calibration Using Data Assimilation for Simulation of Forest Fire Spread

Blaise Delmotte

21 February - 21 August 2011

Supervisor:

Dr. Sophie Ricci
Global Change Research Team,
Centre Européen de Recherche et de
Formation Avancées en Calcul Scientifique
Toulouse, France

Supervisor:

Pr. Arnaud Trouvé
Dept. of Fire Protection Engineering,
University of Maryland
College Park, MD

Acknowledgments

I would like to particularly thank all my supervisors Sophie Ricci, Arnaud Trouvé, Mélanie Rochoux and Bénédicte Cuenot for their availibility, their good humor and their support. I also thank Sebastien Massart, Roberto Paoli, Albert Simeoni and Kayo Ide for their expertise and their interest in this project. I would like to compliment the staff of both CERFACS and UMD for making my paperwork efficient and my stay convenient. Thank you to my office colleagues Pierre Cayot, Pierre Damien, David Nolte, Laurent Krumenacker, Carl Dewandel, Guillaume Frichet, Zhoreh Gorbani, Vivien Lecoustre, Artur Witkowski and Sebastien Vilfayeau for the relaxing and necessary frisbee breaks. A special thank to Mélanie Rochoux who encouraged me all along this internship and who conveyed me her enthusiasm, her sense of priorities and her determination.

Thanks to all this people these internship was really pleasant and fulfilling on both professional and personal aspects.[1]

[1] PS: Waldo ("Charlie" in French) lost his way in this report...will you be able to find him ?

Abstract

The present study aims at demonstrating that some of the limitations of wildfire modeling can be overcome by coupling information coming from both observations and models using data assimilation techniques. The concept is that a data-driven fire model can lead to more accurate predictions of fire spread. This work is limited to a stand-alone numerical feasibility study with the objective of calibrating some of the parameters of a numerical model using the Best Linear Unbiased Estimator (BLUE) algorithm.

A simplified model of premixed combustion is used to simulate the evolution of a wildfire. Following a macroscopic approach, the fire front is modeled as a discontinuity between burnt and fresh vegetation through a progress variable in which the local flame speed is the main physical quantity. This formulation links the local rate of spread (ROS) with the local fuel characteristics and environmental conditions (typically local wind and slope). The front propagation is based on a front tracking method called Level Set.

The data assimilation algorithm calibrates the input parameters which are significant sources of uncertainties in the estimation of the ROS. Two different types of observations are studied: field observations of the progress variable, made at fixed spatial locations over the computational domain (e.g. measurements from fixed sensors) and front observations such as airborne or satellite pictures. The assimilation of each type of observations requires the development of a particular strategy. A comparative study indicates that front observations provide better results than field observations.

Both proposed data-driven modeling strategies appear to provide a valuable solution to the problem of integrating fire sensor and airborne observations into fire models. These strategies also correspond to an innovative application of data assimilation to the area of combustion and fire science.

Keywords: wildfire, fire modeling, CFD, data assimilation, fire forecast, flame spread.

Introduction

Scientific positioning

Each year thousands of hectares of vegetation-covered areas are burnt by forest fires caused by man or nature, endangering not only the natural environment, but also socio-economic life and quite often human life itself. The prediction of forest fire behavior is an essential component in land management and in fire hazard mitigation plans.

Forest fire spread is a complex phenomenon to model. It involves many physical and chemical processes; and the scale of modeling varies from mm, for material decomposition, to km, for atmospheric dynamics. As model fidelity is never perfect, and input parameters are sources of uncertainties, coupling observations and simulations is a good way to overcome model limitations. Jan Mandel's research ([MBB+08]) and a previous study performed by Mélanie Rochoux [Roc10] show the feasibility of data assimilation for forest fire propagation. More specifically, this internship aims at calibrating influent and/or uncertain model parameters in the determination of the rate of spread of the fire front.

This study is part of a wider project called ANR-(COSINUS project)-IDEA, developed as a collaboration between the University of Corte, CERFACS, Météo-France, the CNRS laboratory EM2C at *Ecole Centrale Paris* and the *Laboratoire d'Aérologie* at *Observatoire Midi-Pyrénées*. The global objective is to build a simulation tool of regional-scale wildland fires, coupling the fire dynamics and the atmospheric emissions (carbon, trace gases, aerosols) within an operational time frame. This internship partially focuses on the data assimilation aspects tackled by Mélanie Rochoux in her Ph.D. in the frame of the IDEA project.

This project is multidisciplinary and therefore requires collaborations between different structures and scientific communities.

Structures and collaborations

My internship is the result of a Franco-American collaboration between two structures, the *Centre Européen de Recherche et de Formation Avancée en Calcul Scientifique* (CERFACS) in Toulouse and the Department of Fire Protection Engineering at the University of Maryland (UMD). In this context, my training was divided in two parts, the first three months, from February 21 to May 21, at CERFACS and the last three months, from May 22 to August 21, at the University of Maryland.

CERFACS, computational physics and environmental sciences

The first part of my internship was supervised by Sophie Ricci, senior researcher specialized in data assimilation within the Global Change team; and Bénédicte Cuenot, group leader of the Combustion team at CERFACS. CERFACS is a research organization that aims at developing advanced methods for the numerical simulation and the algorithmic solution of large scientific and technological problems of interest for research as well as industry, and that requires access to the most powerful computers presently available. CERFACS has seven shareholders : CNES, the French Space Agency; EADS France, European Aeronautic and Defence Space Company; EDF, Electricité de France; Météo-France, the French meteorological service; ONERA, the French Aerospace Lab; SAFRAN, an international high-technology group; TOTAL, a multinational energy compagny. Approximately 115 people work at CERFACS, including more than 95 researchers and engineers.

More specifically the Global Change team focuses on understanding the world's climate variability on regional to global scales with the aim of improving climate forecasts as well as impact studies at seasonal-to-decadal time scales. Notably, part of this team is highly qualified in data assimilation; their works apply to several fields such as oceanography, nuclear cores or hydrology. But one objective is to broaden the scope of applications, for instance to fire propagation.

The Combustion team is part of a wider team focusing on Computional Fluid Dynamics led by Thierry Poinsot. This entity is involved in all problems related to aerodynamics and combustion with high performance computing, so as to apply LES[2] techniques to model turbulent flows and turbulent combustion. The AVBP[3] solver has been jointly developed by CERFACS and IFP, the French Institute of Petroleum, to perform parallel compressible LES computations, and is specifically designed to simulate industrial gas turbines, aero gas turbines, rocket engines, and laboratory burners.

[2]Large Eddy Simulation.
[3]A Virtual Burner Project.

Department of Fire Protection Engineering at UMD, fire physics and safety concerns

The second part was supervised by Arnaud Trouvé, associate professor at the Department of Fire Protection Engineering at the University of Maryland, at the border with Washington D.C, in College Park. The research team is composed of 8 faculty members and focuses on recent advances in material testing practices, fire detection, performance-based design and modeling techniques to predict fire growth, smoke movement or the response of building systems in design and fire investigation applications.

This second half of the internship was also a good opportunity to work with experts from different communities. A collaboration has been started with Albert Simeoni, Assistant Professor at the Worcester Polytechnic Institute, near Boston. Dr. Simeoni provided a new expertise in forest fires, especially about rate of spread models and fuel makeup characterization. An exterior point of view on the data assimilation techniques was provided by Kayo Ide, professor at the Department of Atmospheric and Oceanic Science, and a well-known researcher in the data assimilation community.

Because of its international dimension and the wide scope of scientific knowledge it encompasses, this internship appeared as a challenging project and as an important step in the research community.

Outline

This report is built in three parts.

The first part deals with the modeling of a fire spread at a regional scale. It first presents the approach of using a local rate of spread model as an input parameter of a front propagation model. Then it compares numerical performances of different front propagation models.

More theoretical, the second part introduces basic data assimilation concepts to describe the parameter calibration technique. Depending on the type of observation set available, two different assimilation strategies are depicted.

Then the application of the calibration technique to the fire spread model and its performances are fully described in the third part.

A conclusion summarizes the advances of this project and the short- and long- term perspectives.

Contents

Part I

Wildfire Spread Model

1 Scale of study

The macroscopic modeling scale of a wildfire varies from $100\,m^2$ to several square kilometers. From this point of view, the fire can be considered as a 1D propagating line, the interface between fresh and burnt vegetation, whose rate of spread depends on the local conditions, in a 2D domain (Figure 1).

(a) (b)

Figure 1: Forest fire macroscopic scale.

The modeling of a regional scale wildfire front requires :

1. A model to determine the local Rate Of Spread (ROS): $R(x, y)$
2. A model to propagate an interface at a given speed $R(x, y)$

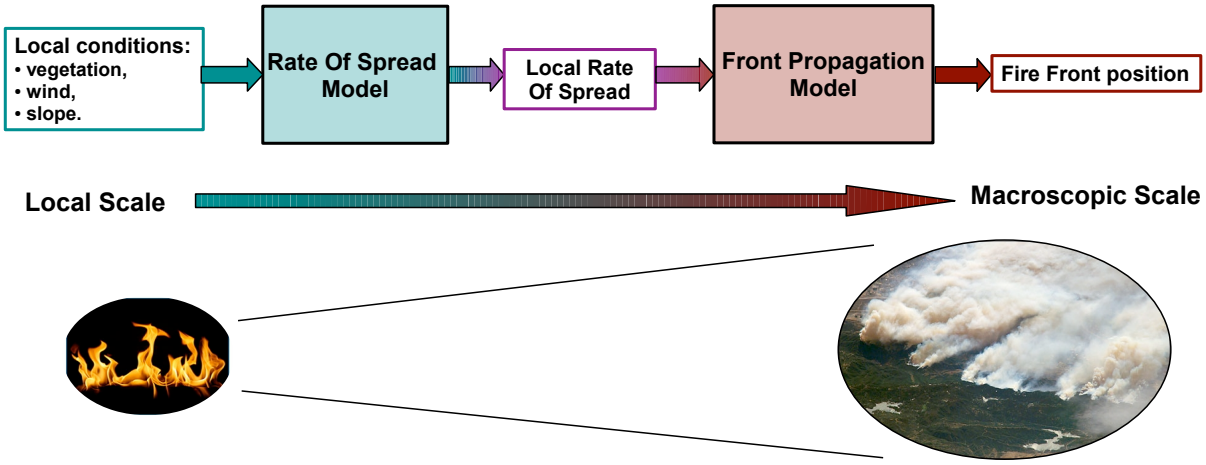

Figure 2: Steps in the wildfire spread modeling.

The understanding of fire spread models requires a prior brief description of the processes involved in this mechanism.

2 How fire spreads

Fire propagation is a complex phenomenon that involves many physical and chemical processes. This study does not aim at fully modeling the fire spread at a local scale. However a simple description given by [Fon46] helps to qualitatively understand the fire propagation mechanisms. The fire spread can be visualized as proceeding by a series of ignitions going from the burnt area to the unburnt fuel.
The ignition mechanism can be broken down into four steps (Figure 3):

1. heat is supplied from the fire to the potential fuel ahead of the fire front;
2. the surface is dehydrated;
3. further heating raises the surface temperature until the fuel begins to release combustible gases (this phase is called pyrolysis);
4. when the gas release rate from the potential fuel is sufficient to support combustion, the gas is ignited by the flame and the fire advances to a new position.

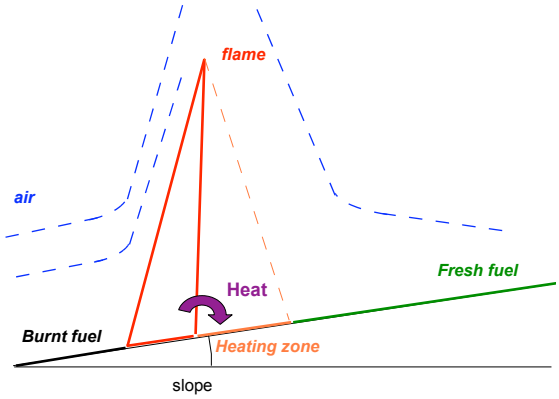

(a) 1. Heating of the potential fuel

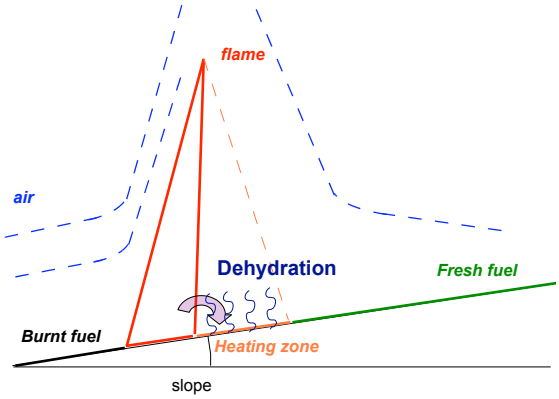

(b) 2. Dehydration of the surface

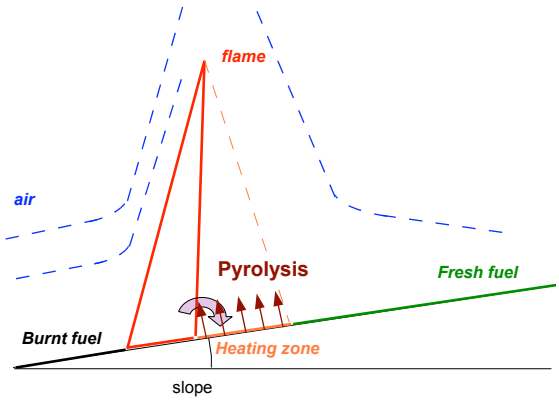

(c) 3. Pyrolysis: release of combustible gases

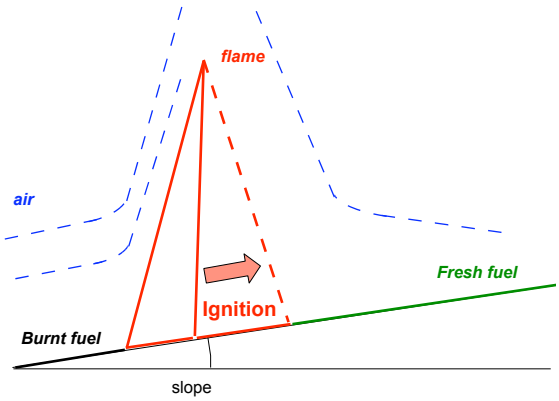

(d) 4. Ignition of the gases and advance

Figure 3: The four steps of the ignition mechanism.

This description of a fire spread is not exhaustive, but a further comprehension of this phenomenon is not necessary for this work. A detailed and didactic description of forest fire propagation mechanisms is provided in [Vie98].

3 Fire Spreads Models

The research carried out during the last fifty years on the behaviour of forest fires has led to numerous fire spread models which reflect the acquired knowledge in this domain.

A forest fire spread model is a tool to predict the local rate of spread of a fire front when spread factors are described, namely speed and direction of local wind, local slope, and vegetation properties such as: fuel structure, fuel load and fuel moisture content.

Generally, a law defines the rate of fire spread R (ROS) as a function of the wind flow velocity U, the ground slope α, the moisture content M_f, and some parameters called V_f that characterize the vegetal fuel. This law is derived according to a more or less arbitrary method:

$$R = R(U, \alpha, M_f, V_f). \tag{1}$$

Numerous modeling approaches for wildfire propagation have been developed over the years. These can be sorted into three classes [Dup97].

3.1 Classes of fire spread models

Three kinds of fire spread models can be distinguished.

1. **Empirical models**. These models provide an algebraic expression of the rate of spread (e.g. [Mac66]). The parameters introduced in the relation (1) are only set up using some experimental data in order to minimize the gap between the modeled and measured ROS. This approach is simple and computationally efficient, but the model is only valid in the range of experiments for which it was validated. Particularly, the change from laboratory to field scale experiments is not supported.

2. **Semi-empirical models** are based on a simple expression of the principle of energy conservation and require numerous laboratory experiments to determine the values of their terms. These semi-empirical models present the same characteristics of simplicity and computational efficiency as fully empirical models. They provide an algebraic expression of the rate of spread more dependent on the local conditions. They also have numerous parameters to calibrate but their main advantage over the previous model concerns their greater ability to be converted from one scale to another, because they include some relevant aspects of fire physics

3. **Physical models**. This approach is based on the numerical resolution of the conservation laws for mass, momentum, and energy in a multiphase medium formed by the vegetal fuel and the surrounding air flow (e.g. [MD04]). The large range of the time and space scales involved in this approach yields high computational costs in term of CPU time and memory storage, and some parameters in physical models are still difficult to fit. A physical model including each phenomenon (dehydration, pyrolysis, ignition,...) is currently set up by Mélanie Rochoux using accurate CFD simulations.

In the framework of parameter calibration using data assimilation, semi-empirical models are preferred for the following reasons :

- They give a good representation of the fire physics with a low computational cost.
- They have a greater ability to be converted from one scale to another than empirical models. In our case from local to macroscopic scale.
- The calibration of input or model parameters using observations can help to improve more detailed physical models.

3.2 A well-known semi-empirical model : Rothermel's model

Rothermel's model is a semi-empirical model based on a 1-D formulation of the energy balance in the fuel litter. Set up by Richard C. Rothermel in 1972 [Rot72], it is based on a mathematical formulation established by William H. Frandsen in 1971 [Fra71]. Many research have been carried out on forest fire rate of spread since Rothermel's formulation [Alb85, CGC98, FW01, BMS$^+$09]... For this feasibility study Rothermel's model appears as a good starting point as it is a reference in the fire community. It has been the basis for many works on fire spread (*op. cit.*). This study does not aim at describing Rothermel's model in details, but it intends to show how it can be interpreted and used in the framework of wildfire data assimilation.

3.2.1 The fire spread model

In this formulation, for a control volume in the unburnt region, the Rate Of Spread (ROS) along the normal direction $\overrightarrow{n}$ to the front is given by the ratio between the energy propagated to the unburnt fuel I_p and the energy necessary to ignite the fuel $\rho_b \varepsilon Q_{ig}$ [Fra71].

$$R = \frac{I_p}{\rho_b \varepsilon Q_{ig}} \tag{2}$$

with,

Symbol	Definition	Units
I_p	The propagating flux	$J.m^{-2}.s^{-1}$
Q_{ig}	Heat of preignition	$J.kg^{-1}$
ϵ	Effective heating number (amount of fuel involved in the ignition process)	-
ρ_b	Bulk density	$kg.m^{-3}$

Table 1: Rothermel's parametrization

The bulk density ρ_b is the density of the porous medium, not the density of the solid phase of the medium. It depends on the compactness of the medium.

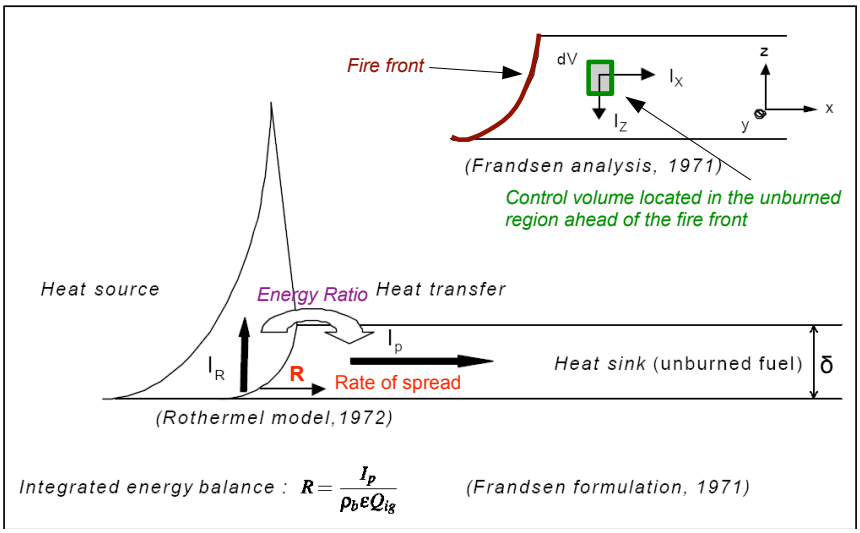

Figure 4: Principle of Rothermel's model (cf. [Dup97])

No wind, no slope conditions

In the case of no wind and no slope conditions, the propagating flux I_p can be expressed as a proportion of the reaction intensity I_R, i.e. the energy release rate of the burning gases released from the organic matter in the fuels :

$$I_p = \xi I_R \tag{3}$$

with,

ξ: the propagating flux ratio. It is the percentage of energy released by the pyrolysis which is involved in the ignition of the fresh fuel.

The ROS denoted by R_0 therefore reads

$$R_0 = \frac{\xi I_R}{\rho_b \varepsilon Q_{ig}}. \tag{4}$$

Wind and/or slope-aided fire

Wind and slope play an important role in the fire spread. To take these factor into consideration, wind and slope coefficients ϕ_w and ϕ_s are introduced. The ROS formulation becomes:

$$R = R_0 \left(1 + \phi_w + \phi_s\right) \tag{5}$$

with,
$\phi_w = f(U)$, where U is the amplitude of the wind in the normal direction to the fire front.
$\phi_s = f(\tan\varphi)$, where φ is the angle of the slope.

3.2.2 Parameters of interest

Rothermel's model do not require a prior knowledge of a fuel's burning characteristics. All that is necessary are inputs describing the physical and chemical makeup of the fuel and the environmental conditions in which it is expected to burn.

Among them, six main parameters are to be specified.

1. Four vegetation parameters:
   (a) The packing ratio:β [1], quantifies the compactness of the fuel bed.
   (b) The surface-area-to-volume ratio: σ $[m^{-1}]$, quantifies the fuel particle size involved in the ignition process.
   (c) The moisture content of the fuel bed: M_f [1], determines the heat of preignition Q_{ig} and the decrease in intensity caused by the conbustion of fuels that initially contained moisture.
   (d) The fuel depth: δ $[m]$.
2. Two environmental parameters:
   (a) The wind amplitude in the normal direction to the fire front: $U[m.s^{-1}]$.
3. A topographical parameter:
   (a) The slope: $\tan\varphi$.

By taking these six parameters as input data, Rothermel's model reads :

$$R = R\left(\beta, \sigma, M_f, \delta, U, \tan(\varphi)\right). \tag{6}$$

3.3 Rothermel's model adaptation for macroscopic scale data assimilation

In the framework of this numerical feasibility study for macroscopic-scale fire data assimilation, the fire is considered bi-dimensional and the vegetation can be represented as a heterogeneous field of fuel depth $\delta(x, y)$. In this context, Rothermel's model adaptation for macroscopic-scale fire data assimilation requires:

1. the extrapolation from a control volume to a scalar field;
2. the extrapolation of the model from 1D to 2D;
3. a simple expression of the ROS depending on commonly available fuel characteristics such as fuel depth δ.

3.3.1 2D extrapolation

Rothermel's model is valid for a control volume in the unburnt region when the wind is colinear to the normal to the front. This configuration is too restrictive for a 2D forest fire spread. Indeed a 2D extrapolation of Rothermel's formulation is necessary when considering the wind dependence. The following describes the extrapolation process from the 1D formulation to the 2D framework by adding new degrees of freedom in equation (6).

Rothermel's framework

The wind factor ϕ_w was established using 1D tunnel experiments (Figure 5). In Rothermel's model, the normal vector to the front $\vec{n}$ is supposed to be uni-directional and constant in time

$$\vec{n}(x,t) = \vec{x}.$$

In these experiments the wind was uni-directional and colinear with the normal to the fire front

$$\vec{U} = U\vec{x}.$$

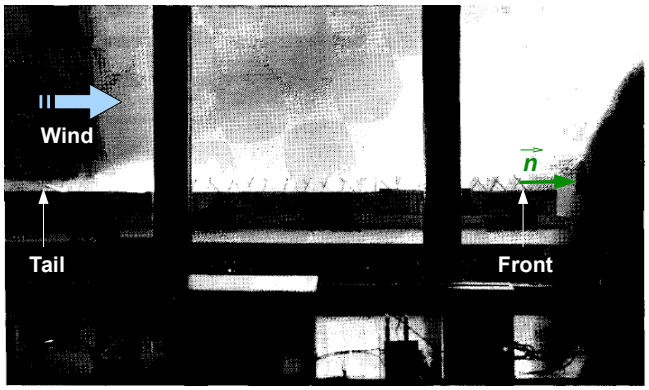

Figure 18.--Burning double tripod fuel bed in a large wind tunnel.

Figure 5: Rothermel tunnel experiment to evaluate wind dependence [Rot72].

Also, this model is valid only at the front of the fire where $\vec{n} = \vec{x}$ not at the tail where $\vec{n} = -\vec{x}$.

2D characteristics of a fire

Normal vector $\vec{n}$

Considering the topological features of a wildfire the shape of the fire front is not straight. Thus the normal vector is not constant along the front. And given that the front moves in time, the normal vector also changes in time (Figure 6). Therefore, for 2D extrapolation the normal vector to the fire front is assumed to be local, bi-directional and time dependent:

$$\vec{n}(x,y,t) = \begin{pmatrix} n_x(x,y,t) \\ n_y(x,y,t) \end{pmatrix}.$$

Wind $\vec{V}$

For the sake of simplicity, new terms need to be introduced. Let

- $\vec{V}$ be the wind vector of amplitude V;
- α be the angle between the wind vector $\vec{V}$ and the ordinate axis (Oy). On a cartesian coordinate system $\vec{V}$ reads

$$\begin{aligned} \vec{V} &= \begin{pmatrix} V_x \\ V_y \end{pmatrix} \\ &= \begin{pmatrix} V\sin\alpha \\ V\cos\alpha \end{pmatrix} \end{aligned};$$

- θ be the angle between $\vec{V}$ and the local normal vector to the front:

$$\begin{aligned}\theta(x,y,t) &= \arccos(\vec{V}.\vec{n}) \\ &= \arccos(V_x n_x + V_y n_y)\end{aligned} .$$

The rate of spread of a 2D wind aided fire highly depends on the wind but also on the topology of the fire front. According to the position along the fire front, the ROS can drastically change. At the rear, the front advances relatively slowly against the oncoming wind, since hot combustion products tend to be blown over an already burned area. At the head, the velocity is relatively large, since hot combustion products tend to be blown over a yet-to-burn area, in which discrete fuel elements are heated toward ignition by convective-conductive transfers.

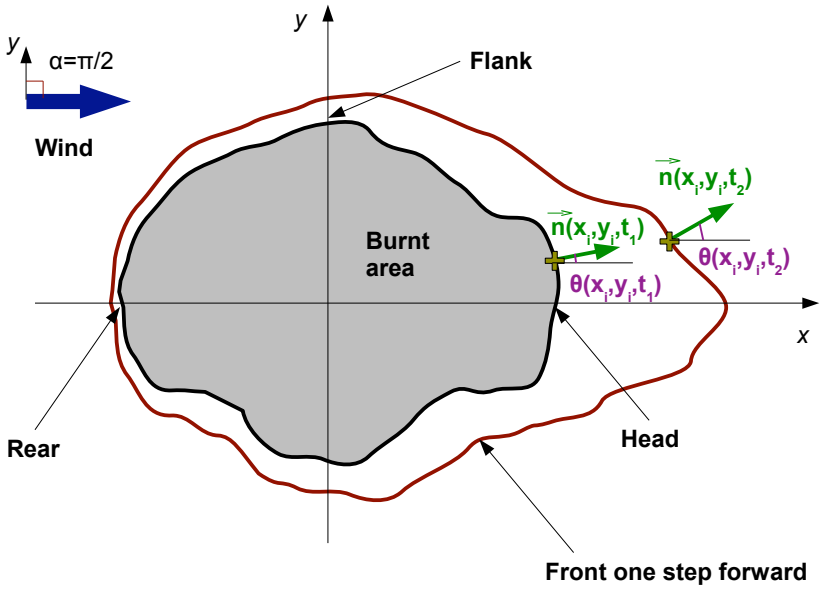

Figure 6: Wind-dependent topology of the front.

Fuel distribution

In a two dimensional configuration, the fuel depth distribution can be heterogenous $\delta = \delta(x,y)$.

New formulation of Rothermel's model

Considering the 2D requirements for extrapolation, the wind velocity in the normal direction U reads

$$U(x,y,t) = \begin{cases} \vec{V}(x,y).\vec{n}(x,y,t) & \text{, if } \vec{V}(x,y).\vec{n}(x,y,t) > 0 \text{ (tail and flank fire)} \\ 0 & \text{, if } \vec{V}(x,y).\vec{n}(x,y,t) \leq 0 \text{ (rear fire)} \end{cases} .$$

This change introduces a space- and time-dependence in the ROS formulation. Equation (6) becomes

$$R(x,y,t) = R\left(\beta, \sigma, M_f, \delta(x,y), U(x,y,t), \tan(\varphi)\right). \tag{7}$$

This new formulation models rear and flank fires as well but using a model designed exclusively for front fire. This extrapolation is just an approximation of what would be a 2D fire spread.

Further results show the limits of this extrapolation.

3.3.2 Linear dependence on the fuel depth δ

A parameter study on Rothermel's formulation shows that, *centeris paribus*, the ROS depends linearly on the fuel depth $\delta(x, y)$:

$$R(x, y, t) = \tau(x, y, t)\delta(x, y) \tag{8}$$

with,
$\tau[s^{-1}]$: the constant of proportionality,

$$\tau(x, y, t) = f\left(\beta, \sigma, M_f, U(x, y, t), \tan(\varphi)\right).$$

The function f to determine the constant of proportionality τ is given by a set of equations fully described in [Rot72].

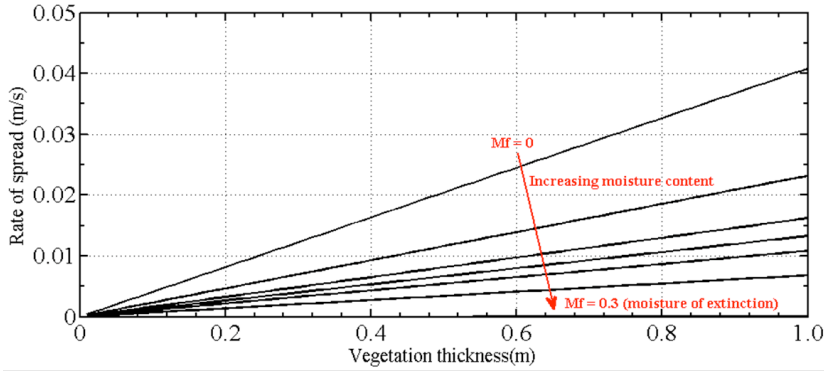

Figure 7: R as a function of δ ($R = \tau\delta$) under no-wind no-slope condition for different moisture contents M_f.

As the fuel thickness is a common vegetation feature, this linear dependence is convenient for parameter calibration. Section 9.1 shows which parameter to calibrate, depending on their influence on the ROS.

In the formulation used in this study, the fuel depth is normalized:

$$\bar{\delta}(x, y) = \frac{\delta(x, y)}{\delta_0}$$

where δ_0 is the maximum fuel depth.

As shown in this section, Rothermel's model provides the local rate of spread depending on local conditions. Then, this local rate of spread is used as an input parameter for the front propagation model.

4 Numerical model of front propagation

For simulations of systems involving flames, several strategies for computing the flame are available. If flames are much smaller than the computational domain, they are impossible to resolve numerically; then the most common approach is to model the flame as a discontinuity. This approach relies on the assumption that a wildfire exhibits, at a macroscopic scale, a topology that is similar to premixed flames [Web91]. A premixed flame is a flame in which the oxidizer has been mixed with the fuel before it reaches the flame front. This creates a thin flame front as all of the reactants are readily available.

A number of techniques dealing with infinitely thin interfaces are available in the literature. Among them are front tracking methods, known for providing better accuracy such as Level Set methods. These methods have essentially the same objective: starting with the current position of the interface and its speed of propagation, compute the position at a later time. Each method strikes a different compromise between computational cost, accuracy, development and implementation cost, and other desirable properties.

When considering the flame as an interface between burnt and fresh gases, the front can be described by a scalar reaction progress variable c (Figure 8):

- $c \geq 1^-$: the vegetation is burnt. $c = 1^-$is the side of the interface where the burnt vegetation is located.
- $0^+ \leq c \leq 1^-$: the front zone. $c = 0^+$ is the side of the interface where the fresh vegetation is located.
- $0 \leq c \leq 0^+$: the vegetation is unburnt.

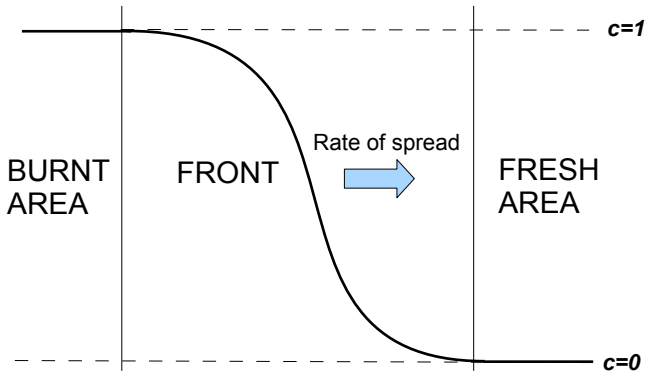

Figure 8: Progress variable c.

Two equations can describe the evolution of the scalar quantity c :

1. the diffusion-reaction equation;
2. the Level Set equation.

Considering a fire in a surface layer just above the ground, the diffusion-reaction equation reads:

$$\frac{\partial c}{\partial t} = \underbrace{D\triangle c}_{\text{diffusion}} + \underbrace{ac(1-c)}_{\text{reaction}} \tag{9}$$

with,

- $D(m^2.s^{-1})$: the diffusion coefficient;
- $a(s^{-1})$: the reaction rate.

In this model, the diffusivity D and the reaction rate a have nothing to do with the physical properties of the fire. They are artificial parameters chosen with the sole purpose of producing a desired flame speed R and front thickness δ_L. And R is given by Rothermel's model:

$$R = R(\text{fuel, wind, slope}).$$

Directly expressed with the Rate Of Spread, the Level Set equation reads

$$\frac{\partial c}{\partial t} = -\overrightarrow{R}.\overrightarrow{\nabla} c \ . \tag{10}$$

Both model are tested and then compared in terms of numerical performances in the following.

4.1 The Reaction-Diffusion equation

This part presents the former work of Mélanie Rochoux in [Roc10].

4.1.1 Study of the equation

Equation with (a, D)

The fire is modeled via a field $c(x, y, t)$ which represents a progress variable, in the geometric domain $\Omega = [0, L_1] \times [0, L_2]$, along the time window $[0; t_f]$. The reaction-diffusion equation describes how the progress variable c changes under the influence of two combined processes:

1. local chemical reactions in which the fuel is burnt and heat is released;
2. diffusion which spreads the released heat over the surface.

$$\frac{\partial c}{\partial t} = D\triangle c + ac(1-c) \tag{11}$$

with,

- $D(m^2.s^{-1})$: the diffusion coefficient;
- $a(s^{-1})$: the reaction rate.

Using Kolmogorov-Petrovsky-Piskounov (KPP) analysis $(a, D) \rightarrow (R_{KPP}, \delta_{KPP})$

This equation can be solved analytically using a KPP analysis [PV05], under the following assumptions:

1. a frozen turbulence (mean flow velocity $>>$ eddies rate of change) ;
2. a flame propagation controlled by the turbulent flame leading edge;
3. homogeneous fuel distribution.

With a frame reference attached to the flame, this analysis provides an expression for the flame speed so that R is a function of both reaction and diffusion processes. It proves indeed that the wave solution propagates at a constant speed $R_{KPP} = 2\sqrt{aD}$ and has a constant flame thickness proportional to $\delta_{KPP} = \frac{1}{2}\sqrt{\frac{D}{a}}$. Using this unique relation between (a, D) and (R_{KPP}, δ_{KPP}), equation (11) becomes:

$$\frac{\partial c}{\partial t} = R_{KPP}\delta_{KPP}\triangle c + \frac{R_{KPP}}{4\delta_{KPP}} c(1-c) \ . \tag{12}$$

Numerical adjustments

To ensure a good CFD resolution and to properly capture the front, the flame needs to be numerically thickened. The flame thickness is therefore prescribed as a numerical parameter in terms of the grid step size: typically $\delta_L = 8\Delta$, $\Delta = \min(dx, dy)$. To guarantee a constant numerical thickness a numerical parameter β is introduced. This leads to a new definition of $\delta_L = 8\beta\Delta$, with $\beta = \mathcal{O}(1/2)$.

The model of fire propagation is defined by the following PDE:

$$\frac{\partial c}{\partial t} = \left(\frac{\beta \Delta R(x,y,t)}{2}\right) \triangle c + \left(\frac{R(x,y,t)}{2\beta\Delta}\right) c(1-c) \tag{13}$$

with,

- $\Delta = \min(dx, dy)$;
- $\beta = \mathcal{O}(1/2)$;
- $R(x,y) = \tau(x,y,t)\delta(x,y)$ given by Rothermel's formulation.

Former results show that the most convenient value for the numerical correction parameter in the context of front tracking is $\beta = 1.2$. This value is fixed in the reaction diffusion model.

Macroscopic scale requirements: uniform radial velocity

The main drawback of equation (13) is that depending on the level of presence of inhomogenities in the fuel distribution, the zone in which the reaction takes place widens. It means that the flame thickness increases and that the reaction is enhanced. More heat is released and therefore the flame speed is higher than the predicted value.

At a macroscopic scale the speed is assumed to be constant through the flame. To adapt the model to any type of vegetation, keeping a constant front speed, a spatial filtering is implemented: at each time step t, all the points within the front ($0^+ < c(x,y) < 1^-$) are given a constant ROS $\bar{R}$ which is defined as $\bar{R}(t) = R(x_c(t), y_c(t))$, (x_c, y_c) representing the front position at the associated time step such that $c(x_c, y_c) = 0.5$.

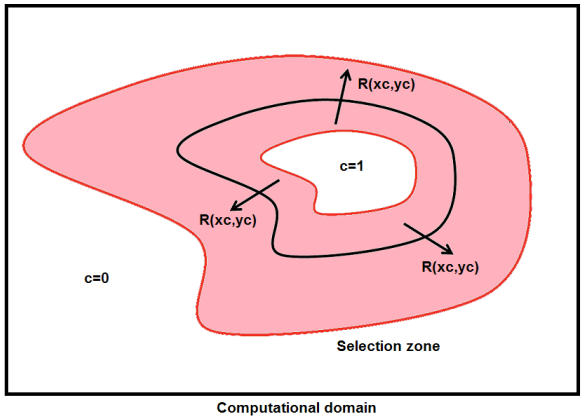

Figure 9: Spatial filtering within the fire front: if $0^+ \leq c(x,y) \leq 1^-$ then $R(x,y) = \bar{R}$.

Model formulation

The 2D fire propagation is therefore modeled by a single PDE with the progress variable c as state variable :

$$\begin{cases} \dfrac{\partial c}{\partial t} = \underbrace{\left(\dfrac{\beta\Delta\bar{R}}{2}\right)\triangle c}_{\text{diffusion}} + \underbrace{\left(\dfrac{\bar{R}}{2\beta\Delta}\right) c(1-c)}_{\text{reaction}} & ,\forall x,y \in \Omega,\ t \in [0, t_f] \\ c(x,y,0) = c_0(x,y) & ,\forall x,y \in \Omega \\ \nabla c(x,y,t) \cdot \vec{n}_{\partial\Omega}(x,y) = 0 & ,x,y \in \partial\Omega \end{cases} \tag{14}$$

with

- c: the progress variable satisfying $0 < c < 1$, with $c = 1^-$ the burnt region and $c = 0^+$ the unburnt region.

- $\bar{R}$: the rate of spread after the spatial filtering of the local rate .
- β: the thickness numerical parameter with $\beta = 1.2$.
- Δ : the grid stepsize with $\Delta = \min(dx, dy)$.
- $\partial\Omega$: the boundary of the domain Ω.
- $\vec{n}_{\partial\Omega}$: the outward-pointing normal of $\partial\Omega$.
- t_f: the simulation time.

The vegetation distribution $\delta(x, y)$ can be of any type, for instance uniform, linear or random. As to the initial condition c_0, the model sets either an initial plane at an arbitrary position $x = x_{init}$, or a circular flame of a fixed radius at the centre of the domain.

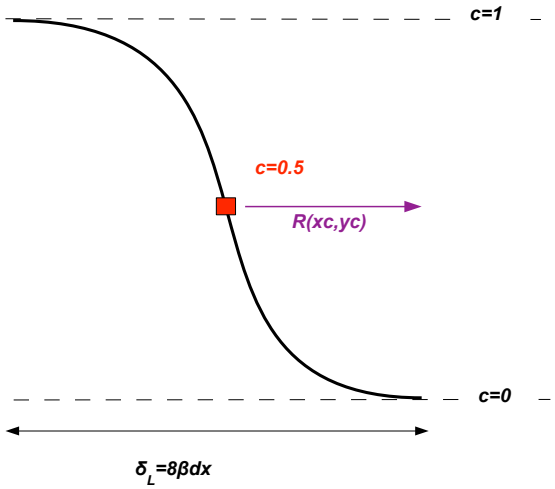

Figure 10: Fire front propagation using the filtered reaction-diffusion equation.

4.1.2 Implementation

Problem (14) is solved using a centered finite difference scheme in space and a Runge Kutta 4 integration in time.

The stability condition satisfies [Lel92]:

$$\frac{D \times dt}{\max(dx, dy)} \leq 0.725 \tag{15}$$

or equivalently:

$$\frac{\Delta\beta\bar{R}}{2} \times \frac{dt}{\max(dx, dy)} \leq 0.725 \ . \tag{16}$$

4.2 The Level-Set Method

Level-Set is a Front Tracking Method commonly used to model the evolution of a moving interface. The central idea of this method has been developed by [OS88]. Nowadays widely used in combustion [KAW88] (especially for flame capturing), computer vision [CK07], or more generally front tracking problems, Level Set has been experimented on wildland fire propagation by [MKF09, RM09] with promising results.

By considering only advection, the interface $\{c = 0.5\}$ is guaranteed, thanks to an accurate numerical integration, to propagate at the prescribed speed R. All the physics of the fire is contained in the model of R

$$R = f(\text{fuel, wind, slope}).$$

4.2.1 Formulation

The Level-Set equation describes the front propagation:

$$\begin{cases} \dfrac{\partial c}{\partial t} + \overrightarrow{R}.\overrightarrow{\nabla} c = 0 & ,\forall x, y \in \Omega,\ t \in [0, t_f] \\ c(x, y, 0) = c_0(x, y) & ,\forall x, y \in \Omega \\ \nabla c(x, y, t) \cdot \vec{n}_{\partial\Omega}(x, y) = 0 & , x, y \in \partial\Omega \end{cases} \tag{17}$$

with, $\overrightarrow{R} = R(x, y, t)\overrightarrow{n}(x, y, t) = \begin{pmatrix} R(x, y, t)n_x(x, y, t) \\ R(x, y, t)n_y(x, y, t) \end{pmatrix}$: the local ROS in the normal direction to the front, given by the extrapolated Rothermel's model.

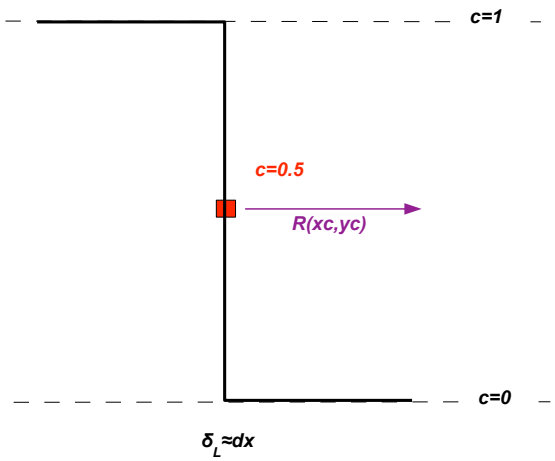

Figure 11: Fire front propagation using Level Set equation.

4.2.2 Implementation

Propagating an interface (e.g. a discontinuity) avoiding numerical diffusion or ensuring numerical stability requires a specific treatment using high order numerical schemes.

This section presents the method for solving the Level-Set equation (17) as in [RM09].

Basic steps :

1. Computation of the node-centered gradient by using a central difference:

$$\left(\frac{\delta c}{\delta x}\right)^n_{i,j} = \frac{c^n_{i+1,j} - c^n_{i-1,j}}{2dx} \tag{18}$$

$$\left(\frac{\delta c}{\delta y}\right)^n_{i,j} = \frac{c^n_{i,j+1} - c^n_{i,j-1}}{2dy} \tag{19}$$

2. Use this difference to determine the fire front unit normal vector $\overrightarrow{n}$ and compute $\overrightarrow{R}$;
3. Calculation of the monotonicity preserving gradient $\overrightarrow{\nabla} c$ with a limiter scheme (cf. next paragraph);
4. Time integration using a second order Runge Kutta scheme (RK2).

Gradient calculation : $\overrightarrow{\nabla} c$

The calculation of the gradient is similar to a flux calculation in CFD:

$$\nabla_x c = \frac{c_{east} - c_{west}}{dx} = \frac{c_{i+1/2,j} - c_{i-1/2,j}}{dx} \tag{20}$$

$$\nabla_y c = \frac{c_{north} - c_{south}}{dy} = \frac{c_{i,j+1/2} - c_{i,j-1/2}}{dy} \tag{21}$$

with,

- c_{east} : the value of c at the east face of the cell i, j.

The numerical scheme used is second order in space. A Superbee slope limiter is used to preserve monotonocity of the scalar field $c(x, y)$ [PD11]. The values at each face is given thanks to the slope and the local direction of $\overrightarrow{R}$.

1D example:

- If $R_x > 0$ then

$$c_{east} = c_{i,j} + \frac{1}{2} B(r_{i,j}) \left(c_{i+1,j} - c_{i,j}\right) \tag{22}$$

$$c_{west} = c_{i-1,j} + \frac{1}{2} B(r_{i-1,j}) \left(c_{i,j} - c_{i-1,j}\right) \tag{23}$$

with,

  - $r_{i,j} = \dfrac{c_{i,j} - c_{i-1,j}}{c_{i+1,j} - c_{i,j}}$: the ratio of successive gradients on the solution mesh;
  - $B(r_{i,j}) = \max\left(0, \min(2r_{i,j}, 1), \min(r_{i,j}, 2)\right)$: the Superbee slope limiter.

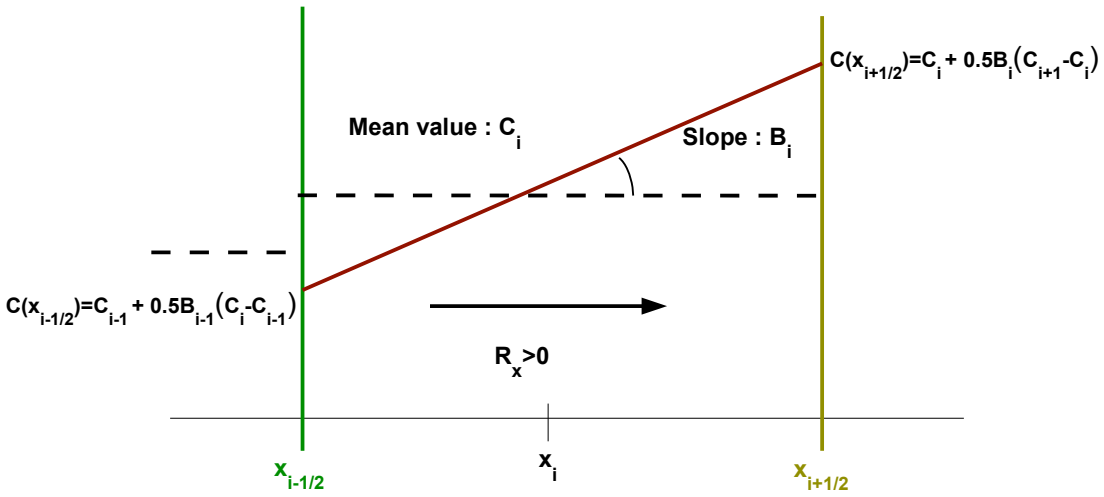

Figure 12: 1D example for second order scheme.

- If $R_x < 0$ then

$$c_{east} = c_{i+1,j} + \frac{1}{2} B(r_{i+1,j}) \left(c_{i,j} - c_{i+1,j}\right) \tag{24}$$

$$c_{west} = c_{i,j} + \frac{1}{2} B(r_{i,j}) \left(c_{i-1,j} - c_{i,j}\right) \tag{25}$$

with,

– $r_{i,j} = \dfrac{c_{i,j} - c_{i+1,j}}{c_{i-1,j} - c_{i,j}}$: the ratio of successive gradients on the solution mesh;
– $B(r_{i,j}) = \max(0, \min(2r_{i,j}, 1), \min(r_{i,j}, 2))$: the Superbee slope limiter.

Stability conditions:

Because of the accuracy of the numerical scheme in space, the CFL condition for this method is more restrictive:

$$dt\left(\frac{\max(R_x)}{dx} + \frac{\max(R_y)}{dy}\right) \leq K \tag{26}$$

The value of K has been empirically determined to be $K = 0.3$. This value ensures a systematic numerical stability. An analytical CFL condition was calculated for a similar numerical scheme (Discontinuous Galerkin, piecewise linear) with an explicit Euler time integration in [Del10] and led to the value of $K = 0.3$.

4.2.3 A Lagrangian approach to evaluate the Level Set accuracy

A Lagrangian formulation was the first approach to be chosen. Given a set of particles to describe the fire front, $\{X_i\}_{i=1,..Npart}$, the Lagrangian formulation reads

$$\frac{d\overrightarrow{X_i}}{dt} = R(\overrightarrow{X_i})\overrightarrow{n} \tag{27}$$

with,

- $\overrightarrow{X_i}$: the position of the particle i;
- $\overrightarrow{n}$: the ouwtard poiting normal vector to the front;
- $R(\overrightarrow{X_i})$: the local ROS given by Rothermel's model.

This formulation, gives a very accurate solution but it presents several drawbacks:

1. a high number of particle is necessary to model the front, especially for heterogeneous fuel distributions;
2. it requires a high-level programming to anticipate events such as:
   (a) Collisions
   (b) Decomposition of a front
   (c) Self-decomposition
   (d) Recomposition

All these events imply the suppression or addition of particles within a dynamic referenced list. This work has been done earlier by [FMB09] using object oriented programming techniques. Therefore, the Lagrangian technique has been implemented only for simple configurations such as homogeneous or linear fuel distribution. As in [RM09], the Lagrangian model was used only to to evaluate the Level Set accuracy for simple configurations.

4.3 Performances

4.3.1 Speed and thickness diagnostics

Some diagnostics on the properties of the flame, commonly used in combustion, help to evaluate the accuracy of both models for different configurations [Roc10].

Speed diagnostic

The objective is to introduce a quantity describing the front (defined by the isocontour $c = 0.5$) at a given time. This quantity is the average speed of the front, denoted by R^* and defined as the following ratio:

$$R^* = \frac{\int_{c=0.5} R dl}{\int_{c=0.5} dl} \tag{28}$$

The diagnostic for the ROS reads:

$$R_d = \frac{1}{\int_{c=0.5} dl} \frac{d}{dt} \left(\iint c(x,y) dxdy \right) \tag{29}$$

Indeed,

$$\begin{aligned}
\frac{d}{dt} \left(\iint c(x,y) dxdy \right) &= \iint \frac{\partial c(x,y)}{\partial t} dxdy \\
&= \iint \overrightarrow{R}.\overrightarrow{\nabla} c \, dxdy \\
&= \iint R\overrightarrow{n}.\overrightarrow{\nabla} c \, dxdy \\
&= \iint R \frac{\overrightarrow{\nabla} c}{\left|\overrightarrow{\nabla} c\right|}.\overrightarrow{\nabla} c \, dxdy \\
&= \iint R \left|\overrightarrow{\nabla} c\right| dxdy \\
&= \int_{c=0.5} R dl \\
&= R^* \int_{c=0.5} dl
\end{aligned}$$

with,

- $\left|\overrightarrow{\nabla} c\right| = \frac{dl}{dxdy}$: the length of the flame per unit area;
- $\int_{c=0.5} dl$: the perimeter of the isocontour $c = 0.5$.

Thickness diagnostic

The flame thickness is diagnosed by the inverse of the maximum gradient of the progress variable c:

$$\delta_{L,d} = \frac{1}{\max \left| \frac{\partial c}{\partial \overrightarrow{n}} \right|_{c=0.5}} \tag{30}$$

where $\overrightarrow{n}$ represents the normal direction to the propagation.

Even if the thickness has no physical meaning in the Level-Set formulation, it allows to evaluate the effect of numerical diffusion.

4.3.2 Reaction Diffusion vs. Level-Set

Configurations for comparison

The accuracy of each model is compared using speed and thickness diagnostics. Both model performances are compared for an initial centered circular fire of radius $r_0 = 5$ as shown on Figure 13 for three different types of fuel distribution:

1. uniform fuel distribution: $\bar{\delta}(x,y) = 1$;
2. linear fuel distribution: $\bar{\delta}(x,y) = \frac{0.2-1}{200} x + 1$;
3. random fuel distribution: $\min_{x,y \in \Omega} \bar{\delta}(x,y) = 0.1$ and $\max_{x,y \in \Omega} \bar{\delta}(x,y) = 0.8$.

For each model the integration time is $t_f = 800$ and stability conditions are respected.

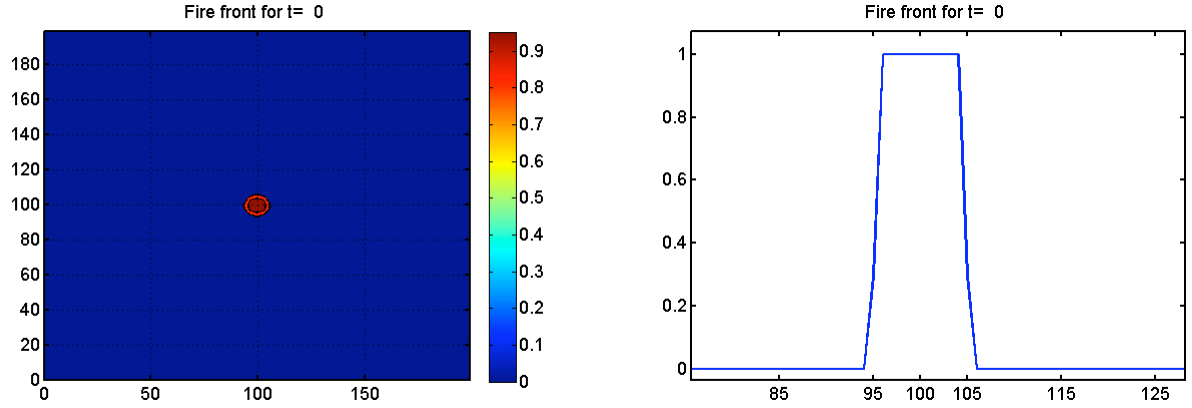

(a) Initial circular fire $c_0(x, y)$.

(b) Section of $c_0(x, y)$.

Figure 13: Initial circular fire with $r = 5$.

Comparison of performances

1. Uniform fuel distribution

Concerning the thickness diagnostic the reaction-diffusion model satisfies the condition: $\delta_L \approx 8\beta \min(dx, dy)$. The Level-Set as it is implemented restricts numerical diffusion and therefore the numerical thickness stabilizes around $\delta_L \approx 3dx$, which is thin compared to the size of the domain 200×200.

Concerning the speed diagnostic, each model sticks to the reference value $R = 0.1$. But the response time of the reaction-diffusion model $\tau_{\text{R-D}}$ is much longer than the Level-Set τ_{LVS}. By calculating the analytical radius of the fire along time

$$r(t) = r_0 + Rt$$

the discrepancies between the two models due to the response time can be compared on Figure 15.

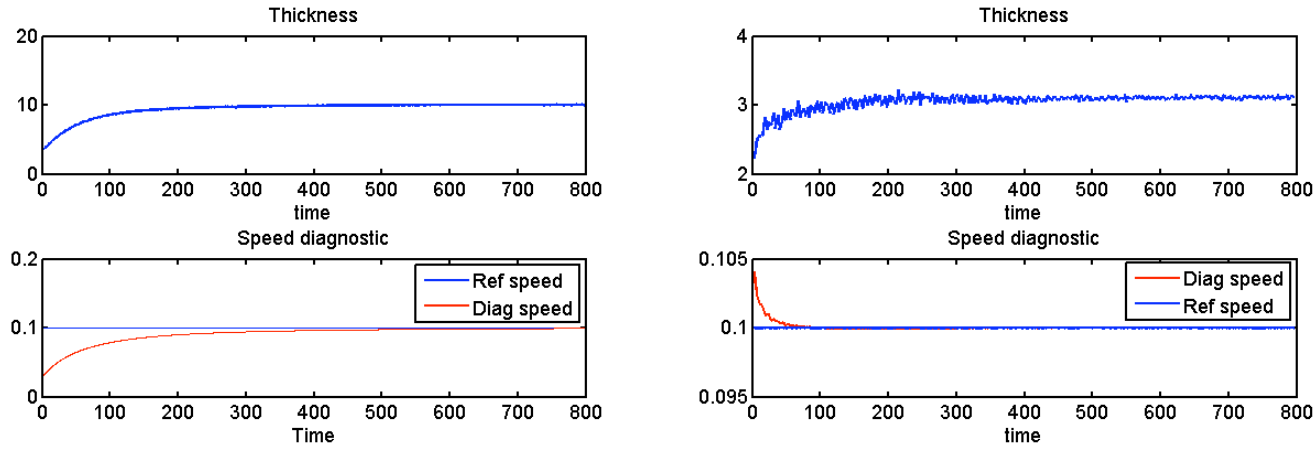

(a) Reaction Diffusion diagnostics.

(b) Level Set diagnostics.

Figure 14: Speed and thickness diagnostics for homogeneous fuel distribution.

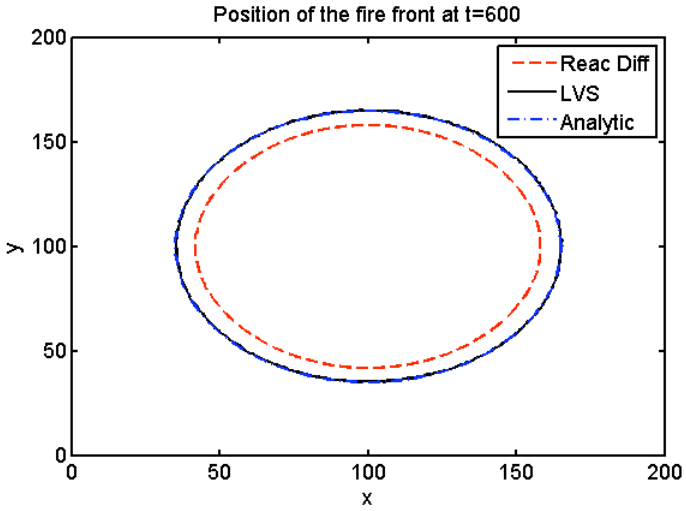

Figure 15: Numerical solutions compared with analytical solution for homogeneous fuel distribution at $t = 600$.

2. Linear fuel distribution

The thickness diagnostic is identical to uniform fuel distribution. Again, the difference in terms of response time makes the Level-Set model converge faster toward the reference value R^*.

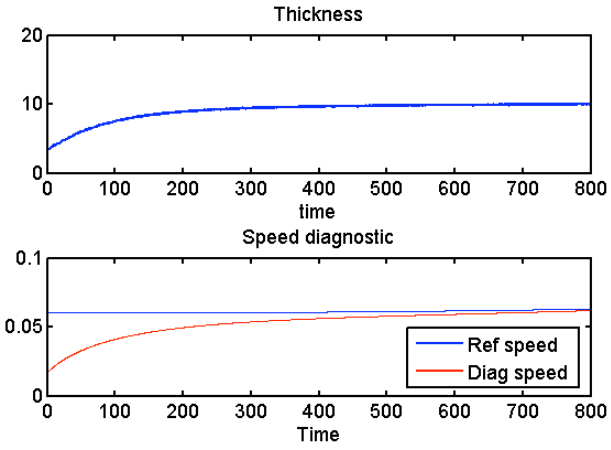

(a) Reaction Diffusion diagnostics.

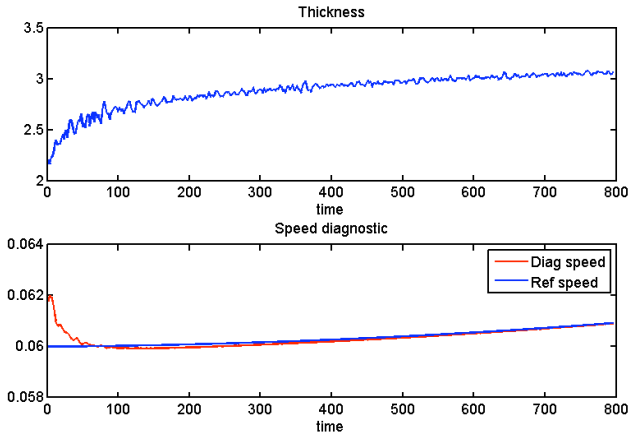

(b) Level Set diagnostics.

Figure 16: Speed and thickness diagnostics for linear fuel distribution.

3. Random fuel distribution

The conclusion is the same for a random fuel distribution.

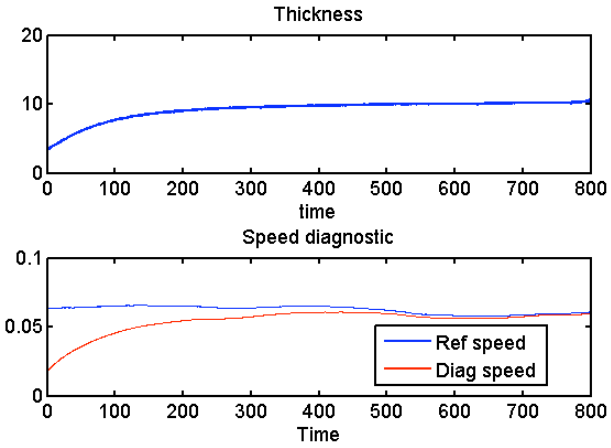

(a) Reaction Diffusion diagnostics.

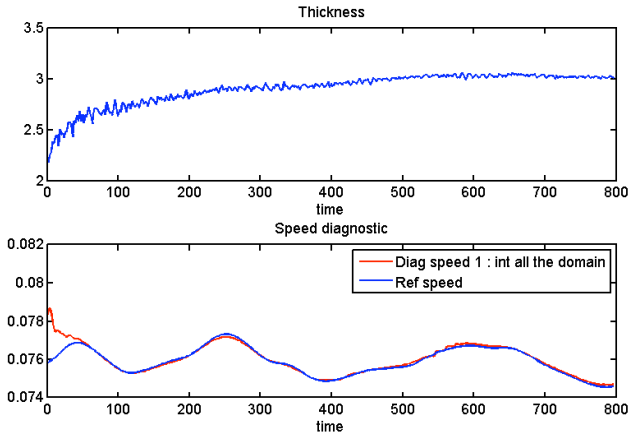

(b) Level Set diagnostics.

Figure 17: Speed and thickness diagnostics for random fuel distribution.

4.3.3 Level-Set with wind conditions

Many different configurations have been tested on the Level-Set method with wind-aided fire. The initial condition $c_0(x, y)$ is a semi-circle of radius $r_0 = 5$ at the south of the domain. The wind vector is given by

- its amplitude $V = 0.5$;
- its direction $\alpha = \widehat{(Oy, \vec{V})} = 0$rad.

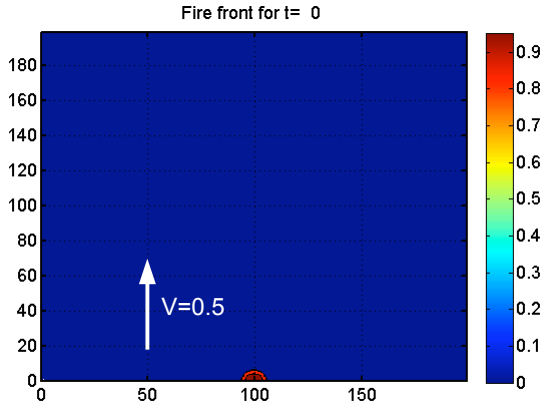

Figure 18: Initial conditions.

The initial condition $c_0(x, y)$ is different for a wind-aided fire because the 2D extrapolation of Rothermel's model is rough for rear fire propagation.

Diagnostics are computed for uniform and random fuel distribution.

1. Uniform fuel distribution

The speed sticks to the reference value. On the other hand the front thickens according to time. The thickening is not fast but for a longer simulation time attention should be paid to this phenomenon. The successive front positions show that the flank fire propagates much slower than the front. As explained previously, Rothermel's model is not designed to model this type of situation.

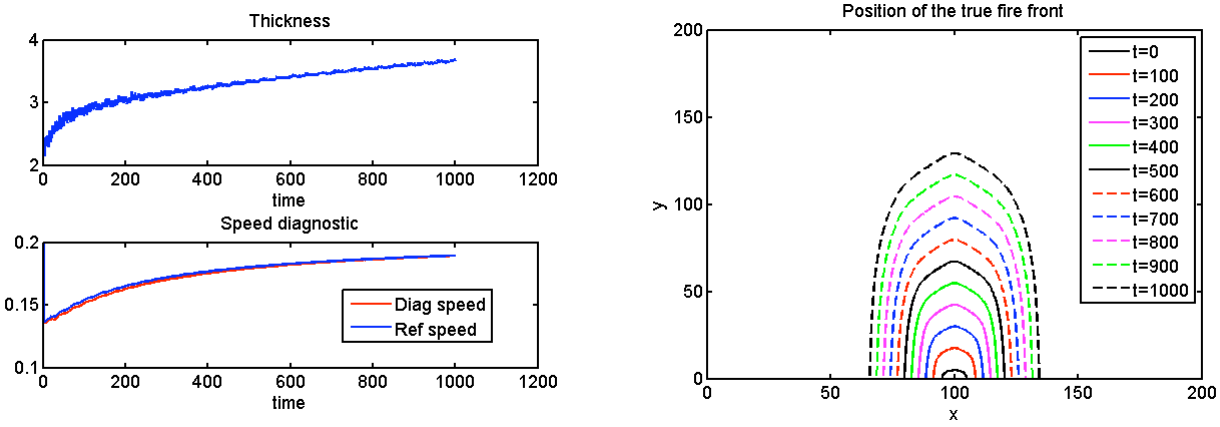

(a) Diagnostics. (b) Front position.

Figure 19: Level Set performances with wind and uniform fuel distribution.

2. Random fuel distribution

The conclusion is similar for a random fuel distribution.

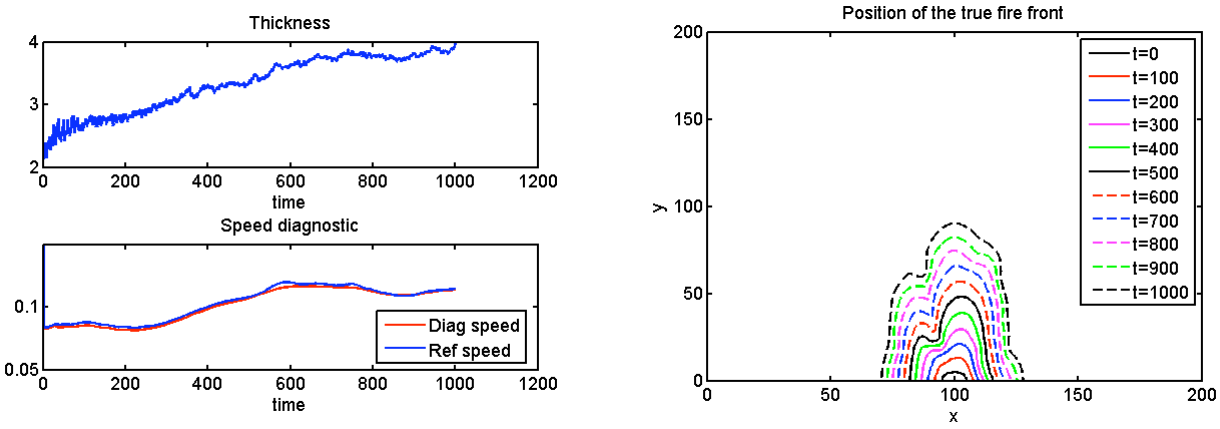

(a) Diagnostics. (b) Front position.

Figure 20: Level Set performances with wind and random fuel distribution.

Discussion

First, the Level Set response time τ_{LVS} is shorter than the reaction-diffusion $\tau_{\text{R-D}}$. A large response time can be problematic when modeling phenomenon whose characteristic time is shorter. Notably if the time of fire spread is shorter than $\tau_{\text{R-D}}$, the reaction-diffusion model will not be able to provide an accurate numerical solution. That is why the Level-Set model provides a more accurate solution in terms of propagation speed.

Secondly, the Level-Set solution method requires a high computational cost. But it does not require a numerical correction like ROS filtering ($\bar{R}$) or thickness control (β) for heterogeneous fuel distributions. Therefore Level-Set and reaction-diffusion solutions are equivalently costly.

Thirdly, Level-Set methods are well-known and used in the litterature whereas the ROS filtering was not enough mature to overcome the problem of front thickening, and introduced some inaccuracies.

To conclude, the Level-Set equation appears to be more adapted for fire spread at a macroscopic scale as it provides a more precise numerical solution.

Part II

Data Assimilation Concepts for Parameter Calibration

Introduction

Before introducing some data assimilation concepts for parameter calibration, it is necessary to understand the usefulness of this method.

Why data assimilation ?

For such a complex phenomenon as forest fire spread, numerical simulations present several sources of errors. First physical models cannot represent all the phenomena involved in the wildfire spread. This lack of fidelity is an important factor in the discrepancies between the real and the modeled fire front. Second, input parameters of the model are not perfectly known. They are sources of uncertainties in the rate of spread determination. Lastly, semi-empirical models are designed with experimentally calibrated parameters. These model parameters are valid for a limited range of configurations. This limited validity is also a source of errors.

These model limitations can be reduced coupling simulations with real observations thanks to data assimilation.

This approach matches Richard Rothermel predictions in his reference article "A Mathematical Model For Predicting Fire Spread in Wildland Fuels" in 1972 [Rot72], *"A method for forecasting the behavior of a specific fire eventually will be developed; most likely, it will be patterned on a probability basis similar to that used for forecasting weather."*.

What is data assimilation ?

Data assimilation optimally combines all sources of information on a system to produce a more realistic image of its control parameters than if either were taken separately [BC99, ICGL97, Kal03]. The benefit of this technique has already been greatly demonstrated in meteorology [PD92, RJK+00] and oceanography [BV06] over the past decades, especially for providing initial conditions for numerical forecast. Data assimilation is now being applied with increasing frequency to other application fields (such as nuclear physics, hydrology [TMM+10] or compartment fires [Jah10]). It provides therefore an efficient framework to reduce the uncertainty on the dynamics of a system. More specifically in this study, the most uncertain or influent Rothermel's model parameters are calibrated by evaluating the distance between observations and simulations.

To sum up, the parameter calibration using data assimilation provides:

1. a better fitness of Rothermel's model parameters;
2. a better estimate of the front positions.

5 Basic concepts in data assimilation

Data assimilation combines numerical and observational information on a system in order to provide a better description of it. While measures are most of the time imperfect and sparse in space and time, the model provides extensive data of the approximated solution of the physical problem, but its parameters are not precisely known and time and spatial discretizations induce consistency errors. So both observations and model are subject to uncertainties.

So the main objective of data assimilation is to obtain the optimal value of the "real" state of the model, called **analysis**, thanks to the **observations** (measures) and to the estimation of model parameters (**background**), considering their inaccuracy.

A brief description of data assimilation concepts in the framework of parameter calibration is presented [Roc10].

5.1 The data assimilation variables

5.1.1 The control vector: $\mathbf{X}$

In the context of parameter calibration, the control vector is a set of n parameters, defining the control space. It is an approximation of a reference, known as the **true control vector** $\mathbf{X}^t$, which represents the true values of these n parameters which are, in reality, completely unknown. Data assimilation aims at determining an optimal value of the control vector, called the **analysis** and denoted by $\mathbf{X}^a$ which is closer to $\mathbf{X}^t$ than the a priori value of the control vector $\mathbf{X}^b$, called the background. The background can be a prior estimation of the model parameters thanks to previous experiments, such as semi-empirical model parameters.

5.1.2 The observation vector: $\mathbf{Y}^o$

Even though they may be sparse in time and space, observations of the system give additional information on the dynamics of the system. Gathered in one vector $\mathbf{Y}^0$ of length p, they represent, measurements of a given quantity. They may help to integrate more physical features of the true solution which are not modeled without data assimilation.

5.1.3 Background information: $\mathbf{X}^b$

The information that can be used to produce the analysis is a collection of observed values provided by observations of the true state. In the case of parameter calibration, the model parameters should not reach any aberrant value just to stick to the observations. In order to make the analysis problem more "physical", it is necessary to rely on some background information $\mathbf{X}^b$, an a priori estimate of the model parameters before application of data assimilation ; it is similar to a "first guess" of the model parameters.

5.1.4 The observation operator: H

As model parameters and observational information need to be combined in the course of data assimilation, an operator H mapping a parameter from the control space onto the observation space is required. This observation operator is generally non-linear as a composition of a model integration M (from model parameters to state variables) and of a selection process S (from grid points to observational points). The formulation of the observation operator mostly depends on the type of observations available. To simplify, let assume that is just the composition of the model M and a selection operator S. H is defined by equation (31).

$$H(\mathbf{X}) = S\left(M(\mathbf{X})\right) \ . \tag{31}$$

In practice, measurements are not perfect and the determination of H implies some assumptions. They are therefore subject to uncertainties, denoted by ϵ^0.

Since H is not available analytically, an approximation is computed. So the formulation of the calibration algorithm requires therefore the linearization of H, denoted by $\mathbf{H}$ which is identified as the Jacobian matrix in the first order Taylor expansion of H in the vicinity of a reference value of the control vector $\mathbf{X}^g$ (usually the background $\mathbf{X}^b$):

$$H(\mathbf{X}^g + \delta\mathbf{X}^g) = H(\mathbf{X}^g) + \left.\frac{\partial H}{\partial \mathbf{X}}\right|_{\mathbf{X}^g} \delta\mathbf{X} + O\left((\delta\mathbf{X})^2\right) \tag{32}$$

with $\lim_{\delta \mathbf{X} \to 0} O\left((\delta \mathbf{X})^2\right) \ (\delta \mathbf{X})^{-2} = 0$.

Hence,

$$\mathbf{H} = \left. \frac{\partial H}{\partial \mathbf{X}} \right|_{\mathbf{X}^g} . \tag{33}$$

Numerically $\mathbf{H}$ is calculated using a non-centered finite difference method and reads

$$\mathbf{H} = \frac{H(\mathbf{X}^g + \delta \mathbf{X}) - H(\mathbf{X}^g)}{\delta \mathbf{X}} \tag{34}$$

$\mathbf{H}$ is called the linear tangent of H.

5.1.5 Innovation vector

The innovation vector measures the discrepancies between the observation vector and the background projection in the observation space .

$$\mathbf{d}^{ob} = \mathbf{Y}^0 - H(\mathbf{X}^b) \ . \tag{35}$$

5.2 The modeling of the errors

As the true control vector $\mathbf{X}^t$ is unknown, the error on the background $\mathbf{X}^b$, denoted by ϵ^b, and on the observations $\mathbf{Y}^0$, denoted by ϵ^0, are also unknown. As a consequence, the background and observation error covariance matrices, denoted by $\mathbf{B}$ and $\mathbf{R}$ respectively, can only be estimated using an error covariance model.

The modeling of the errors is performed using statistics. If a large number of experiments were undergone under exactly the same conditions, the associated errors would be different each time, but statistics such as expectation value and variance could be established. These two first statistical moments would then converge to values which depend only on the physical processes responsible for the errors, and no longer on any particular realization of these errors. So a statistical model may appear as the reasonable process to approach the errors present in the system.

The best information about the distribution of these errors is given by the Probability Density Function (PDF) function. It describes the relative likelihood for these errors to occur at a given point in the control or observation space, and gives information on their expectation value and variance. This PDF is modeled by a Gaussian function.

5.2.1 Background errors

The background error ϵ^b is defined as the difference between the background $\mathbf{X}^b$ and the true control vector $\mathbf{X}^t$ with $\epsilon^b = \mathbf{X}^b - \mathbf{X}^t$. The statistics of ϵ^b are described in a square symmetric, positive definite matrix $\mathbf{B}$ of size $n \times n$, such that:

$$\mathbf{B} = \mathbb{E}[\epsilon^b \cdot (\epsilon^b)^T] \tag{36}$$

where the diagonal elements of $\mathbf{B}$ represent the error variance for each control parameter, while the off-diagonal terms stand for the covariances between the errors. This means that if $n = 1$, $\mathbf{B}$ is a scalar and is fully described by the variance associated to the single control parameter considered.

As the background errors are assumed to be unbiased,

$$\epsilon^b \sim \mathcal{N}(0, \mathbf{B}) \ . \tag{37}$$

5.2.2 Observation errors

As to the background, the observations are represented by a random variable $\mathbf{Y}^0$ that is assumed to follow a Gaussian distribution $\mathcal{N}(H(\mathbf{X}^t), \mathbf{R})$ (provided that $H(\mathbf{X}^t)$ is a non-random variable) with the error covariance matrix

$$\mathbf{R} = \mathbb{E}[\epsilon^o \cdot (\epsilon^o)^T] \ . \tag{38}$$

As the observation error is defined as the difference between the observations and the true control vector projected onto the observation space such that $\mathbf{Y}^o = H(\mathbf{X}^t) + \epsilon^o$, assuming it is unbiased and uncorrelated, ϵ^0 follows a Gaussian distribution

$$\epsilon^o \sim \mathcal{N}(0, \mathbf{R}) \tag{39}$$

Furthermore, observed quantities are not necessarily the same as the control variables. The transformations required to map one variable from the control space onto the observation space do not change the analysis problem, only its representation. However, they insert some unvavoidable errors due to the conversion between the observed values and their equivalents in the model state (independently from the observation and background errors), called the representativeness errors. They will not be considered in this case study.

5.3 Data assimilation and inverse modelling

Data assimilation provides more realistic physical fields by integrating observations and the physical expertise through a numerical model.

In this context, errors are limited to observations and background. Both follow a Gaussian distribution with a zero average and a specified covariance matrix. The resolution of the data assimilation problem requires therefore four components:

- observations of the physical system $\mathbf{Y}^o$ and their associated errors (ϵ^o, $\mathbf{R}$),
- a background estimation of the control vector $\mathbf{X}^b$ and its associated errors (ϵ^b, $\mathbf{B}$),
- a model M describing the system dynamics,
- an observation operator H with its associated linear tangent operator $\mathbf{H}$.

This defines an **inverse problem** [Tar87]: given $\mathbf{Y}^o$ and $\mathbf{X}^b$, the goal is to approximate as best as possible the true control vector $\mathbf{X}^t$ satisfying

$$\begin{array}{rcl} \mathbf{Y}^o & = & H(\mathbf{X}^t) + \epsilon^o \\ \mathbf{X}^b & = & \mathbf{X}^t + \epsilon^b \end{array} \quad . \tag{40}$$

6 Parameter calibration method: the Best Linear Unbiased Estimator

By estimating uncertainties on the background and the observations, data assimilation gives an unbiased estimation of the analysis $\mathbf{X}^a$ and minimizes the distance with the true control vector $\mathbf{X}^t$. The BLUE algorithm formulates the analysis as a linear combination of the background $\mathbf{X}^b$ and of the observations $\mathbf{Y}^o$ such that

$$\mathbf{X}^a = \mathbf{L}\mathbf{X}^b + \mathbf{K}\mathbf{Y}^o \tag{41}$$

with $\mathbf{K}$ the gain matrix and $\mathbf{L}$ a linear operator.

This way, the analysis $\mathbf{X}^a$ approximates the true state $\mathbf{X}^t$.

6.1 The BLUE formulation as a background correction

The BLUE algorithm relies on two major assumptions:

1. The background and observation errors are unbiased.
2. The observation operator is linear: it is equal to its first order Taylor expansion in the vicinity of $\mathbf{X}^b$:

$$H(\mathbf{X}) = H_{Taylor}(\mathbf{X}) = H(\mathbf{X}^b) + \mathbf{H}(\mathbf{X} - \mathbf{X}^b)$$

, with $\mathbf{H} = \frac{\partial H}{\partial \mathbf{X}}\big|_{\mathbf{X}^b}$.

Using these assumptions, the linear combination (41) can be written as a background correction, as it will be shown in the following.
From Section 5 the data assimilation variables read:

$$\begin{array}{rcl} \mathbf{X}^b &=& \mathbf{X}^t + \epsilon^b \\ \mathbf{Y}^t &=& H_{Taylor}(\mathbf{X}^t) \\ \mathbf{Y}^o &=& \mathbf{Y}^t + \epsilon^o \\ \mathbf{X}^a &=& \mathbf{X}^t + \epsilon^a \end{array} \tag{42}$$

with ϵ^b, ϵ^o and ϵ^a respectively the background, observation and analysis errors, and $\mathbf{Y}^t$ the true trajectory projected onto the observation space. The background and observation errors are assumed to be unbiased, i.e. $\mathbb{E}[\epsilon^o] = 0$ and $\mathbb{E}[\epsilon^b] = 0$.

By injecting equations (42) in equation (41) it leads to [Ric04] :

$$\begin{array}{rl} \mathbf{X}^t + \epsilon^a & = \mathbf{L}\mathbf{X}^t + \mathbf{L}\epsilon^b + \mathbf{K}\mathbf{Y}^t + \mathbf{K}\epsilon^o \\ & = \mathbf{L}\mathbf{X}^t + \mathbf{L}\epsilon^b + \mathbf{K}H_{Taylor}(\mathbf{X}^t) + \mathbf{K}\epsilon^o \end{array} \tag{43}$$

The BLUE estimator $\mathbf{X}^a$ is also unbiased ($\mathbb{E}[\epsilon^a] = 0$), so taking the expectation value of $\mathbf{X}^t + \epsilon^a$ in Equation (43) leads to:

$$\mathbb{E}[\mathbf{x}^t] = \mathbf{L}\mathbb{E}[\mathbf{X}^t] + \mathbf{K}H_{Taylor}\mathbb{E}[\mathbf{X}^t] \tag{44}$$

Hence

$$\mathbf{L} = \mathbf{I} - \mathbf{K}H_{Taylor} \tag{45}$$

and Equation (41) reads therefore

$$\mathbf{X}^a = \mathbf{X}^b + \mathbf{K}\left(\mathbf{Y}^o - H_{Taylor}\mathbf{X}^b\right) \tag{46}$$

So, the analysis can be considered as a correction of the background with an analysis increment $\delta\mathbf{X}^a = \mathbf{K}(\mathbf{Y}^o - H_{Taylor}\mathbf{X}^b) = \mathbf{K}\mathbf{d}^{ob}$, with

- $\mathbf{K}$: the gain matrix (see [Ric04] for its calculation),

$$\mathbf{K} = \left(\mathbf{B}^{-1} + \mathbf{H}^T\mathbf{R}^{-1}\mathbf{H}\right)^{-1}\mathbf{H}^T\mathbf{R}^{-1} = \mathbf{B}\mathbf{H}^T\left(\mathbf{H}\mathbf{B}\mathbf{H}^T + \mathbf{R}\right)^{-1} \tag{47}$$

- $\mathbf{d}^{ob} = \mathbf{Y}^o - H_{Taylor}\mathbf{X}^b$: the innovation vector.

A perfect confidence in the backgound $\mathbf{X}^b$ leads to a zero matrix $\mathbf{B}$ and therefore a zero matrix $\mathbf{K}$ by equation (47). In this context the assimilation correction is zero and $\mathbf{X}^a = \mathbf{X}^b$. Conversely, if the confidence is total in the observations, $\mathbf{R}$ is a zero matrix and then $\mathbf{K} = \mathbf{H}^{-1}$ by equation (47). Thus Equation (41) becomes

$$\mathbf{X}^a = \left(\mathbf{I} - \mathbf{H}^{-1}H_{Taylor}\right)\mathbf{X}^b + \mathbf{H}^{-1}\mathbf{Y}^o = \mathbf{H}^{-1}\mathbf{Y}^o$$

So in this case, $\mathbf{X}^a$ is directly the solution of the inverse problem $\mathbf{HX} = \mathbf{Y}^o$.

.

6.2 The analysis residual

The gain matrix $\mathbf{K}$ provides a posteriori the analysis error covariance matrix $\mathbf{A}$, assuming that both background and observations errors are non-correlated. $\mathbf{A}$ reads

$$\mathbf{A} = \mathbb{E}[\epsilon^a \cdot (\epsilon^a)^T] = (\mathbf{I} - \mathbf{K}H_{Taylor})\mathbf{B} \tag{48}$$

As equation (48) shows, if H_{Taylor} is of full rank (e.g., $\text{rank}(H_{Taylor}) = \min(n, p)$), then $\mathbf{A} \leq \mathbf{B}$, meaning that the BLUE algorithm reduces the error variance of the control variables.

The BLUE formulation can also be tackled with the minimization problem resulting from a data assimilation process [BC99]

6.3 The 3DVAR formulation

The resolution of most data assimilation algorithms relies on the minimization of a cost function J_{3DVAR} (variational approach referred to as $3DVAR$) defined in equation (49). This cost function measures the statistically weighted square difference between the background and the control vector on the one hand, the observations and the equivalent of the control vector in the observation space on the other hand :

$$J_{3DVAR}(\mathbf{X}) = \frac{1}{2}\left(\mathbf{X} - \mathbf{X}^b\right)^T \mathbf{B}^{-1}\left(\mathbf{X} - \mathbf{X}^b\right) + \frac{1}{2}\left(\mathbf{Y}^o - H(\mathbf{X})\right)^T \mathbf{R}^{-1}\left(\mathbf{Y}^o - H(\mathbf{X})\right) \tag{49}$$

with H the non-linear observation operator, whose linearization in the vicinity of $\mathbf{X}^b$ is denoted H_{Taylor} so that $H_{Taylor}(\mathbf{X}) = H(\mathbf{X}^b) + \mathbf{H}(\mathbf{X} - \mathbf{X}^b)$, with $\mathbf{H} = \frac{\partial H}{\partial \mathbf{X}}\big|_{\mathbf{X}^b}$.

The minimization of this cost function consists in finding the optimal "compromise" between the background and the observations depending on their precision ($\mathbf{B}^{-1}$ and $\mathbf{R}^{-1}$ respectively).
The gradient of J_{3DVAR} reads:

$$\nabla J_{3DVAR}(\mathbf{X}) = \mathbf{B}^{-1}\left(\mathbf{X} - \mathbf{X}^b\right) + \mathbf{H}^T\mathbf{R}^{-1}\left(\mathbf{Y}^o - H(\mathbf{X})\right)$$

The objective of data assimilation is to find $\mathbf{X}^a = \arg\min\left(J_{3DVAR}(\mathbf{X})\right)$ or equivalently :

$$\nabla J_{3DVAR}(\mathbf{X}^a) = 0 \tag{50}$$

$$\Rightarrow \mathbf{B}^{-1}\left(\mathbf{X}^a - \mathbf{X}^b\right) + \mathbf{H}^T\mathbf{R}^{-1}\left(\mathbf{Y}^o - H(\mathbf{X}^a)\right) = 0 \tag{51}$$

J_{3DVAR} is not quadratic because H is not linear. Therefore, the 3DVAR approach requires the use of a minimizor that implies the evaluation of the cost function and its gradient at each iteration, whereas the BLUE algorithm aims at calculating a solution to this problem using a linearity assumption.

6.4 Equivalence between BLUE and 3DVAR under the linearity assumption

In order to find a solution to the minimization problem (50) the BLUE formulation requires a linearization of the observation operator H (cf. Section 5.1.4).
If H is considered linear, it is equal to its first order Taylor expansion in the vicinity of $\mathbf{X}^b$:

$$H_{Taylor}(\mathbf{X}) = H(\mathbf{X}^b) + \mathbf{H}(\mathbf{X} - \mathbf{X}^b)$$

By injecting $H(\mathbf{X}) = H_{Taylor}(\mathbf{X})$ in equation (49), the quadratic cost function the BLUE minimizes reads:

$$J_{BLUE}(\mathbf{X}) = \frac{1}{2}\left(\mathbf{X} - \mathbf{X}^b\right)^T \mathbf{B}^{-1}\left(\mathbf{X} - \mathbf{X}^b\right) + \frac{1}{2}\left(\mathbf{Y}^o - H(\mathbf{X}^b) - \mathbf{H}(\mathbf{X} - \mathbf{X}^b)\right)^T \mathbf{R}^{-1}\left(\mathbf{Y}^o - H(\mathbf{X}^b) - \mathbf{H}(\mathbf{X} - \mathbf{X}^b)\right) \tag{52}$$

Thus, equation (51) becomes :

$$\begin{array}{rcl} 0 & = & \mathbf{B}^{-1}\left(\mathbf{X}^a - \mathbf{X}^b\right) - \mathbf{H}^T\mathbf{R}^{-1}\left(\mathbf{Y}^o - H(\mathbf{X}^b) + \mathbf{H}\left(\mathbf{X}^a - \mathbf{X}^b\right)\right) \\ \Rightarrow \mathbf{X}^a & = & \mathbf{X}^b + \left(\mathbf{B}^{-1} + \mathbf{H}^T\mathbf{R}^{-1}\mathbf{H}\right)^{-1}\mathbf{H}^T\mathbf{R}^{-1}\left(\mathbf{Y}^o - H(\mathbf{X}^b)\right) \\ \Rightarrow \mathbf{X}^a & = & \mathbf{X}^b + \mathbf{K}\left(\mathbf{Y}^o - H(\mathbf{X}^b)\right) \end{array} \tag{53}$$

$$\Rightarrow \mathbf{X}^a = \mathbf{X}^b + \mathbf{K}\mathbf{d}^{ob} \tag{54}$$

So, if H is linear, equation (50) leads directly to equation (54) which is exactly the same as equation (46).

Consequently, **the 3DVAR and BLUE approaches are equivalent if H is linear** [BC99].

6.5 Which of 3DVAR and BLUE is the most appropriate method ?

In the case of data assimilation when calibrating only a few parameters, the BLUE approach is more efficient than 3DVAR. Calculating an analytic solution using a linear approximation is indeed less costly **[Ric04]** than the evaluation of the cost function and its gradient at each iteration.

However, when the number of control variables increases and/or the observation operator H is highly non-linear, 3DVAR direct minimization may be less costly and/or more precise in the definition of the minimum of J_{3DVAR}.

6.6 External loops : analysis as an iterative process

6.6.1 Why using external loops ?

When using the BLUE approach to calibrate the parameter of a model, the solution can be distorted depending on the level of non-linearity of the observation operator. If the cost function J_{3DVAR} is not quadratic in the vicinity of the observation operator linearization point, $\mathbf{X}^g$, the minimum of J_{BLUE} and J_{3DVAR} will not coincide (cf. Figure 21). This can lead to over-corrections of the background value. In this case, it is helpful to calculate the analysis as an iterative process to converge on a solution $\mathbf{X}^a$ close to $\arg\min J_{3DVAR}$.

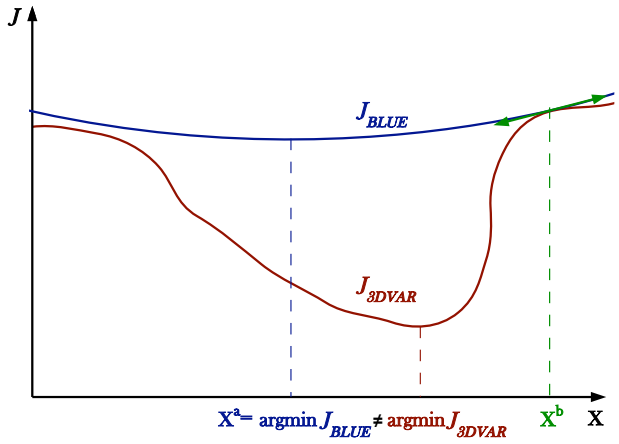

Figure 21: Discrepancies in the solution due to non-linearities of H lead to an over-correction of the background $\mathbf{X}^b$.

In this configuration, the analysis results from a succession of corrections on the background. This reasoning is equivalent to the calculation of a succession of gradients in the $3DVAR$ approach. For each iteration $\mathbf{H}$ is updated at a new reference control parameter which is the analysis of the previous iteration, and a new increment $\delta\mathbf{X}^a$ is calculated. The convergence of this iterative process is ensured by a criterion η on the relative distance between two successive analysis.

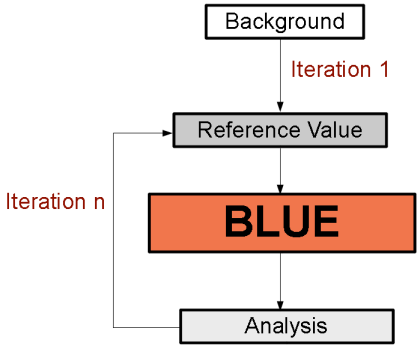

Figure 22: Simplified schematic external loop algorithm.

6.6.2 Algorithm

The process is fully described in the following algorithm (Figure 22 and Figure 23).

1. Determination of the true trajectory $M(\mathbf{X}^t)$.
2. Modeling of the observation error covariance matrix $\mathbf{R}$.
3. Modeling of the background error covariance matrice $\mathbf{B}$.
4. Construction of the observations $\mathbf{Y}^0$, directly extracted from the true state.
5. Determination of the background trajectory $M(\mathbf{X}^b)$ and projection onto the observation space: $H(\mathbf{X}^b)$.
6. Start of external loops: ***while*** $\dfrac{\left\|\mathbf{X}_i^a - \mathbf{X}_{i-1}^a\right\|_2}{\left\|\mathbf{X}_{i-1}^a\right\|_2} = \dfrac{\left\|\delta\mathbf{X}^a\right\|_2}{\left\|\mathbf{X}_{i-1}^a\right\|_2} < \eta$
   (a) Determination of the reference control vector $\mathbf{X}^g$:

i. -at iteration 1, $\mathbf{X}^g = \mathbf{X}^b$.

ii. -for all other iterations, $\mathbf{X}^g = \mathbf{X}^a_{i-1}$.

(b) Determination of the reference trajectory $M(\mathbf{X}^g)$ and projection onto the observation space: $H(\mathbf{X}^g)$.

(c) Determination of the new "innovation vector" : $\mathbf{d}^{og} = \mathbf{Y}^o - H(\mathbf{X}^g)$.

(d) Construction of the tangent linear of the observation operator $\mathbf{H} = \frac{\partial H}{\partial \mathbf{X}}|_{\mathbf{X}^g}$ in the vicinity of the reference control parameter $\mathbf{X}^g$.

(e) BLUE provides a new analysis $\mathbf{X}^a_i$.

(f) Integration of the analysed trajectory $M(\mathbf{X}^a_i)$.

7. End of external loops.

Attention must be paid in **Point 6.(e)** [Thu10]:

By taking $\mathbf{X}^g = \mathbf{X}^a$, the formulation of the BLUE differs from the "classical" one. It can be demonstrated by starting with the incremental cost function formulation :

$$J^i_{BLUE}(\mathbf{X}, \mathbf{X}^g) = \frac{1}{2}\left(\mathbf{X} - \mathbf{X}^b\right)^T \mathbf{B}^{-1}\left(\mathbf{X} - \mathbf{X}^b\right) + \frac{1}{2}\left(\mathbf{Y}^o - H(\mathbf{X}^g) - \mathbf{H}(\mathbf{X} - \mathbf{X}^g)\right)^T \mathbf{R}^{-1}\left(\mathbf{Y}^o - H(\mathbf{X}^g) - \mathbf{H}(\mathbf{X} - \mathbf{X}^g)\right) \tag{55}$$

Given that $\mathbf{X}^a = \arg\min\left(J^i_{BLUE}\right)$, it follows

$$\frac{\partial J^i_{BLUE}}{\partial \mathbf{X}}(\mathbf{X}^a, \mathbf{X}^g) = 0 \tag{56}$$

$$\Rightarrow \mathbf{B}^{-1}\left(\mathbf{X}^a - \mathbf{X}^b\right) - \mathbf{H}^T\mathbf{R}^{-1}\left(\mathbf{Y}^0 - H(\mathbf{X}^g) - \mathbf{H}(\mathbf{X}^a - \mathbf{X}^g)\right) = 0$$

Using the same calculation as in Section 6.4 the new analysis reads:

$$\Rightarrow \mathbf{X}^a = \mathbf{X}^b + \mathbf{K}\left(\mathbf{d}^{og} + \mathbf{H}(\mathbf{X}^g - \mathbf{X}^b)\right) \tag{57}$$

with $\mathbf{d}^{og} = \mathbf{Y}^0 - H(\mathbf{X}^g)$ the difference between the observation vector and the projection of the reference control vector onto the observation space.

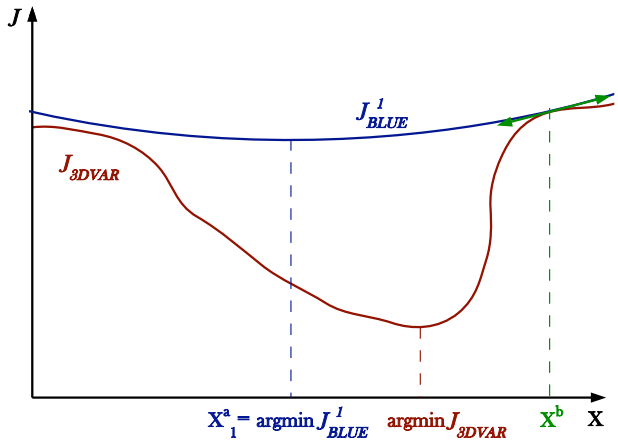

(a) First BLUE minimization $\rightarrow \mathbf{X}^a_1$

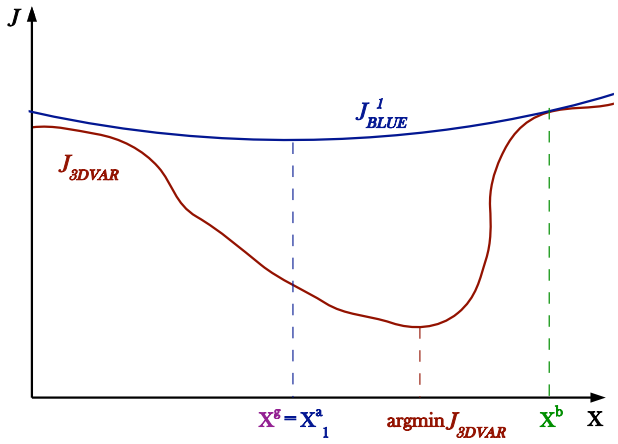

(b) New reference for linearization: $\mathbf{X}^g = \mathbf{X}^a_1$

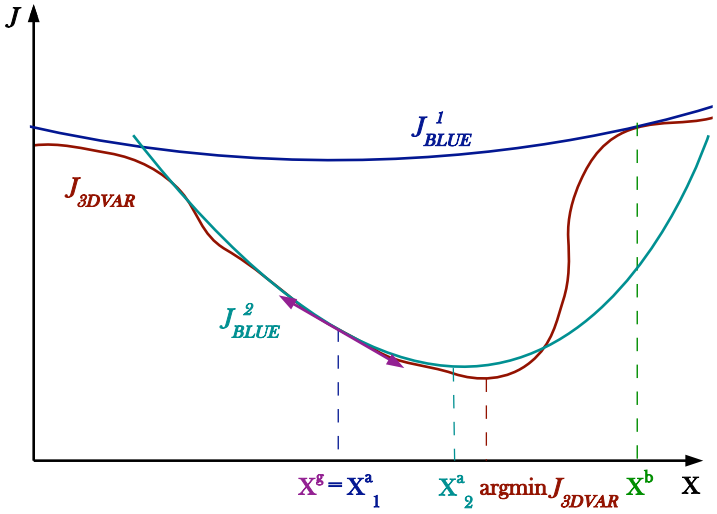

(c) Second BLUE minimization $\rightarrow \mathbf{X}^a_2$

Figure 23: Example for two iterations and one parameter ($\mathbf{X}$ is a scalar, $n = 1$). The distance between $\mathbf{X}^a$ and $\arg\min J_{3DVAR}$ is reduced.

6.7 Cost function behavior

As shown previously, the cost function J_{3DVAR} can be decomposed in two components. One in the control parameter space, denoted by J^b_{3DVAR}, involving the background value $\mathbf{X}^b$ and the variable parameter $\mathbf{X}$. The other in the observation space, denoted by J^o_{3DVAR}, involving the observation vector $\mathbf{Y}^o$ and the projection of the variable $\mathbf{X}$ in the observation space $H(\mathbf{X}^b)$.

$$J_{3DVAR}(\mathbf{X}) = \underbrace{\frac{1}{2}\left(\mathbf{X}-\mathbf{X}^b\right)^T \mathbf{B}^{-1}\left(\mathbf{X}-\mathbf{X}^b\right)}_{J^b_{3DVAR}} + \underbrace{\frac{1}{2}\left(\mathbf{Y}^o - H(\mathbf{X})\right)^T \mathbf{R}^{-1}\left(\mathbf{Y}^o - H(\mathbf{X})\right)}_{J^o_{3DVAR}} \tag{58}$$

Depending on the respective values of the uncertainties $\mathbf{B}$, $\mathbf{R}$ and the distances $\mathbf{X}-\mathbf{X}^b$ and $\mathbf{Y}^o - H(\mathbf{X})$, one component can predominate on the other.
For example, when observations are numerous ($p > n$) and are granted a higher confidence than the background ($\sigma_o \ll \sigma_b$), the terms of the observation error covariance matrix $\mathbf{R}$ are very small. So $\mathbf{R}^{-1} \gg \mathbf{B}^{-1}$ and therefore

J^o_{3DVAR} is predominant:

$$p > n,\ \sigma_o \ll \sigma_b \Rightarrow J^o_{3DVAR} \gg J^b_{3DVAR}$$

On the contrary if, observations are sparse and poor, the term J^b_{3DVAR} is predominant.

6.8 A diagnostic on observation contribution for analysis: the Degree of Freedom for Signal

Introduced in [Rab05], the Degree of Freedom for Signal (DFS) is a useful diagnostic to determine the quantity of information provided by a whole set of observations. More precisely, this quantity diagnoses the contribution of a set of observations k on the reduction of the error variance in the analysis. For a given observation set k, DFS_k reads

$$\mathrm{DFS}_k = Tr\left(\mathbf{A}\mathbf{H}_k^T\mathbf{R}_k^{-1}\mathbf{H}_k\right) \tag{59}$$

where,

- $\mathbf{A}$ is the analysis error covariance matrix. $\mathbf{A}$ is a square matrix $n \times n$.
- $\mathbf{H}_k$ is the extraction of the linear tangent of $H(\mathbf{X})$ at observation points associated to k. $\mathbf{H}_k$ is a $p_k \times n$ matrix, where p_k is the number of observations contained in k.
- $\mathbf{R}_k$ is the extracted observation error covariance matrix. $\mathbf{R}_k$ is a square matrix $p_k \times p_k$.

If $p_k = p$, the DFS reads

$$\mathrm{DFS} = Tr\left(\mathbf{A}\mathbf{H}^T\mathbf{R}^{-1}\mathbf{H}\right)$$

If observation errors are not correlated, the matrix $\mathbf{R}$ is diagonal:

$$\mathbf{R} = \begin{bmatrix} \sigma_o^2 & & \\ & \ddots & \\ & & \sigma_o^2 \end{bmatrix} = \sigma_o^2\mathbf{I}_p$$

and its inverse $\mathbf{R}^{-1}$ reads

$$\mathbf{R}^{-1} = \frac{1}{\sigma_o^2}\mathbf{I}_p$$

In this case the DFS for an observation set is defined as

$$\begin{aligned} \mathrm{DFS}_k &= Tr\left(\mathbf{A}\mathbf{H}_k^T\mathbf{R}_k^{-1}\mathbf{H}_k\right) \\ &= \frac{1}{\sigma_o^2}Tr\left(\mathbf{A}\mathbf{H}_k^T\mathbf{I}_{p_k}\mathbf{H}_k\right) \\ &= \frac{1}{\sigma_o^2}Tr\left(\mathbf{A}\mathbf{H}_k^T\mathbf{H}_k\right) \end{aligned}$$

Therefore the DFS can also be computed for each observation point of the set k: $(\mathbf{Y}^o_k(i))_{i=1,\ldots,p_k}$

$$\mathrm{DFS}^i_k = \frac{1}{\sigma_o^2}Tr\left(\mathbf{A}\mathbf{H}_k^T(1:n,i)\mathbf{H}_k(i,1:n)\right) \tag{60}$$

It quantifies their contribution to the assimilation system with respect to their position and to their observation time.

Further results show that the DFS is a powerful tool to measure which observations carry the most important information on the fire dynamics.

7 Data assimilation framework

7.1 Context

This study mainly aims at evaluating the numerical feasibility of a data assimilation methodology for parameter calibration. The objectives of parameter calibration are

1. to improve the model forecast;
2. to calibrate model input parameters to test and improve the model itself.

As a first step toward the validation of the data assimilation methodology, the goal is to grant observations a high level of confidence to show that the data assimilation algorithm converges toward the true solution (i.e the true control vector $\mathbf{X}^t$). This classical framework for validation is called Observation System Simulation Experiments. The second part of this section depicts how the data assimilation can be applied depending on the type of observations available. It reveals that the formulation of observation operator can drastically differ with the type of observations.

7.1.1 Observation System Simulation Experiments: a validation framework

In the context of Observation System Simulation Experiments (OSSE), the observations are synthesized through the numerical model itself. This configuration is designed for validation of the calibration algorithm as:

- the true value of the control parameter $\mathbf{X}^t$ is known;
- background and observation errors (resp. σ_b and σ_o) are perfectly controlled;
- the quality of the BLUE correction can be precisely quantified with a large panel of data assimilation diagnostics.

OSSE as a validation process

OSSE can be divided into several steps, from the choice of input parameters, to calibration and result analysis (Figure 24):

1. Input parameters $\mathbf{X}^t$, σ_b and σ_o are chosen by the experimenter. σ_b and σ_o directly define the error covariance matrixes:
   (a) $\mathbf{B} = \sigma_b^2$;
   (b) $\mathbf{R} = \sigma_o^2$.
2. The background $\mathbf{X}^b$ is defined as a perturbation of $\mathbf{X}^t$, in agreement with σ_b:
$$\begin{aligned} \mathbf{X}^b &= \mathbf{X}^t + \sigma_b \\ &= \mathbf{X}^t(1+\alpha_b) \end{aligned}$$
   where α_b defines a percentage of the true value: $\sigma_b = \alpha_b \times \mathbf{X}^t$.
3. Integration and projection of the background trajectory in the observation space: $H(\mathbf{X}^b)$ (and its linear tangent $\mathbf{H}$).
4. Integration and projection of the true trajectory in the observation space: $H(\mathbf{X}^t)$. Addition of a gaussian noise $\epsilon^0 \sim \mathcal{N}(0, \mathbf{R})$ to obtain the synthetized observations $\mathbf{Y}^o$:
$$\mathbf{Y}^o = H(\mathbf{X}^t) + \epsilon^o$$
   More details about noise addition are given in Section 7.2.3 and Section 7.3.4.
5. Calculation of the innovation vector:
$$\mathbf{d} = \mathbf{Y}^o - H(\mathbf{X}^b)$$

6. Once the required components ($\mathbf{R}, \mathbf{X}^b, \mathbf{B}, \mathbf{d}$ and $\mathbf{H}$) are calculated, the BLUE algorithm can be applied to obtain the analysis value $\mathbf{X}^a$ and its error covariance matrix $\mathbf{A}$.

7. Then, the objective is to compare the resulting analysis to the true state with various diagnostics in order to evaluate the optimality of the solution and the robustness of the algorithm.

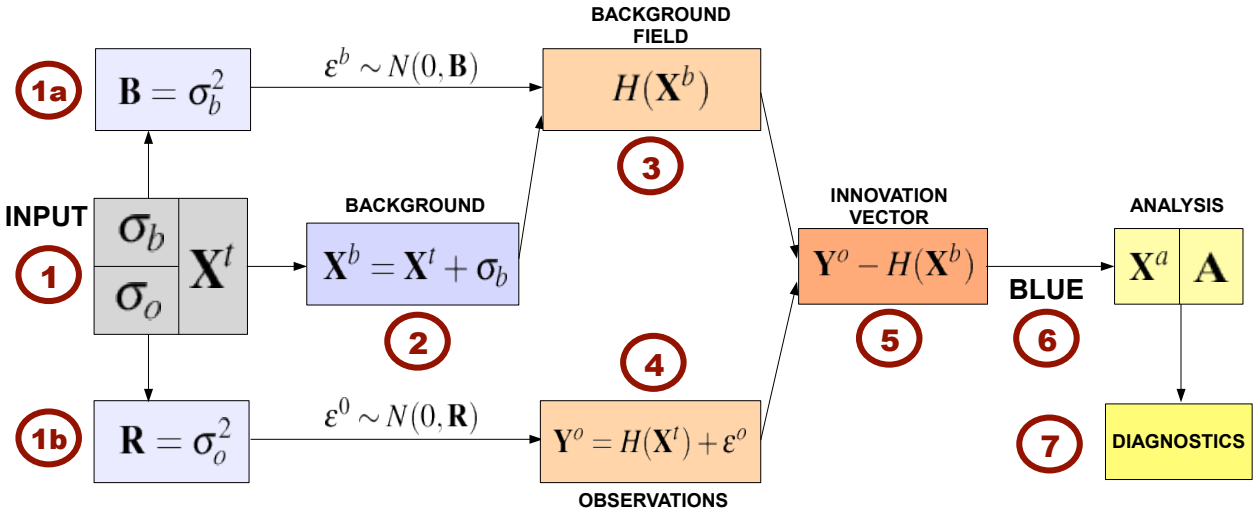

Figure 24: Schematic representation of OSSE.

7.1.2 Diagnostics for validation

In the control parameter space

If the observations are granted a high level of confidence $\mathbf{X}^t = \arg\min J_{3DVAR}$. Provided that the observation operator is linear, the analysis is in the interval $\left[\mathbf{X}^b, \mathbf{X}^t\right]$ and $\mathbf{X}^a$ satisfies:

$$Tr(A) = \sigma_a^2 = \left(\mathbf{X}^t - \mathbf{X}^a\right)^2 < Tr(B) = \sigma_b^2 = \left(\mathbf{X}^t - \mathbf{X}^b\right)^2$$

This diagnostic can be formulated easily:

$$\left|\mathbf{X}^t - \mathbf{X}^a\right| \leq \left|\mathbf{X}^b - \mathbf{X}^a\right| \tag{61}$$

Of course this diagnostic could not be performed in the case of real observations, because the true value $\mathbf{X}^t$ would be unknown.

In the observation space

Another common diagnostic in data assimilation is to verify that the analysis error variance is also reduced in the observation space. This implies that the variance of the difference between the analysis projection $H(\mathbf{X}^a)$ and the observations $\mathbf{Y}^o$ is smaller than the variance of the difference between the background projection $H(\mathbf{X}^b)$ and the observations [Ric10]:

$$\text{RMS(OMA)=RMS}\left(\mathbf{Y}^o - H(\mathbf{X}^a)\right) \leq \text{RMS(OMB)} = \text{RMS}\left(\mathbf{Y}^o - H(\mathbf{X}^b)\right) \tag{62}$$

7.2 Data assimilation formalism with field observations

7.2.1 Definition of field observations

Observations are spread over the whole domain with a prescribed space frequency f_x and f_y. The measurements are taken at each observational time with a time frequency f_t, so that there are multiple observations at a same grid position over an assimilation window.

This type of observation can be assimilated to *in situ* measurements of the fire such as sensors used by firefighters.

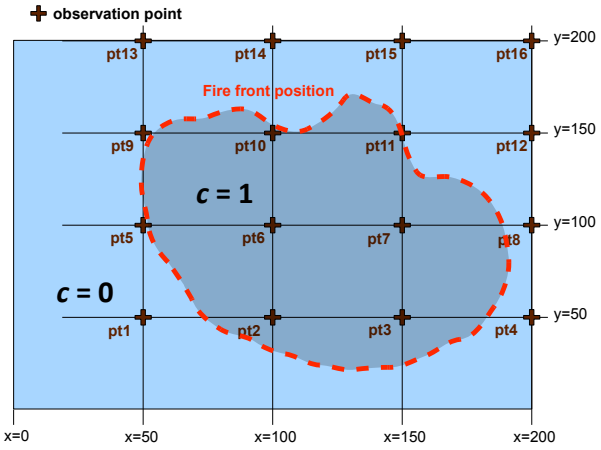

Figure 25: Field observations at a given observation time for a frequency $f_x = f_y = \dfrac{1}{50}$.

7.2.2 How to describe the observation operator H ?

Formalism

In the case of field observations the observation operator H can be written as a composition of the model M, given that we calibrate model parameters, and a selection operator S, which extracts the modeled field $c(x, y, t)$ at observation points for each observation time t_{obs}:

$$\begin{aligned} c(x, y, t) &= M(\mathbf{X}) \\ H(\mathbf{X}) &= S\left(M(\mathbf{X})\right) \end{aligned} \tag{63}$$

Structure of the observation operator $H(\mathbf{X})$

$H(\mathbf{X})$ is a vector of length p with

$$p = p_x \times p_y \times p_t$$

where,

- $p_x = N_x \times f_x$ is the number of observation points along x-axis;
- $p_y = N_y \times f_y$ is the number of observation points along y-axis;
- $p_t = N_t \times f_t$ is the number of observation times.

The structure of $H(\mathbf{X})$ reads:

$$H(\mathbf{X}) = \begin{bmatrix} \left.\begin{matrix} c(x_1, y_1, t_1) \\ \vdots \\ c(x_{p_x}, y_1, t_1) \\ c(x_1, y_2, t_1) \\ \vdots \\ c(x_{p_x}, y_2, t_1) \\ \vdots \\ c(x_{p_x}, y_{p_y}, t_1) \end{matrix}\right\} p_x \times p_y \\ \vdots \\ \vdots \\ \left.\begin{matrix} c(x_1, y_1, t_{p_t}) \\ \vdots \\ c(x_{p_x}, y_{p_y}, t_{p_t}) \end{matrix}\right\} p_x \times p_y \end{bmatrix} \tag{64}$$

where,

- $x_i = i \times \dfrac{dx}{f_x}$, $i = 1, .., p_x$: are the abscissa of the observation grid;
- $y_j = j \times \dfrac{dy}{f_y}$, $j = 1, .., p_y$: are the ordinates of the observation grid;
- $t_k = k \times \dfrac{dt}{f_{ty}}$, $k = 1, .., p_k$: are the observation times of the observation grid.

7.2.3 Observations generation for OSSE

Given that the observation space and the model space are representing the same quantity c, the noise addition is performed by adding a gaussian noise to $H(\mathbf{X}^t)$:

$$\mathbf{Y}^o = H(\mathbf{X}^t) + \epsilon^o \tag{65}$$

7.3 Data assimilation formalism with front-tracking observations

7.3.1 Definition of front-tracking observations

Observations are set along the front independently of the mesh, and follow its propagation with a fixed time frequency f_t. In this feasibility study, the number of observations N_p along the front is supposed constant in time.

This type of observation can be assimilated to airborne-like observations, visible or thermal-infrared data taken from planes [Mer09].

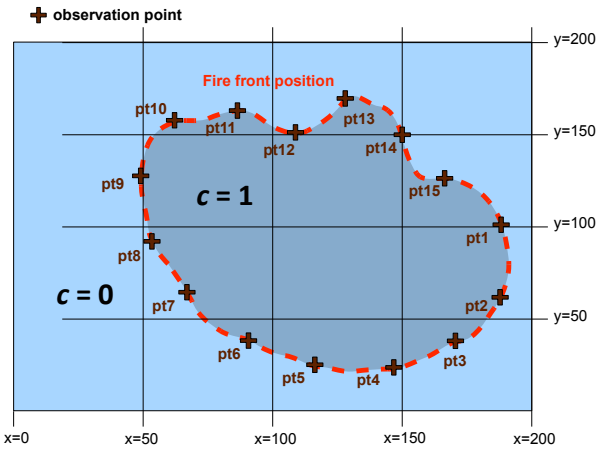

Figure 26: Front observations at a given observation time for $N_p = 15$.

7.3.2 How to describe the observation operator H ?

Formalism

To simplify the assimilation process, the observed fire front Γ^{obs} is supposed to be continuous (or as fine as needed). Under this assumption the observation operator H can be written as the composition of the model M, given that we calibrate model parameters, a selection operator S and a discretization operator D:

$$\begin{aligned} c(x,y,t) &= M(\mathbf{X}) \\ \Gamma(x,y,t) &= S\left(M(\mathbf{X})\right) \\ H(\mathbf{X}) &= D\left(S\left(M(\mathbf{X})\right)\right) \end{aligned} \tag{66}$$

Structure of the observation operator $H(\mathbf{X})$

$H(\mathbf{X})$ is a vector of length p with

$$p = 2 \times N_p \times p_t$$

where,

- N_p is the number of observation points along the front;
  - $2 \times N_p$ is the number of coordinates: one observation point = two coordinates (x_i, y_i);
  - $p_t = N_t \times f_t$ is the number of observation times ;

The structure of $H(\mathbf{X})$ reads:

$$H(\mathbf{X}) = \begin{bmatrix} \left.\begin{matrix} x_1^1 \\ y_1^1 \\ \vdots \\ x_{N_p}^1 \\ y_{N_p}^1 \end{matrix}\right\} 2 \times N_p \\ \vdots \\ \vdots \\ \left.\begin{matrix} x_1^{p_t} \\ y_1^{p_t} \\ \vdots \\ x_{N_p}^{p_t} \\ y_{N_p}^{p_t} \end{matrix}\right\} 2 \times N_p \end{bmatrix} \tag{67}$$

where,

- $x_i^k = x(\text{pt}_i,\, t = k \times \dfrac{dt}{f_{ty}})$, $i = 1..N_p$, $k = 1..p_t$: is the abscissa of the i^{th} observation point pt_i placed along the front at the k^{th} observation time;
- $y_i^k = y(\text{pt}_i,\, t = k \times \dfrac{dt}{f_{ty}})$, $i = 1..N_p$, $k = 1..p_t$: is the ordinate of the i^{th} observation point pt_i placed along the front at the k^{th} observation time;

Notation:
In the following (x_i, y_i) represents the coordinates of the i^{th} observation point pt_i placed along the front, independently from the mesh, for a fixed observation time:

$$(x_i, y_i) = (x(\text{pt}_i), y(\text{pt}_i))$$

Construction steps

The construction of the observation operator follows three steps (Figure 27):

1. Computation of the field $c(x, y)$ with the model:

$$c(x, y, t) = M(\mathbf{X})$$

2. Extraction of the continuous fire front $\Gamma(x, y)$ (i.e the isocontour $c = 0.5$) for each observation time t_{obs}:

$$\Gamma(x, y, t_{obs}) = S\left(M(\mathbf{X})\right)$$

3. Discretization of $\Gamma(x, y, t_{obs})$, defining the number of observation points $(x_i, y_i)_{i=1..N_p}$ per observation time t_{obs}, :

$$H(\mathbf{X}) \quad = \quad D\left(S\left(M(\mathbf{X})\right)\right)$$

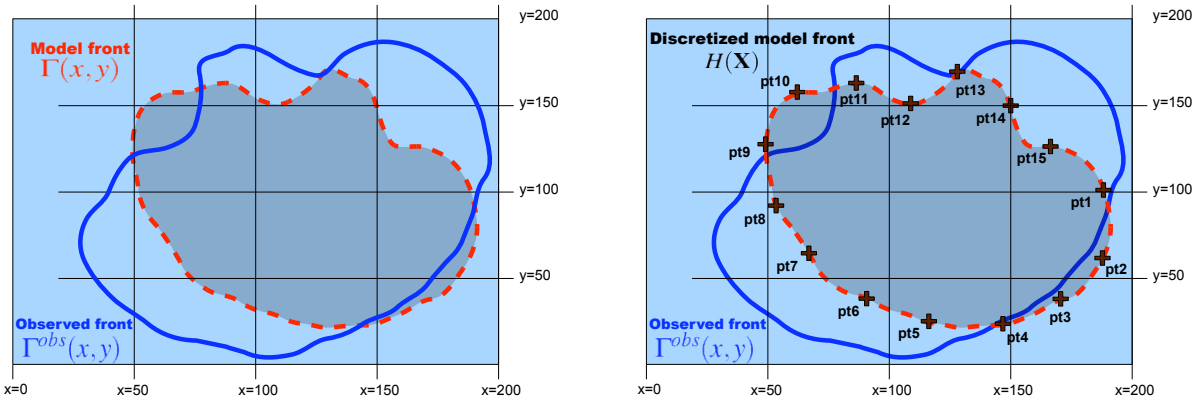

(a) Isocontour extraction S: $\Gamma(x,y) = S\left(M(\mathbf{X})\right)$

(b) Discretization D: $H(\mathbf{X}) = D\left(S\left(M(\mathbf{X})\right)\right)$

Figure 27: $H(\mathbf{X})$ with $N_p = 15$ at a given observation time t_{obs}.

The discretization step D

The discretization operation consists in defining N_p points along the model front $\Gamma(x,y)$ independently of the comutational mesh. The set of N_p points can be defined using many different techniques (equidistant, depending on the curvature of $\Gamma(x,y), ...$). In this study the points are placed equidistant along the isocontour. The distance between two consecutive points d is defined thanks to the perimeter of the front

$$d = \frac{\text{perimeter}}{N_p} \tag{68}$$

This method presents two main advantages:

1. the discretization is denser where the curvature of Γ is higher. The variations of the front contour are therefore well described.

2. Because the points are equidistant, the calculation of the normal to the isocontour can be directly computed by using the nearby observation points with a centered difference (Figure 28):

$$\vec{n}(x_i,y_i) = \begin{pmatrix} n_x(x_i,y_i) \\ n_y(x_i,y_i) \end{pmatrix} = \begin{pmatrix} \dfrac{y_{i+1}-y_{i-1}}{\sqrt{(x_{i+1}-x_{i-1})^2+(y_{i+1}-y_{i-1})^2}} \\ -\dfrac{x_{i+1}-x_{i-1}}{\sqrt{(x_{i+1}-x_{i-1})^2+(y_{i+1}-y_{i-1})^2}} \end{pmatrix} \tag{69}$$

Even if this method is less precise than if using a strictly isoceles triangle, it is still accurate when the observation discretization is dense enough.

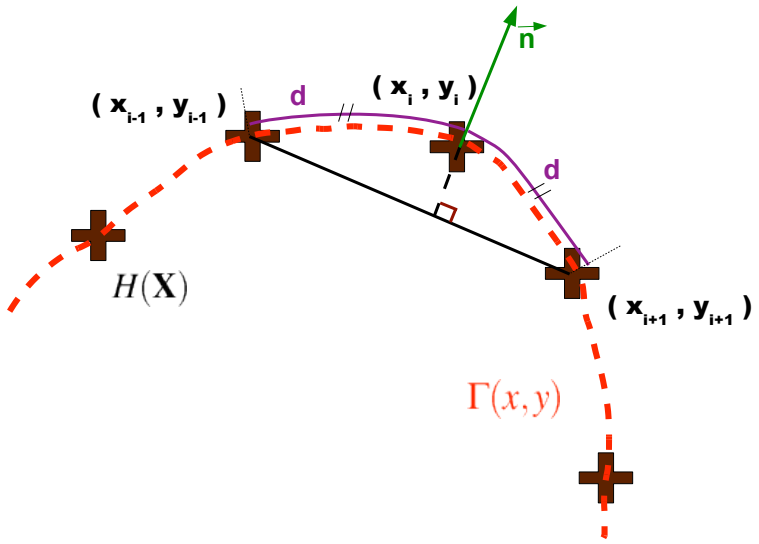

Figure 28: Normal calculation of $\Gamma(x, y)$ using the discretization $H(\mathbf{X})$ at a given observation time t_{obs}.

This discretization is an important step for the comparison of two isocontours, $\Gamma(x, y)$ and $\Gamma^{obs}(x, y)$, whose resolution or fineness can be different.

7.3.3 Innovation vector computation $\mathbf{d} = \mathbf{Y}^o - H(\mathbf{X})$: how to compare two isocontours ?

How to define $\mathbf{Y}^o$ ***from the continuous contour*** $\Gamma^{obs}(x, y)$ ***?***

The number of observation points N_p for a given observation time t_{obs} is given by the discretization step on the modeled fire front. Therefore, N_p equivalent points $(x_i^{obs}, y_i^{obs})_{i=1..N_p}$ must be defined on the observed continuous front, denoted by $\Gamma^{obs}(x, y)$, to evaluate the distance between $\Gamma(x, y)$ and $\Gamma^{obs}(x, y)$ in the observation space, which in this context represents the innovation vector:

$$\mathbf{d} = \mathbf{Y}^o - H(\mathbf{X})$$

Consequently, the distribution of N_p point along $\Gamma^{obs}(x, y)$ depends on the shape of $\Gamma(x, y)$ and on its discretization. It implies that, for a given value of the control parameter $\mathbf{X}_1$, $H(\mathbf{X}_1)$ is unique and its equivalent on the observed front $\mathbf{Y}_1^o$ is unique:

$$\begin{aligned} & \mathbf{X}_1 \neq \mathbf{X}_2 \\ \Rightarrow \quad & H(\mathbf{X}_1) \neq H(\mathbf{X}_2) \\ \Rightarrow \quad & \mathbf{Y}_1^o \neq \mathbf{Y}_2^o \end{aligned}$$

The equivalent of the modeled front discretization $(x_i, y_i)_{i=1..N_p}$ on $\Gamma^{obs}(x, y)$ is computed thanks to a projection P.

The projection operator P

For a given observation time t_{obs}, the projection operator projects the modeled discretized front $(x_i, y_i)_{i=1..N_p}$ on $\Gamma^{obs}(x, y)$ to obtain the observed discretized front $(x_i^{obs}, y_i^{obs})_{i=1..N_p}$:

$$P : (x_i, y_i)_{i=1..N_p} \rightarrow (x_i^{obs}, y_i^{obs})_{i=1..N_p} \tag{70}$$

The projection can be performed either, progressively, in agreement with the modeled physics of the fire, called progressive projection; or directly, in the normal direction to the modeled fire front, called direct projection.

Whichever the projection method is, the normal vectors are calculated using the technique previously mentionned (Figure 28).

Nota Bene:
For practical purposes, both projections do not require the explicit calculation of the isocontour Γ^{obs}, they just use the changes in the observed field $c^{obs}(x,y)$ around the value $c = 0.5$. More details are provided in Appendix B.

Progressive projection

The points of the discretized model front $(x_i, y_i)_{i=1..N_p}$ progressively follow the normal direction $\vec{n}(x,y)$ to the successive isocontours of the field $c(x,y)$ with a given step dr, until they reach the isocontour $\Gamma^{obs}(x,y)$ (Figure 29a), i.e. when the observed field $c^{obs}(x,y)$ changes from $c = 0.5^-$ to $c = 0.5^+$ or vice versa (cf. Appendix B).
This type of projection guarantees the equivalence between (x_i, y_i) and its image (x_i^{obs}, y_i^{obs}) because it follows the trajectory that would have followed the particle driven by the model M with a further time integration. However, some weaknesses have to be highlighted:

1. the model trajectory followed by (x_i, y_i) to reach $\Gamma^{obs}(x,y)$ might not be physically correct because the model is not necessarily representative of the real fire physics;

2. this type of projection is not well suited for a "binarized" field such as in the Level-Set method where the numerical thickness is $\mathcal{O}(\min(dx, dy))$. Indeed the successive isocontour Γ' cannot be extracted when $c = 0$ or $c = 1$.

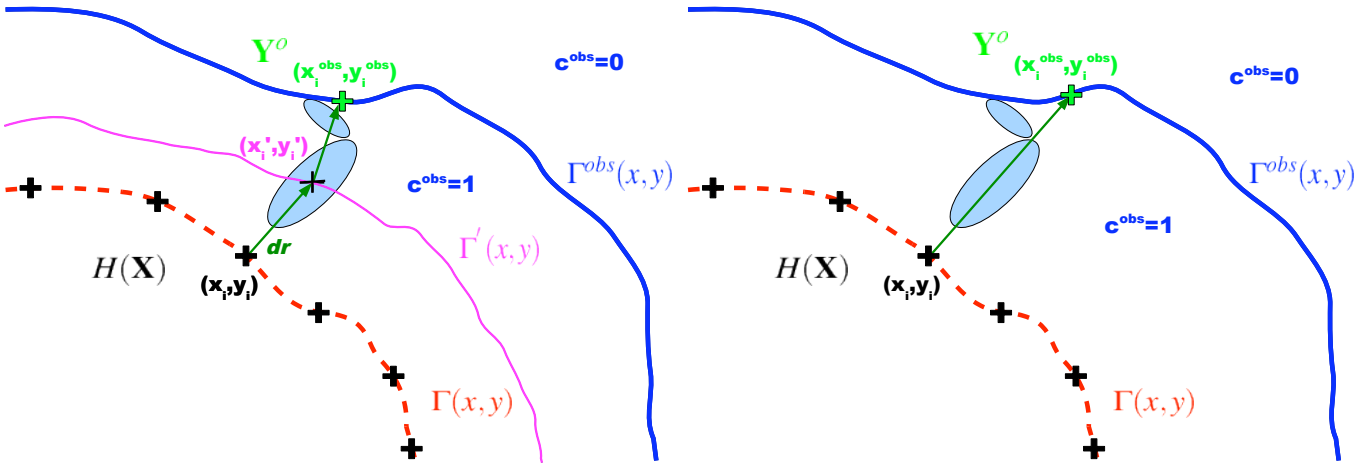

(a) Progressive projection.

(b) Direct projection.

Figure 29: Projection methods.

Direct projection

The points of the discretized model front $(x_i, y_i)_{i=1..N_p}$ are directly projected on $\Gamma^{obs}(x,y)$ following the normal direction to $\Gamma(x,y)$ (Figure 29b).
This type of projection does not depend on the physics of the fire (trajectory, fuel fluctuation,...) but it is less costly than the previous method and can be applied to a binarized field $c(x,y)$.

Discussion

The weaknesses of the progressive projection are too important to be neglected. Even if the direct projection is less in agreement with the fire physics, it can be applied for all type of field $c(x,y)$. Given that the modeled front is considered as an infinitely thin interface between $c = 0$ and $c = 1$, the progressive projection does not appear as a good technique for this feasibility study.

The lack of precision of the direct projection can lead to some errors in the evaluation of the distance when two fronts are far from each other. But as the modeled front gets closer to the observed front along the calibration process, these errors are progressively reduced.

Formulation of the observation vector $\mathbf{Y}^o$ in the context of OSSE

Considering the formulation of the observation operator $H(\mathbf{X})$ and the projection operator P, the observation vector reads:

$$\mathbf{Y}_1^o = P\left(H(\mathbf{X}_1)\right) \ , \forall \mathbf{X}_1 \tag{71}$$

7.3.4 Observations generation

Concerning front observations, the observation space and the model space are not representing the same quantity: the model provides a field $c(x, y, t)$ whereas the observation operator provides positions of the fire front:

$$H : \mathbf{X} \rightarrow \left((x_i, y_i)_{i=1..N_p}^j\right)_{j=1..p_t} \tag{72}$$

As explained in Appendix B, the projection algorithm only uses the changes of $c^{obs}(x, y, t)$ around the value $c = 0.5$ to place the observation points on $\Gamma^{obs}(x, y, t)$, but the isocontour $\Gamma^{obs}(x, y, t)$ itself is not calculated. As $\Gamma^{obs}(x, y, t)$ is not calculated, the projection algorithm does not allow the direct noise addition on the front positions $\Gamma^{obs}(x, y, t)$. Instead, a gaussian noise ϵ^o is added directly on the true trajectory $M(\mathbf{X}^t) = c^t(x, y, t)$ to obtain the synthesized observed field:

$$c^{obs}(x, y, t) = M(\mathbf{X}^t) + \epsilon^o$$

The noise addition on $c^t(x, y, t)$ implicitly changes the position of the observed front Γ^{obs} as:

$$\Gamma^{obs}(x, y, t) = S\left(M(\mathbf{X}^t) + \epsilon^o\right) \tag{73}$$

where S is the front extraction operator.

7.3.5 Linear tangent calculation

In the case of front assimilation, the difference $H(\mathbf{X}^g + \delta\mathbf{X}) - H(\mathbf{X}^g)$ is not straightforward, contrary to field assimilation. Again, it requires a distance evaluation between two fronts.
The technique is similar to the innovation vector calculation $\mathbf{d} = \mathbf{Y}^o - H(\mathbf{X})$. Let

- Γ^g the front obtained with the reference value:

  $$\Gamma^g(x, y, t) = S\left(M(\mathbf{X}^g)\right)$$

  and $H(\mathbf{X}^g)$ its discretization:

  $$H(\mathbf{X}^g) = D\left(\Gamma^g(x, y, t)\right);$$

- Γ^{pert} the front obtained with the perturbed value:

  $$\Gamma^{pert}(x, y, t) = S\left(M(\mathbf{X}^g + \delta\mathbf{X})\right).$$

The linear tangent calculation follows two steps:

1. Similarly to equation (71), $H(\mathbf{X}^g + \delta\mathbf{X})$ results from the projection P of $H(\mathbf{X}^g)$ on the isocontour Γ^{pert}:

   $$H(\mathbf{X}^g + \delta\mathbf{X}) = P\left(H(\mathbf{X}^g)\right)$$

2. The linear tangent is then computed with an upwind finite difference scheme:

   $$\mathbf{H} = \frac{H(\mathbf{X}^g + \delta\mathbf{X}) - H(\mathbf{X}^g)}{\delta\mathbf{X}} \tag{74}$$

7.3.6 Discussion on theoretical aspects of the observation operator in the context of front-tracking observations

A few questions can be raised concerning the observation operator formulation:

1. Firstly, as it is fromulated, is the observation operator differentiable with respect to the control parameter $\mathbf{X}$? ($\frac{\partial H}{\partial \mathbf{X}}$?)
2. Secondly, is it acceptable to define a different observation vector $\mathbf{Y}_k^o$ for each value $\mathbf{X}_k$ the control parameter takes ? Should $\mathbf{Y}^o$ be unique ?
3. Lastly, could a better method be applied to evaluate the distance between two fronts ?

To answer the first question, an extensive theoretical study needs to be conducted. Even if theoretical results prove somewhere that H is not differentiable with respect to $\mathbf{X}$, it does not intriscally mean that the numerical derivative, as it is computed in equation (74), would not exist...

The second point does not seem to be a real problem when using the BLUE algorithm. Indeed the analysis increment (or background correction) $\delta\mathbf{X}^a$ only depends on the innovation vector $\mathbf{d}^{ob}$, i.e. the distance between $\mathbf{X}^b$ and $\mathbf{Y}^o$, not $\mathbf{Y}^o$ itself:

$$\delta\mathbf{X}^a = \mathbf{K}(\mathbf{Y}^o - \mathbf{H}\mathbf{X}^b) = \mathbf{K}\mathbf{d}^{ob}.$$

Concerning the third question, the litterature abounds in different methods to calculate the distance between two fronts [BA05, CMD+10]. Obviously some of them are better than the one used in this study, but the latter is easy to implement and further results show that for current needs, it fulfills its duty.

All these points require further investigation to be fully understand and/or solved...

Part III

Parameter Calibration

In this study the calibration algorithm described in Section 6, is applied to the Rothermel's fire spread model introduced in Section 3.2 with the type of observations presented in Section 7.

8 One parameter calibration

This section aims at showing that the quality of the calibration algorithm is highly dependent on the observation set and on the model non-linearities[4].

8.1 Principle

8.1.1 Data assimilation formalism for the calibration of τ

The parameter to calibrate is the constant of proportionality initially given by Rothermel's model: $\tau[s^{-1}]$. The rate of spread of the fire front reads:

$$R(x,y) = \tau\bar{\delta}(x,y)$$

where $\bar{\delta}(x,y)$ is the normalized fuel bed thickness in the domain $\Omega = [0, L_1] \times [0, L_2]$.

***Control vector* X**

Using the data assimilation formalism, the control parameter $\mathbf{X}$ is a scalar ($n = 1$) and

$$\mathbf{X} = \tau$$

is the quantity to calibrate.

Background value $\mathbf{X}^b = \tau^b$

The background value is given by Rothermel's model depending on local conditions:

$$\mathbf{X}^b = \tau^b = f\left(\beta, \sigma, M_f, U, \tan(\varphi)\right)$$

with,

- The packing ratio:β [1], quantifies the compactness of the fuel bed;
- The surface-area-to-volume ratio: σ $[m^{-1}]$, quantifies the fuel partice size;
- The moisture content of the fuel bed: M_f [1];
- The wind amplitude in the normal direction to the fire front: U $[m.s^{-1}]$;
- The slope: $\tan\varphi$.

True value $\mathbf{X}^t = \tau^t$

The true parameter is precribed as a value $\mathbf{X}^t = \tau^t = 0.1$ which correponds the order of magnitude of τ given by Rothermel's model under no-wind, no-slope conditions.

Error modeling

Background error covariance matrix **B**

Given that $\mathbf{X}^b = \tau^b$ is a scalar, the background error standard deviation σ_b is also a scalar. In the context of OSSE σ_b reads

$$\sigma_b = \tau^b - \tau^t.$$

Therefore $\mathbf{B}$ is a scalar. It is the square of the background error standard deviation

$$\mathbf{B} = \sigma_b^2.$$

[4]A didactic example of non-linearity impact on the BLUE algorithm is also available in Appendix A.

Observation error covariance matrix $\mathbf{R}$

For both types of observations, the observation error covariance matrix is assumed to be diagonal (observation errors are not correlated) and every observation is given the same uncertainty σ_o. Therefore $\mathbf{R}$ reads

$$\mathbf{R} = \begin{bmatrix} \sigma_o^2 & & \\ & \ddots & \\ & & \sigma_o^2 \end{bmatrix} = \sigma_o^2 \mathbf{I}_p$$

where,

- $\mathbf{I}_p$ is the $p \times p$ identity matrix;
- p : is the number of observations.

Linear tangent calculation **H**

As explained in Section 5.1.4, the tangent linear $\mathbf{H}$ of the osbervation operator $H(\tau)$ is calculated using an upwind finite difference:

$$\mathbf{H} = \frac{H(\tau^g + \delta\tau) - H(\tau^g)}{\delta\tau}$$

where $\delta\tau$ is the linearization step.
$\delta\tau$ is arbitrarily prescribed a value by default :

$$\delta\tau = 0.05\tau^g.$$

Further results (cf. Section 8.3.2) show that this value should be changed depending on the non-linearity impact in the vicinity of the reference point τ^g.

8.1.2 Standard configuration

For the sake of simplicity and to focus only on assimilation matters, some values are set constant.

Numerical configuration

This first study is performed in a no-wind no-slope configuration. Table 2 depicts the numerical configuration.

Domain Ω	Simulation time	Discretization step	Time step
$\Omega = L_1 \times L_2 = 200 \times 200$	$[0; t_f],\ t_f = 800$	$dx = dy = 1$	$dt = 0.5$

Table 2: Numerical configuration.

The domain size $\Omega = L_1 \times L_2 = 200 \times 200$, corresponds to the macroscopic scale of a wildland fire.
Also the time step dt is chosen in order to satisfy the stability for both reaction-diffusion and Level-Set numerical schemes. With $dt = 0.5$ the acceptable range for the rate of spread R differs depending on the numerical scheme:

- considering the mesh ($dx = dy = 1$), the stability condition of the reaction diffusion numerical scheme reads

$$\max_{x,y \in \Omega} R(x, y) \leq \frac{0.725}{0.5\beta dt}$$

for $\beta = 1.2$ the condition on the rate of spread R becomes

$$\max_{x,y \in \Omega} R(x, y) < 12$$

- the stability condition of the Level Set numerical scheme reads

$$\max_{x,y\in\Omega}\left(R_x(x,y),R_y(x,y)\right)\leq\frac{0.3}{2dt}$$

for $dt=0.5$ the condition on the rate of spread R becomes

$$\max_{x,y\in\Omega}\left(R_x(x,y),R_y(x,y)\right)\leq 0.3$$

The assimilation window runs through the whole simulation time from $t=0$ to $t=t_f=800$.

8.2 Former work

A previous feasibility study on the calibration of the constant of proportionnality τ has been performed in [Roc10]. This former study was conducted with field observations and no external loops.
This work led to three main conclusions:

1. the behavior of the data assimilation prototype is consistent in terms of diagnostics in the parameter and observation space. However, external loops must be implemented to allow a more extensive study on the calibration behavior for bigger background errors σ_b.
2. A large number of observations subject to a high uncertainty can, in some configurations, have a larger contribution to the analysis than a few observations with a lower uncertainty. The results show that there is, however, a threshold to this phenomenon.
3. A quantitative contribution of observations to the analysis is calculated using the Degree of Freedom for Signals (DFS). It shows that the information on the fire system is located in the surrounding of the front, which moves over time depending on the location of the fuel pockets.

8.2.1 Consistency of the assimilation prototype

The BLUE algorithm is used to calibrate τ. The propagation model is the reaction-diffusion model. The observation operator reads:

$$H(\tau)=S\left(M_{\text{R-D}}(\tau)\right)$$

with,

- $M_{\text{R-D}}$: the reaction diffusion model
- S: the selection operator, mapping model results on the observation grid defined in Table 3

Observations	x-frequency	y-frequency	Time-frequency	Total observations
Field	$f_x=\frac{1}{96}$	$f_y=\frac{1}{96}$	$f_t=\frac{1}{48}$	$4\times 16=64$

Table 3: Observation grid.

The behavior of the data assimilation prototype has been studied for an extensive set of configurations. For the sake of conciseness, only one case with random fuel depth distribution and $\tau^b=0.11$ is presented here in Table 4.

Observation variance σ_o	6×10^{-6}	6×10^{-4}	1×10^{-2}	6×10^{-2}	2×10^{-1}	1
Analysis τ^a	0.0995	0.0988	0.1054	0.1079	0.1090	0.1096
RMS$\big(H(\tau^t) - H(\tau^b)\big)$	1×10^{-1}	1×10^{-1}	1×10^{-1}	1×10^{-1}	1×10^{-1}	1×10^{-1}
RMS$(H(\tau^t) - H(\tau^a))$	7×10^{-3}	1×10^{-2}	6×10^{-2}	9×10^{-2}	1×10^{-4}	1×10^{-1}
DFS	0.99	0.85	0.188	0.05	0.01	0.002

Table 4: Results for a decreasing level of confidence in the observations.

When the level of confidence in the observations increases, the analysis varies from the background $\tau^b = 0.11$ towards the true control parameter $\tau^t = 0.10$ (Figure 30). Consistently, the DFS for the ensemble of the observations on the data assimilation window increases from 0 to 1, meaning that the contribution of the observations also increases.

However, the impact of non-linearities reduces the choice on the background error (here $\sigma_b = 0.1$). That is why external loops must be implemented to study assimilation results for a wider range of σ_b.

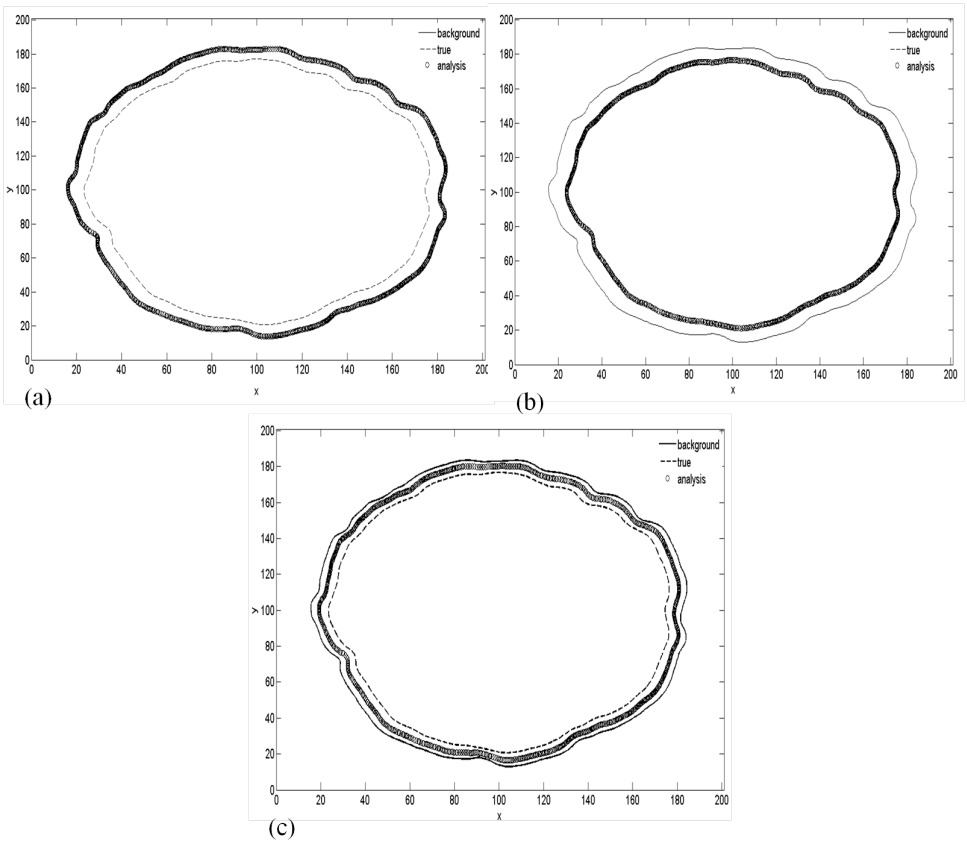

Figure 30: Position of the simulated front at $t = 800$ with the true parameter in dashed line, the background parameter in solid line and the analysed parameter in circle line (a) Scenario 1: when a high level of confidence is prescribed on the background (b) Scenario 2: when a high level of confidence is prescribed on the observations (c) Scenario 3: when an equivalent confidence is prescribed on the background and on the observations.

8.2.2 Analysis depending on observation frequency

One of the objective of this former study was to check how the analysis behaves if the observation frequency is changed: is there a threshold from which the analysis does not change if the number of the observations increases?

Two importants results are to be highlighted:

1. Table 5 shows that, for a fixed assimilation window $[0; 800\,s]$, the level of confidence in the analysis increases when the frequency decreases. The lower the frequency, the higher the number of observations is. When there are more assimilated observations, the algorithm is able to capture more information on the system and thus, to correct with a better accuracy the control parameter. Also, the non-linearities interfere more likely with the assimilation when the number of assimilated observations p decreases.

Obs. frequency	Number of obs. p	Analysis τ^a	Analysis uncertainty $\mathbf{A} = \sigma_a^2$
$\frac{1}{32}$	1800	0.10014	3.1×10^{-9}
$\frac{1}{64}$	225	0.09996	1.7×10^{-8}
$\frac{1}{96}$	64	0.0996	3.2×10^{-6}
$\frac{1}{101}$	15	0.1097	9.9×10^{-5}

Table 5: Analysis as a function of observation frequency for inhomogeneous vegetation and $\tau^b = 0.11$.

2. Figure 31 shows that a large number of observations subject to a high uncertainty can, in some configurations, have a larger contribution to the analysis than a few observations with a lower uncertainty. It also highlights the threshold to this phenomenon: for $f = 32$, the analysis does not change for $\sigma_o^2 \leq 2 \times 10^{-3}$. .

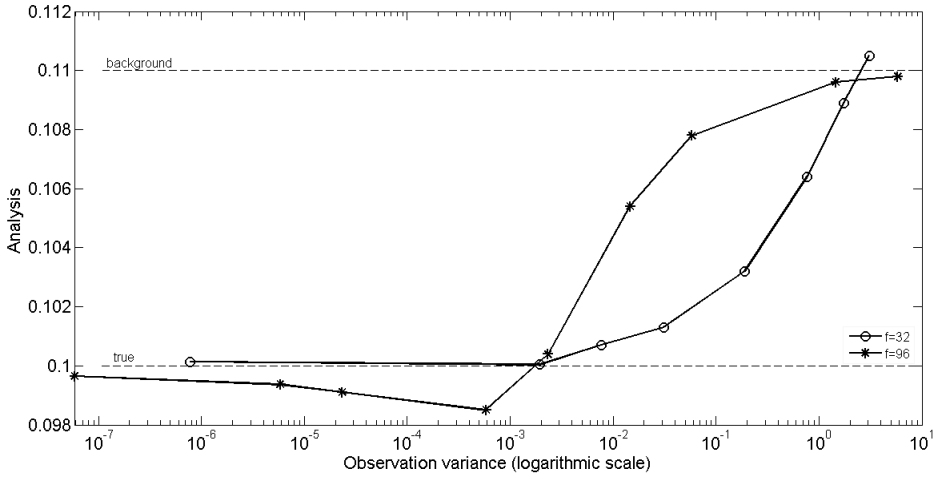

Figure 31: Analysis depending on σ_o^2 for two frequencies $f = \frac{1}{32}$ and $f = \frac{1}{96}$.

8.2.3 Importance of observation location using Degree of Freedom for Signals (DFS)

Figure 32 shows the progress variable $c(x, y)$ and the DFS of each observation point at a given time $t = 100$. It reveals that the information is mostly located on the front and more particularly where the propagation speed is higher.

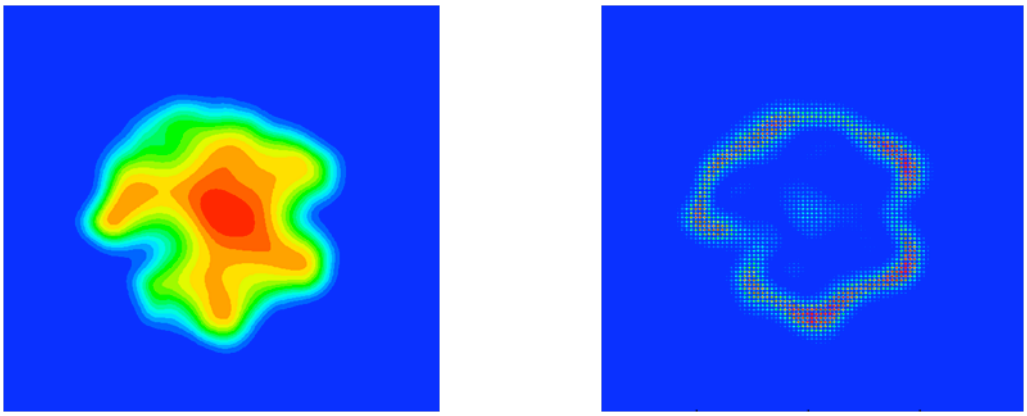

(a) Progress variable c at $t = 100$.

(b) DFS per observation at $t = 100$ for $f_x = f_y = \frac{1}{2}$.

Figure 32: Location of the information provided to the assimilation system with the reaction diffusion model.

8.3 Comparative tests between field observation and front observation performances

Based on the previous conclusions two main works have been achieved :

1. External loops implementation to overcome non-linearities and guarantee the convergence of the calibration algorithm whichever value the background takes;
2. The DFS results naturally led to a feasibilty study of the calibration with front observation. Indeed, front observations would make the calibration process more efficient given that they bring more information to the assimilation system than field observations.

8.3.1 Comparison of performances for a similar number of observation points along the front

In order to compare field and front assimilations, the number of observations in space and time must be the same for each set. To ensure this condition, the number of observation points along the front is taken equal to the average number of field observation points reached by the front in the assimilation window (cf. example in Figure (33)).

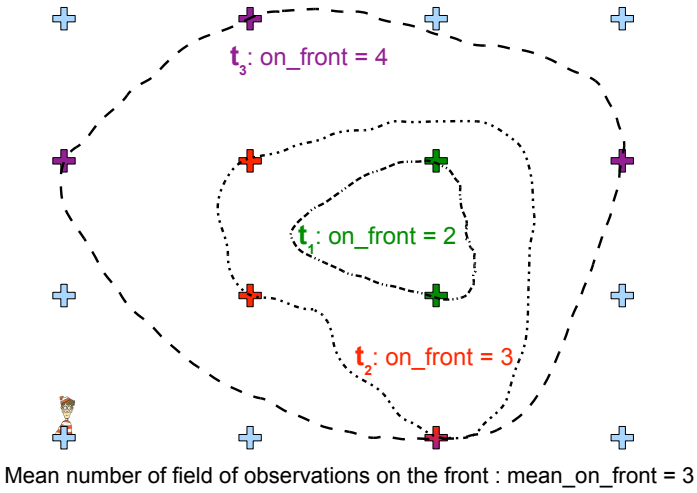

Figure 33: Mean number of field observation points on the front for three observation times.

Assimilation configuration

In the context of OSSE, the observations are granted a high confidence, so that $\tau^t = \arg\min J_{3DVAR}$. The true value and the assimilaton window are kept unchanged. The observation grid is defined in Table 6. External loops are implemented with a convergence criterion $\eta = 1\%$:

$$\text{if } \frac{\left\|\tau_i^a - \tau_{i-1}^a\right\|_2}{\left\|\tau_{i-1}^a\right\|_2} \leq 1\% \text{ then}$$

$$\text{STOP} \quad \text{CALIBRATION}$$

The normalized fuel depth is randomly distributed between $\min_{x,y\in\Omega} \bar{\delta}(x,y) = 0.1$ and $\max_{x,y\in\Omega} \bar{\delta}(x,y) = 0.8$.

Observations	x-frequency	y-frequency	time-frequency	Total observations
Field	$f_x = \frac{1}{50}$	$f_y = \frac{1}{50}$	$f_t = \frac{1}{25}$	$16 \times 32 = 512$
	Number of points along the front		time-frequency	Total observations
Front	$N_p = 3,\ 4 \text{ or } 5$		$f_t = \frac{1}{25}$	$2 \times N_p \times 32 = 64N_p$

Table 6: Observation grid.

For front observations the observation operator reads:

$$H(\tau) = D\left(S\left(M(\tau)\right)\right)$$

with,

- M: the propagation model, either reaction diffusion or Level Set formulation;
- S: the selection operator, extracting the front from the field $c(x,y,t)$ obtained with the model;
- D: the discretization operator, which for a given observation time, define a discretization of the modeled front as defined in Table 6.

Four scenarii using both types of propagation models with both types of observation sets are tested (cf. Table 7).

Scenario	Propagation model	Type of observations
$S1$	Reaction-diffusion	Field
$S2$	Reaction-diffusion	Front
$S3$	Level-Set	Field
$S4$	Level-Set	Front

Table 7: Four test scenarii.

***Comparison between** $S1$ **and** $S2$*

A series of tests is carried out with the previous conditions in the context of OSSE. The results of the BLUE analysis[5] are given in Table 8. The percentages in parentheses represent the relative distance to the true value τ^t.

Background τ^b	Type of obs.	Number of obs. p	External loops	Analysis τ^a	Analysis uncertainty $\mathbf{A} = \sigma_a^2$
0.02 (-80%)	Field	$16 \times 32 = 512$	4	0.4010	3.4×10^{-8}
	Front	$2 \times 3 \times 32 = 192$	3	0.1000	5.4×10^{-14}
0.07 (-30%)	Field	$16 \times 32 = 512$	1	0.4350	1.8×10^{-7}
	Front	$2 \times 3 \times 32 = 192$	3	0.1000	5.6×10^{-14}
0.13 (+30%)	Field	$16 \times 32 = 512$	3	0.0999	2.3×10^{-11}
	Front	$2 \times 4 \times 32 = 256$	3	0.1000	3.7×10^{-14}
0.18 (+80%)	Field	$16 \times 32 = 512$	6	0.0999	1.8×10^{-11}
	Front	$2 \times 5 \times 32 = 320$	3	0.1000	2.8×10^{-14}

Table 8: Comparison between front and field assimilation for the reaction diffusion model

$S1$: Field assimilation behavior

Figure 34 shows the relative error of the analysis on the true value depending on the background value for the three first BLUE iterations.

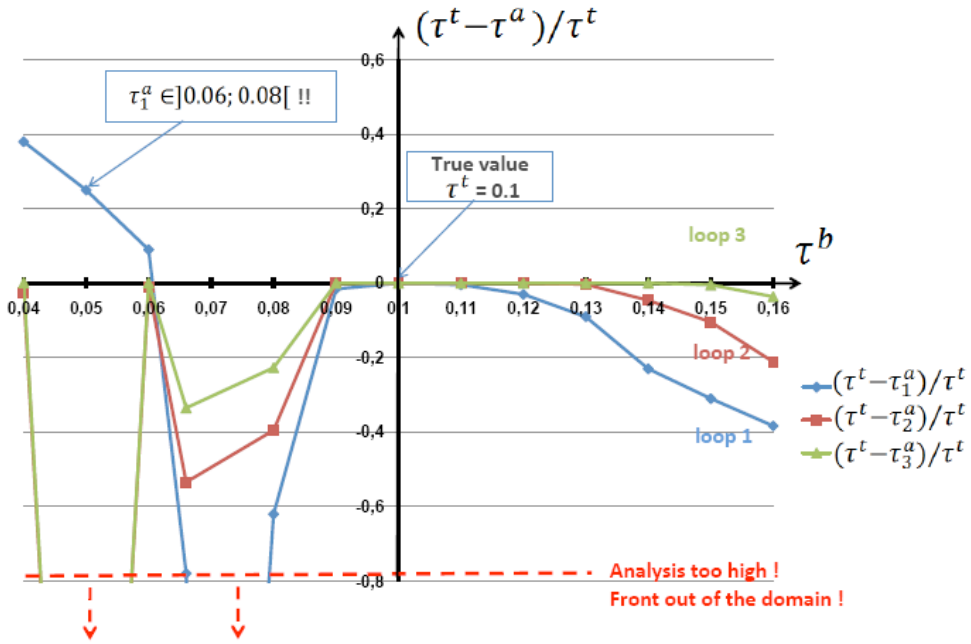

Figure 34: Relative distance between τ^t and $(\tau_i^a)_{i=1,..,3}$ on the ordinate according to $\tau^b = [0.04; 0.16]$ on the abscissa.

[5]Depending on the point of view this range of τ^b is not symetric with regard to the true value. On one side $\tau^b = 0.2\tau^t = \frac{\tau^t}{5}$ whereas on the other side $\tau^b = 1.8\tau^t$. If the mesh were symetric the right bound value for the background would be $\tau^b = 5\tau^t$. But here the background value is prescibed in terms of relative distance to the true value, as a percentage.

For $\tau^b \in]0.08; 0.16[$ all the common diagnostics are satisfied:

- In the control parameter space (Figure 34):
  - Each successive analysis τ_i^a is closer to $\tau^t = \arg\min J_{3DVAR}$ than the previous one τ_{i-1}^a:
$$\left\|\tau^t - \tau_i^a\right\|_2 < \left\|\tau^t - \tau_{i-1}^a\right\|$$
  - The final analysis τ^a is equal to $\tau^t = \arg\min J_{3DVAR}$: $\dfrac{\|\tau^t - \tau^a\|_2}{\|\tau^t\|_2} < 1\%$
  - The analysis uncertainty is smaller than the background uncertainty: $\sigma_a^2 < \sigma_b^2$.
- In the observation space (Figure 35):
  - The analysis projection in the observations space is closer to the observations than the projection of the background:
$$\text{RMS(OMA)=RMS}\left(\mathbf{Y}^o - H(\mathbf{X}^a)\right) \leq \text{RMS(OMB)} = \text{RMS}\left(\mathbf{Y}^o - H(\mathbf{X}^b)\right)$$

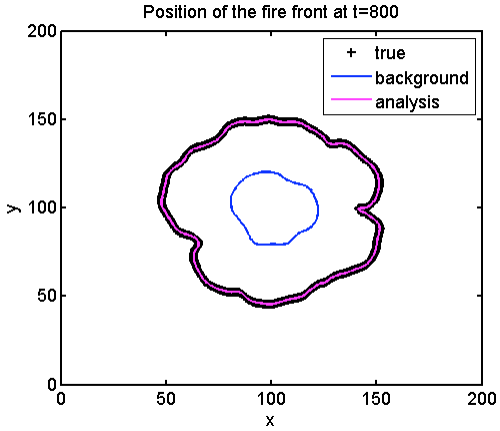

Figure 35: Example of good background correction for $\tau^b = 0.04$ (-60%).

However for a special region $\tau^b \in]0.06; 0.08[$ the impact of non-linearities is so strong that even external loops cannot compensate for the over-corrections of the background.

- In the control parameter space (cf. Figure 34):
  - The analysis is far from the true value.
  - When reaching the interval $]0.06; 0.08[$ the sucessive analysis go farther to the true value: $\left\|\tau^t - \tau_i^a\right\|_2 > \left\|\tau^t - \tau_{i-1}^a\right\|$.
- In the observation space (cf. Figure 36):
  - The analysis projection in the observations space is farther to the observations than the projection of the background:
$$\text{RMS(OMA)=RMS}\left(\mathbf{Y}^o - H(\mathbf{X}^a)\right) > \text{RMS(OMB)} = \text{RMS}\left(\mathbf{Y}^o - H(\mathbf{X}^b)\right)$$

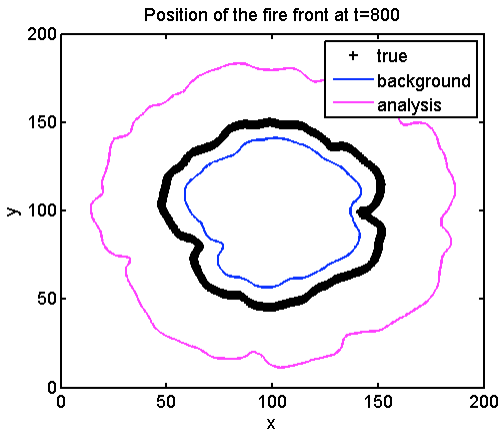

Figure 36: Example of over-correction due to the non-linearities, $\tau^b = 0.08$ (-20%) and $\tau^a = 0.16$ (+60%).

The presence of this "dangerous zone" is problematic because, whatever is the background value τ^b, as soon as the BLUE provides an analysis matching the interval $]0.06; 0.08[$, the next analysis will be out of range and make the analysed front go out of the domain Ω (Figure 34):

$$\text{if} \quad \tau_i^a \in]0.06; 0.08[\quad \text{then}$$

$$\tau_{i+1}^a < 0 \qquad \text{or} \qquad \tau_{i+1}^a \gg \tau^t$$

Depending on the observation position in space and time, the "dangerous zone" differs. Indeed, the importance of the non-linearities is highly correlated to the position of the assimilated observations over the computational domain. When the assimilated observations are sparse over the domain an important proportion of these observations can be upstream or downstream from the fire front, in the zone where the progress variable c is low, and therefore where the non-linearities are considerable. In the opposite, when the observation network is denser, there are more observations (in proportion) located inside the front, and so these observations can provide important information to the assimilation, avoiding the non-linearities as they have a higher contribution to the analysis. Also, when the observation operator H is highly non-linear in the vicinity of the reference point τ^g, the linearization step $\delta\tau^g$ plays an important role in the calibration process. It defines the slope $\mathbf{H}$ from which the BLUE cost function J_{BLUE} is computed and then minimized. More details are provided in 8.3.2

$S2$: Front assimilation behavior

The calibration using front observations provides consistent results (Table 8) concerning all the diagnostics presented previously.

In addition, it presents several advantages:

- the impact of non-linearities on the results is reduced:
  - the algorithm needs less iterations to converge than with field observations;
  - for the observation set considered, no "dangerous zone" appears;
- the results are good considering the low number of observations on the front;
- the analysis uncertainty $\mathbf{A} = \sigma_a^2$ is smaller than with field observations.

The fact that all observation points are located on the front and provide significant information to the assimilation system may diminish the impact of non-linearities (cf. Section 8.3.2). Also the change in the observed quantity, progress variable c for field observations and front positions (x_i, y_i) for front observations, may be a factor in this improvement...

***Comparison between** $S3$ **and** $S4$*

A series of tests is carried with the same conditions in the context of OSSE. The fire spread is solved with the Level-Set formulation. The results of the BLUE analysis are given in Table 9.

Background τ^b	Type of obs.	Number of obs. p	External loops	Analysis τ^a	Analysis uncertainty $\mathbf{A} = \sigma_a^2$
0.02 (-80%)	Field	$16 \times 32 = 512$	2	0.0203	6.4×10^{-3}
	Front	$3 \times 32 = 96$	3	0.1000	6.1×10^{-14}
0.07 (-30%)	Field	$16 \times 32 = 512$	1	7.613	8.6×10^{-4}
	Front	$3 \times 32 = 96$	2	0.1000	5.9×10^{-14}
0.13 (+30%)	Field	$16 \times 32 = 512$	5	0.0999	1.1×10^{-11}
	Front	$4 \times 32 = 128$	10	0.0999	3.1×10^{-14}
0.18 (+80%)	Field	$16 \times 32 = 512$	10	0.1000	8.6×10^{-12}
	Front	$5 \times 32 = 160$	3	0.1000	1.3×10^{-14}

Table 9: Comparison between front and field assimilation for the Level Set model

Either using field observations or front observations the behavior of the assimilation system is similar to the calibration using the reaction diffusion model.

However, concerning field observations the impact of non-linearities is even stronger. For $\tau^b = 0.07$ (-30%) the resulting analysis $\tau^a = 7.613$ is 20 times farther to the true value τ^t than the analysis $\tau^a = 0.435$ obtained using the reaction-diffusion model. The front thickness in the Level-Set solution is so small that the probability for an observation to be inside the front is lower than using the reaction-diffusion model where the front thickness is larger ($\approx 8\beta dx$ instead of $\approx 3dx$). Figure 37 shows that the information is contained in a thiner zone than for the reaction-diffusion equation. Given that the slope describing the front is sharper for the Level-Set solution, the transition between the unburnt area, $c = 0^+$, and the front zone $0^+ < c < 1^-$ is more abrupt and therefore more non-linear.

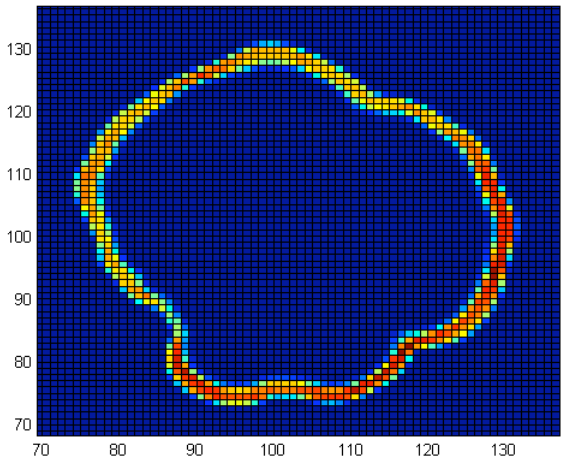

Figure 37: DFS per observation at $t = 200$ with the Level Set model.

Also, for $\tau^b = 0.02$ (-80%) the background correction is too small to significantly rectify τ^b. Indeed, when τ^b is

small, the rate of spread $R(x, y)$ is small. Then none of the observation points are close to the front. When all the observation points are far from the front, and in addition, the front is thin and sharp, the variations of $H(\tau)$ in the vicinity of τ^b are very small. Therefore (cf. Section 7.3.5)

$$\mathbf{H} = \frac{H(\tau^b + \delta\tau) - H(\tau^b)}{\delta\tau} \approx 0$$

and then the gain matrix of the BLUE algorithm is close to zero:

$$\mathbf{K} = \mathbf{B}\mathbf{H}^T \left(\mathbf{H}\mathbf{B}\mathbf{H}^T + \mathbf{R}\right)^{-1} \approx 0.$$

Therefore the background correction is insignificant

$$\delta\tau^a = \mathbf{K}(\mathbf{Y}^o - H(\tau^b) \approx 0.$$

Consequently,

$$\frac{\|\tau_2^a - \tau_1^a\|_2}{\|\tau_{i-1}^a\|_2} = \frac{\|\delta\tau^a\|_2}{\|\tau_{i-1}^a\|_2} < \eta = 1\%$$

and the calibration algorithm stops.

8.3.2 Cost function comparison for $S3$ and $S4$

Studying the shape of the cost functions J_{3DVAR} and J_{BLUE} provides a visual evaluation of the performances of the BLUE algorithm and the impact of non-linearities on the minimization process.

Figures 38 and 42 show the cost function J_{3DVAR} and the first quadratic cost function J^1_{BLUE} for $\tau^b = 0.07$ (-30%) using field and front assimilations with the Level-Set equation (scenarii $S3$ and $S4$).

S3:***Field observations***

The cost function J_{3DVAR} related to the field observation is clearly less quadratic than the cost function related to front observations.

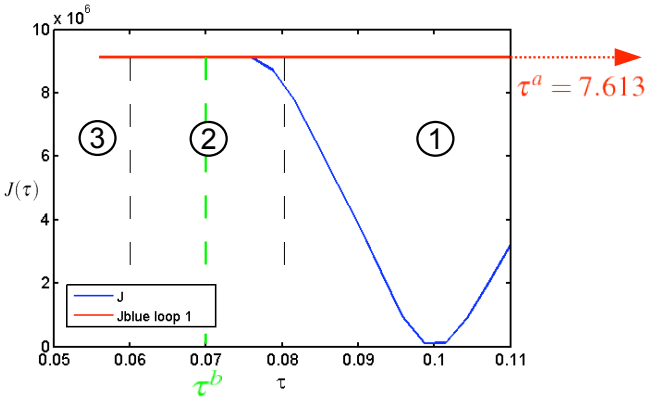

Figure 38: J_{3DVAR} and J^1_{BLUE} for $\tau^b = 0.07$ (-30%) using field observations with the Level-Set model.

Three zones can be distinguished:

1. The "quadratic" zone: $\tau > 0.08$

The cost function J_{3DVAR} has a quadratic shape. In this zone the calibration process quickly converges toward the true value τ^t.

2. The "transition" zone: $\tau \in]0.06; 0.08[$

The strong change in slope in Figure 39b corresponds to a "dangerous" zone. This behavior matches the interval in which a sufficient amount of observation points transits from fresh fuel to the front zone. The highly non-linear

aspect of this transition leads to a flawed linear approximation of the observation operator $H(\tau)$, $H_{Taylor}(\tau) = H(\tau^b) + \mathbf{H}(\tau - \tau^b)$ (cf. Section 6.3), in the interval $[\tau^b; \tau^b + \delta\tau]$ for the linearization step $\delta\tau = 0.05\tau^b$.

As shown on Figure 39a, H_{Taylor} is underestimating the growth of H :

$$H_{Taylor}(\tau) \ll H(\tau) \text{ when } \tau > \tau^b = 0.07.$$

Thus,

$$\arg\min \tfrac{1}{2} \left(\mathbf{Y}^o - H_{Taylor}(\mathbf{X})\right)^T \mathbf{R}^{-1} \left(\mathbf{Y}^o - H_{Taylor}(\mathbf{X})\right) \quad \gg \quad \arg\min \tfrac{1}{2} \left(\mathbf{Y}^o - H(\mathbf{X})\right)^T \mathbf{R}^{-1} \left(\mathbf{Y}^o - H(\mathbf{X})\right)$$

or equivalently

$$\arg\min J^o_{BLUE} \gg \arg\min J^o_{3DVAR} \tag{75}$$

Besides, in this assimilation configuration the observations are granted a high confidence. Therefore (cf. Section 6.7)

$$J^o_{BLUE} \gg J^b_{BLUE} \tag{76}$$

and, by definition

$$J^b_{BLUE} = J^b_{3DVAR} \tag{77}$$

So equations (75), (76) and (77) lead to

$$\begin{aligned} \arg\min J_{BLUE} \quad &\gg \quad \arg\min J_{3DVAR} \\ \Leftrightarrow \qquad \tau^a \quad &\gg \quad \arg\min J_{3DVAR} \end{aligned} \tag{78}$$

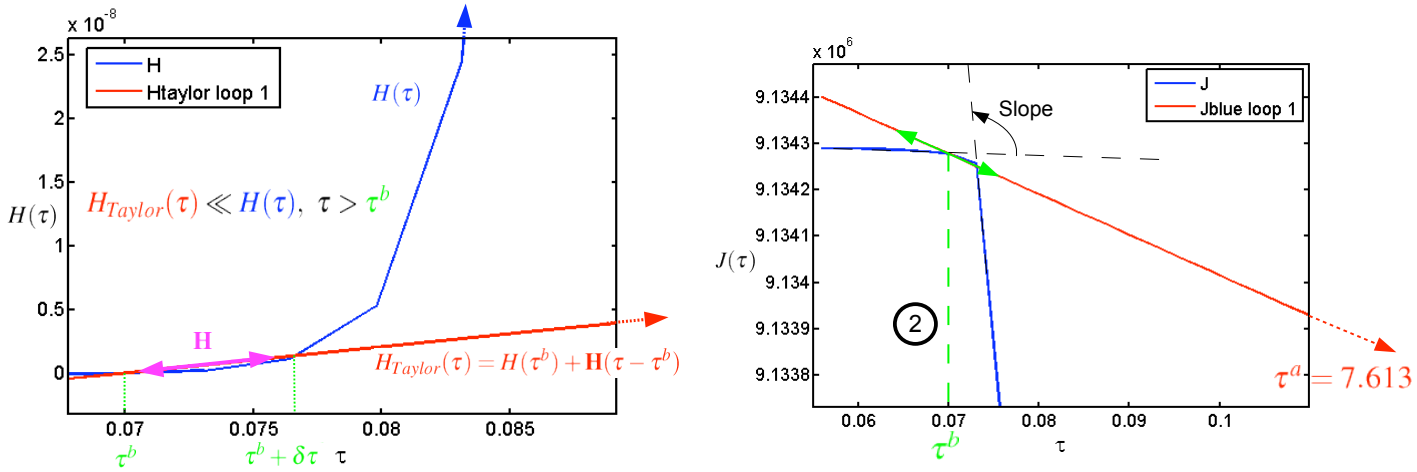

(a) Impact on the linear approximation H_{Taylor}.

(b) Impact on the shape of J_{BLUE}.

Figure 39: Example of the non-linearity impact in the transition zone for $\tau^b = 0.07$ (-30%).

That is why, in the transition zone the BLUE algorithm provides results far from the true value : $\tau^a = 7.613$ for $\tau^b = 0.07$.

This non-linearity problem could be overcome by densifying the observation network. Even for small values of τ^b some observation points would be located on the front. There would still be a flat zone but for smaller background values. Also, when J_{3DVAR} is non quadratic, the linearization step $\delta\tau$ plays an important role in the evaluation of the slope $\mathbf{H}$, and therefore in the shape of J_{BLUE}. By taking a longer step $\delta\tau > 0.05\tau^g$ the slope $\mathbf{H}$ would be closer to the slope in the quadratic zone. This way the shape of J_{BLUE} would be more convenient and provide an analysis that could be easier corrected iteratively. For instance, on Figure 40, $\delta\tau = 0.2\tau^b$ instead of $\delta\tau = 0.05\tau^b$, and the analysis is much closer to the true value: $\tau^a = 0.09$ instead of $\tau^a = 7.613$.

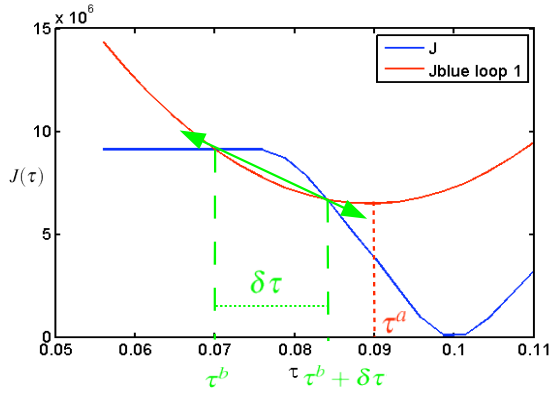

Figure 40: Analysis for a bigger linearization step $\delta\tau$.

3. The "flat" zone: $\tau < 0.06$

The cost function flattens for $\tau < 0.06$. As explained previously it is due to the fact that all observation points are far from the front. $H(\tau)$ becomes progressively constant as τ decreases. Thus J^o_{3DVAR} is constant in the vicinity of τ^b and the only variations of the cost function are due to the distance to the background value: $J^b_{3DVAR}(\tau)$. Thus, as shown on Figure 41

$$\arg\min J_{3DVAR} = \arg\min J^b_{3DVAR} = \tau^b$$

in the vicinity of τ^b

As for the BLUE cost function J_{BLUE}, the linearized observation operator H_{Taylor} is constant:

$$\mathbf{H} \approx 0 \Rightarrow H_{Taylor}(\tau) = H(\tau^b)$$

Consequently, J^o_{BLUE} is constant

$$J^o_{BLUE} = \frac{1}{2}\left(\mathbf{Y}^o - H(\tau^b)\right)^T \mathbf{R}^{-1}\left(\mathbf{Y}^o - H(\tau^b)\right)$$

and thus

$$\tau^a = \arg\min J_{BLUE} = \arg\min J^b_{BLUE} = \tau^b$$

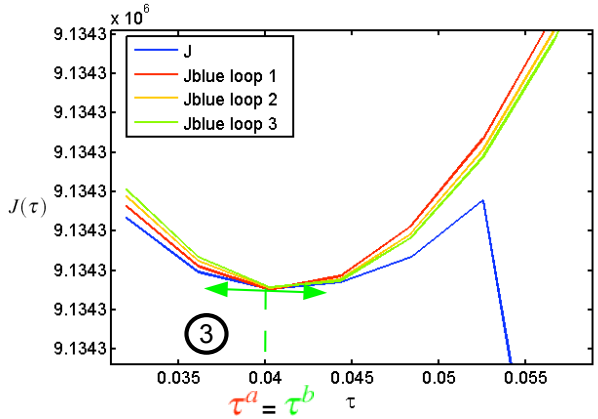

Figure 41: Detail of the flat zone for field observations in the vicinity of $\tau^b = 0.04 < 0.06$.

$S4$: ***Front observations***

Contrary to field observations, the cost function J_{3DVAR} has a quadratic shape in the vicinity of $\tau^b = 0.07$.

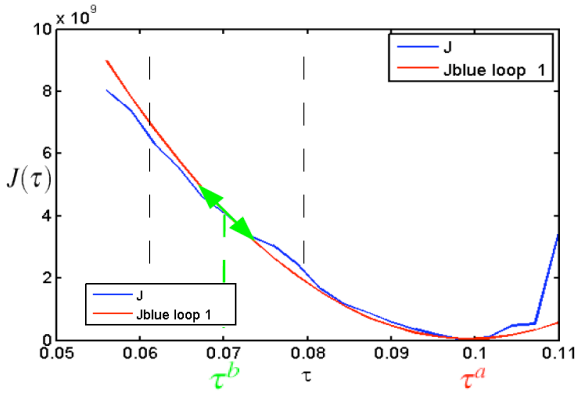

Figure 42: J_{3DVAR} and J^1_{BLUE} for $\tau^b = 0.07$ (-30%) using front observations with the Level-Set model.

There is no flat or transition zone. The non-linearities are not significant to disturb the assimilation process.

Discussion

This case study shows that the calibration process is less sensitive to non-linearities when using front observations than using field observations. Even though solutions have been presented to compensate for the non-linearities, front observations appear to provide better results whithout having to try different linearization steps or densifying the observation network.

Also, as shown in Section 4.3 the Level-Set method provides a more accurate solution than the reaction-diffusion model in term of front propagation speed.

So, Level Set method coupled with front observations ($S4$) turns out to be the best combination for parameter calibration.

A more complete study on performances, robustness and further results are presented in the following.

8.4 Further results for calibration using Level-Set model and front observations

So far, the Level-Set method coupled with front observations ($S4$) provide good results for a small number of observation points along the fire front. Thanks to the previous work, a more realistic situation can be studied.

8.4.1 Assimilation configuration

Usually, the resolution of the cameras used to take pictures of the forest fire from airplanes is such that more than 5 pixels actually describe the front.

Considering the scale of a wildfire, the number of observation points along the fire front is chosen to respect an average distance of $2m$ between two observation points. A picture of the front is assumed to be provided each $50s$. The characteristics of the observation set are given in Table 12.

Observations	Number of obs. points along the front	Time-frequency	Total observations
Front	$N_p = 200$	$f_t = \frac{1}{50}$	$2 \times 200 \times 16 = 6400$

Table 10: Observation set.

Again, the normalized fuel depth is randomly distributed between $\min_{x,y\in\Omega} \bar{\delta}(x,y) = 0.1$ and $\max_{x,y\in\Omega} \bar{\delta}(x,y) = 0.8$.

8.4.2 Performances

A series of tests is carried out with the previous conditions in the context of OSSE. The results of the BLUE analysis are displayed on Figure 43.

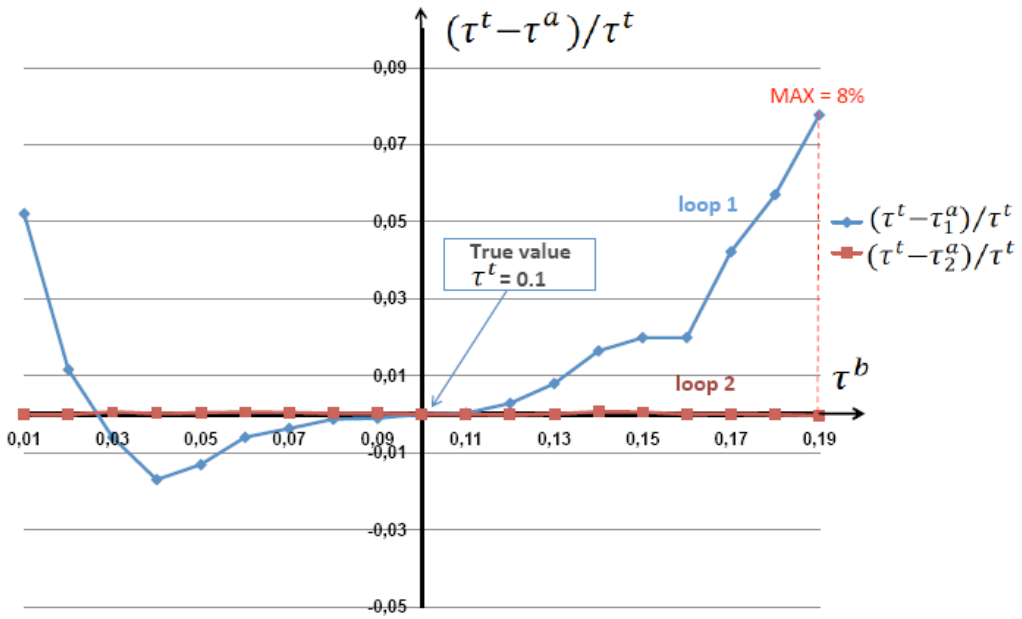

Figure 43: Relative distance between τ^t and $(\tau_i^a)_{i=1,2}$ according to $\tau^b = [0.01; 0.19]$ (-90%,...,+90%).

In the control parameter space

With a larger amount of observation points along the front, the calibration process is faster and more efficient. Even with only one loop, the largest distance to the true value τ^t is below 8% for $\tau^b = 0.19$ (+90%).

Whichever value the background τ^b takes, the distance between the analysis and the true value is less than 1% at the second BLUE iteration.

In the observations space

As τ^a always sticks to τ^t, the analysis projection is always closer to the observations than the background projection:

$$\text{RMS(OMA)}=\text{RMS}\left(\mathbf{Y}^o - H(\mathbf{X}^a)\right) < \text{RMS(OMB)} = \text{RMS}\left(\mathbf{Y}^o - H(\mathbf{X}^b)\right)$$

8.4.3 Analysis as a function of observation uncertainty

In this study, the level of confidence in the background is assumed to be constant, $\tau^b = 0.15$ is fixed and thus, $\mathbf{B} = 2.5 \times 10^{-3}$ is constant. Different assimilations are performed, each assimilation is associated to a different observation uncertainty σ_o even though the observation frequency is fixed to $N_p = 200$ points along the front in space and $f_t = \dfrac{1}{250}$ in time. Results are summarized in Table 11.

For front observation generation the gaussian noise ϵ^o is added on the true trajectory $M(\tau^t)$ (cf. Section 7.3.4). In this context, mean distance between the true projection and the observation vector, RMS(OMT), indicates the impact of the standard deviation σ_o on the observed front position $\mathbf{Y}^o$. As RMS(OMT) increases the analysis goes from the true state to the background state both in the control parameter space and observation space. Figure 44 shows the evolution of the analysis state depending on the noise added to observations.

Observation variance σ_o	6.5×10^{-3}	0.3	1
RMS(OMT) $=$ RMS$(\mathbf{Y}^o - H(\tau^t))$	1.3m	5.3m	10.1m
Analysis τ^a	0.0981	0.122	0.1509
RMS$\big(H(\tau^t) - H(\tau^b)\big)$	19.6	19.6	19.6
RMS(OMB) $=$ RMS$\big(\mathbf{Y}^o - H(\tau^b)\big)$	17.3	7.5	3.5
RMS$(H(\tau^t) - H(\tau^a))$	0.3	11	19.3
RMS(OMA) $=$ RMS$(\mathbf{Y}^o - H(\tau^a))$	1.6	4	3.5

Table 11: Results for a decreasing level of confidence in the observations.

These results also reveal that, for a given observation time frequency f_t, only a large incertainty on the observations can make the analysis diverge from the true value. As explained in Section 8.2.2 a large number of observations subject to a high uncertainty can, in some configurations, have a larger contribution to the analysis than a few observations with a lower uncertainty.

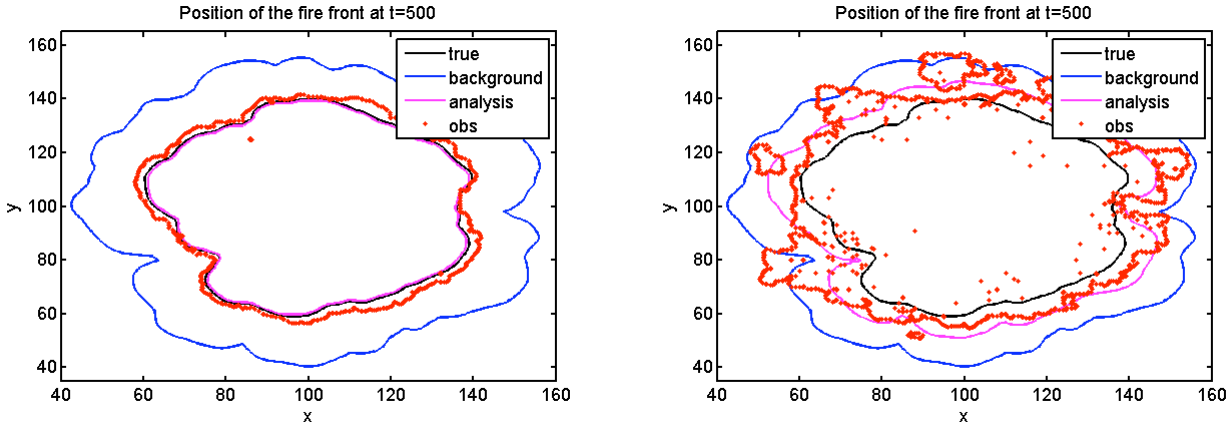

(a) The confidence of the observation is predominant: $\tau^a \approx \tau^t$. (b) Equal confidence between obs. and background: $\tau^t < \tau^a < \tau^b$

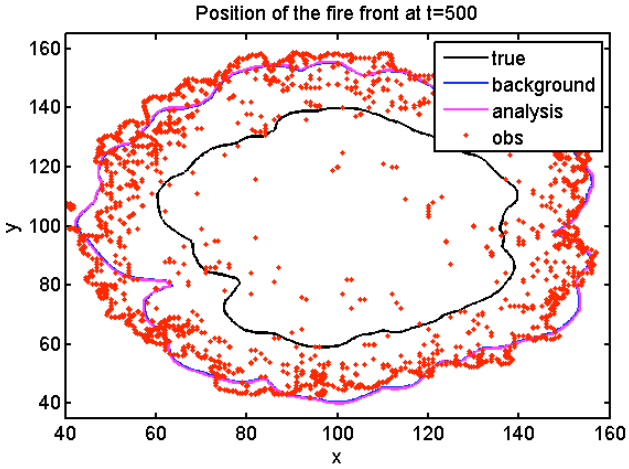

(c) The information on the background is predominant: $\tau^a \approx \tau^b$.

Figure 44: Analysed front depending on the observed front uncertainty.

8.4.4 Diagnostics and robustness of the method

DFS

A DFS diagnostic is applied to the front observation set. As each observation point (x_i, y_i) is bidimensionnal, a DFS per coordinate is computed :

$$\mathrm{DFS}_x = \mathrm{DFS}\left(\left((x_i)^j_{i=1..N_p}\right)_{j=1..p_t}\right)$$

and

$$\mathrm{DFS}_y = \mathrm{DFS}\left(\left((y_i)^j_{i=1..N_p}\right)_{j=1..p_t}\right)$$

As shown on Figure 45 the DFS is maximal in the privileged directions of propagation. DFS_x is maximal where $R_x = R(x,y)n_x$ is maximal and so for DFS_y. This behavior is consistent with the previous conclusion stating that the most important information on the fire dynamics is located where the speed is higher.

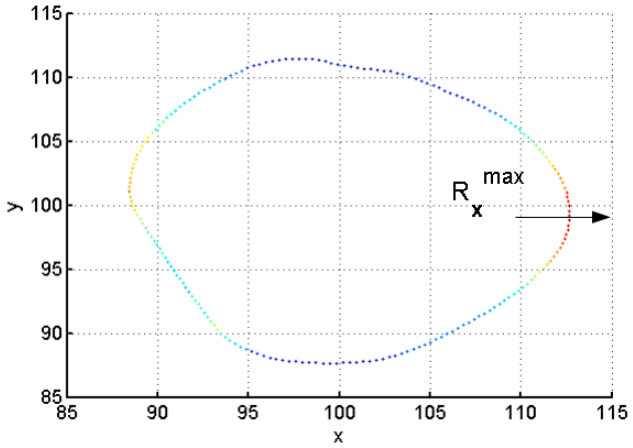

(a) DFS_x for $t = 100$.

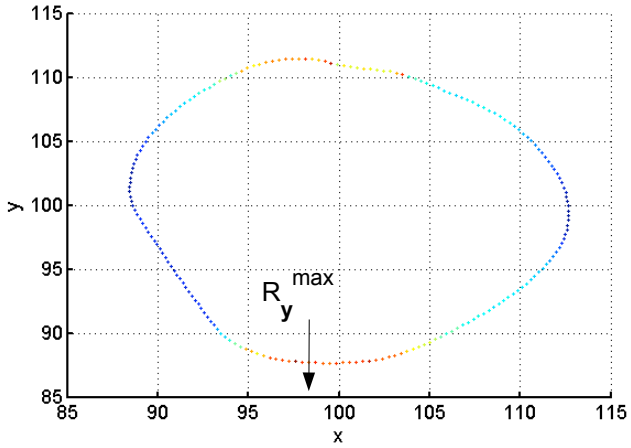

(b) DFS_y for $t = 100$

Figure 45: DFS per observation point $(\mathrm{DFS}_x, \mathrm{DFS}_y)$

Robustness

The calibration algorithm has been tested with different configurations to evaluate its robustness. The assimilation is performed in the context of OSSE: the observation are granted a high level of confidence, i.e. no noise addition on the true trajectory. The analysis should therefore convrege to the true value τ^t.

The clasp case (small lake)

This test case aims at studying the reaction of the calibration algorithm when the geometry of the front is such that it includes a clasp. Physically this clasp could be assimilated to a small lake or more generally to a zone without fuel (Figure 46).

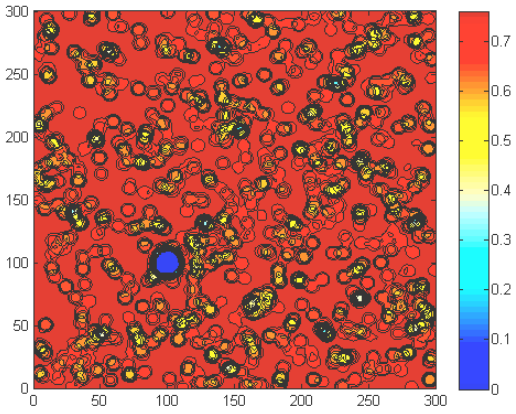

Figure 46: Random fuel distribution with small lake.

Two configurations are tested:

1. $\tau^b > \tau^t$: $\tau^t = 0.1$ and $\tau^b = 0.19$ (+90%). The background front is ahead of the observed front. In this test the observed front does not reach the "lake". Only the background front presents a clasp. Several steps in the assimilation process are affected (Figure 47):

   (a) The discretization D: because of the presence of the clasp, the total perimeter of the front is longer than the outside perimeter $P_{total} = P_{outside} + P_{clasp}$. Therefore the discretization step d is shorter than it should be: $d = \dfrac{P_{total}}{N_p}$ instead of $d = \dfrac{P_{outside}}{N_p}$. This leads to a lack of observation points in a portion of the isocontour $c = 0.5$.

   (b) The projection P: because of the vegetation heterogeneities, the shape of the fire front is sometimes such that the direction normal vector $\overrightarrow{n}$ does not coincide with the target observed front at some locations. By default, if a point cannot be projected on the target front, its projection is taken equal to the previous point projection.

   However the resulting analysis with only one BLUE iteration is still close to the true value: $\tau^a = 0.095$.

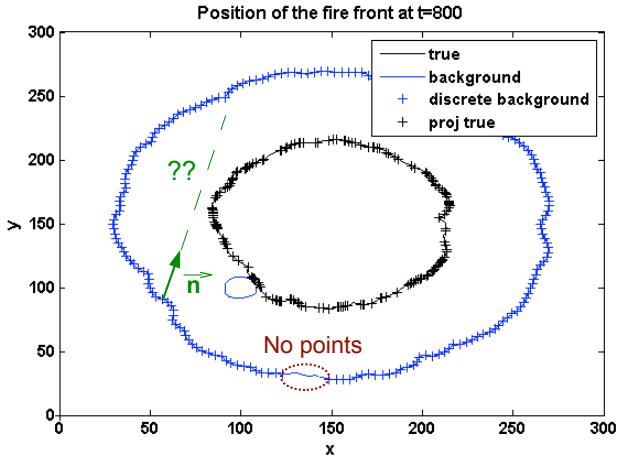

Figure 47: Background clasp for $t = 800$, $\tau^b = 0.19$

2. $\tau^b < \tau^t$: $\tau^t = 0.19$ and $\tau^b = 0.019$ (-90%). The observed front is ahead of the model front. Nor the discretization step nor the projection are affected but some projected points impact the clasp instead of

impacting the outside contour. But, as shown on Figure 48b, the resulting analysis after one BLUE iteration is still good : $\tau^a = 0.186$. Somehow, impacting the clasp provides a physical information to the calibration system that the lake slows propagation.

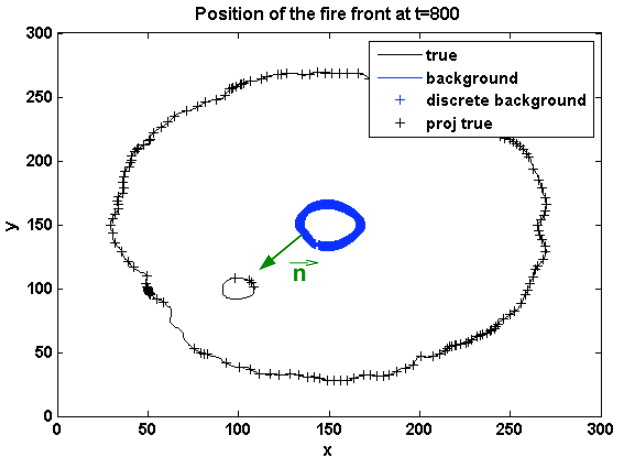

(a) Observed clasp, $\tau^t > \tau^b$.

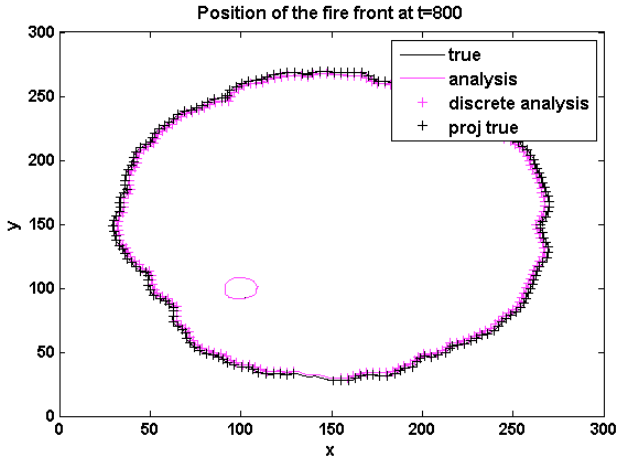

(b) Analysis after one BLUE iteration: $\tau^a \approx \tau^t$.

Figure 48: Clasp for $t = 800$ and $\tau^t > \tau^b$.

The big lake case

The calibration algorithm is also tested for a big distortion of the front due to large zone without fuel (e.g.Titicaca lake).

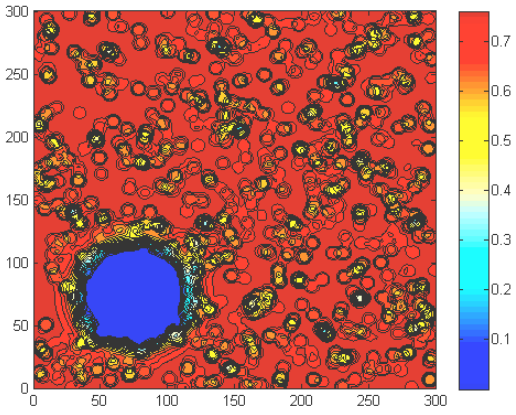

Figure 49: Random fuel distribution with big lake.

Again two configurations are tested:

1. $\tau^b > \tau^t$: $\tau^t = 0.1$ and $\tau^b = 0.19$ (+90%). The big distortion of the front curvature provoked by the big lake increases the number of point whose normal vector does not coincide with the observed front (Figure 50). However the analysis is still close to the true value: $\tau^a = 0.098$ for one BLUE iteration.

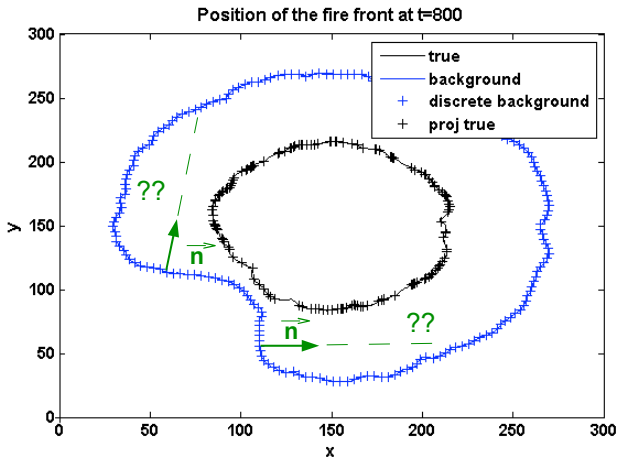

Figure 50: Big lake for $t = 800$, $\tau^b > \tau^t$.

2. $\tau^b < \tau^t$: $\tau^t = 0.19$ and $\tau^b = 0.019$ (-90%). In this situation none of the assimilation steps is affected by the strong curvature of the observed front. The analysis is close to the true value after one iteration.

The series of tests carried out is not exhaustive. Many other situations could be studied and the discretization and projection algorithm could be improved. But as long as these imperfections are not problematic for the parameter calibration, this point will not be extensively investigated.

9 Two parameter calibration

The sources of uncertainties in the Rate Of Spread determination can come from several input parameters. Also, as the ROS is determined with a semi-empirical model, some model parameters are calibrated using laboratory experiment. The extrapolation from laboratory to real case can also provide errors in the ROS determination.

First a study is performed to evaluate the sensitivity of the rate of spread to input and model parameters. Once the most influent parameters are designated, the BLUE algorithm is applied for their calibration.

Two input parameters are calibrated. Then both an input parameter and a wind dependence model parameter, C_f, experimentally fitted, are calibrated together.

9.1 Sensitivity study

9.1.1 Sensitivity to input parameters: fuel makeup

The rate of spread highly depends on local conditions and, particularly, the vegetation characteristics play an important role in its determination. Namely, the moisture content M_f and the surface-area-to-volume ratio σ are two of the most influent parameters on the ROS constant of proportionality τ (graphically the slope of R). Some maps of vegetation humidity can be obtained thanks to airborne observations [Mer09] but the surface-area-to-volume ratio is difficult to characterize, and therefore uncertain, as it quantifies the particle size. Figure 51 and Figure 52 show the sensivity of τ, and consequently the sensitivity of the ROS R, to these parameters under a constant wind condition $U = 1.4m.s^{-1}$.

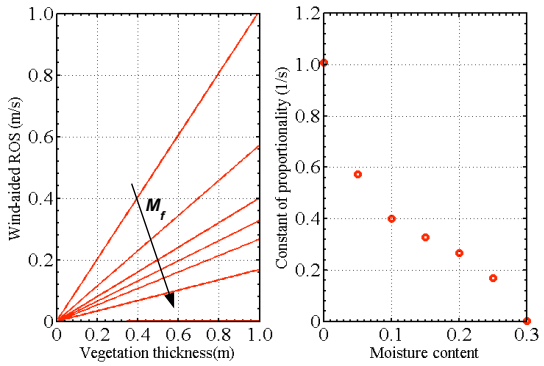

Figure 51: Influence of the moisture content M_f on the rate of spread and on τ.

The moisture content is an essential parameter in the ROS determination as it reaches a limit value for which the fire spread is stopped. Indeed the higher the humidity is, the slower the propagation will be. This value, denoted by M_X, is called the moisture of extinction. In Rothermel's model $M_X = 0.3$ for any type of fuel.

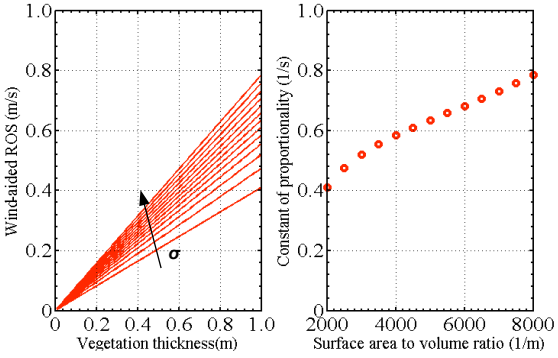

Figure 52: Influence of the surface-area-to-volume ration σ on the rate of spread and on τ.

The surface-area-to-volume ratio is used to quantify the particle size. If the surface area is larger than the volume, the particle are thinner and are more likely to be involved in the ignition process. Therefore, as σ increases, the rate of spread increases.

As M_f is highly influent on the ROS and σ can be an important source of uncertainties, these two parameters need to be calibrated.

9.1.2 Sensitivity to a model parameter: wind coefficient

In Rothermel's formulation the rate of spread depends on the wind amplitude along the normal to the front U. The wind dependence ϕ_w is given by several input parameters (fuel compactness β and surface-area-to-volume ratio σ), but also by model coefficients experimentally calibrated. In broad outline ϕ_w reads

$$\phi_w = C_f \times A(\beta, \sigma) U^{B(\sigma)}$$

where

- U: the wind amplitude along the normal to the front
- $A(\beta, \sigma)$: is a coefficient depending on the fuel makeup;
- $B(\sigma)$: is a wind exponent depending on the surface-area-to-volume ratio σ
- C_f: is a constant experimentally fitted by Rothermel with a fixed value $C_f = 7.47$.

Figure shows the influence of C_f on the rate of spread.

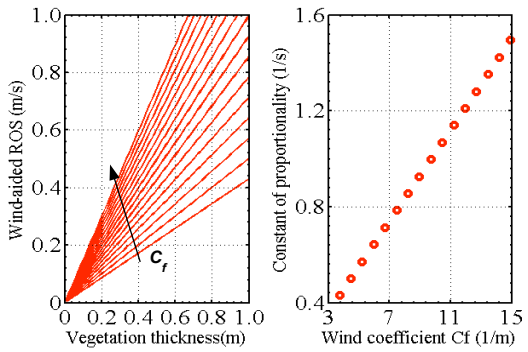

Figure 53: Influence of the wind coefficient C_f on the rate of spread and on τ.

As explained in Section 3.3.1, the 2D extrapolation is a source of error in the ROS determination. Notably, the constant $C_f = 7.47$, fitted with 1D experiments, might not be valid in a 2D configuration. Also, given that ϕ_w is highly dependent on C_f, this model parameter is a good candidate for parameter calibration using data assimilation.

9.2 Calibration of two input parameters M_f and σ

9.2.1 Formalism

***Control vector* X**

The control parameter $\mathbf{X}$ is now a vector of length $n = 2$:

$$\mathbf{X} = \begin{pmatrix} M_f \\ \sigma \end{pmatrix}$$

True value $\mathbf{X}^t = \begin{pmatrix} M_f^t \\ \sigma^t \end{pmatrix}$

The true value of the moisture content is arbitrarily chosen to 10% of humidity: $M_f^t = 0.1$. And the true value of the surface-to-volume ratio is given by Rothermel's data characterizing the tall grass: $\sigma^t = 4921\, m^{-1}$.

Therefore $\mathbf{X}^t$ reads

$$\mathbf{X}^t = \begin{pmatrix} 0.1 \\ 4921 \end{pmatrix}.$$

Background value $\mathbf{X}^b = \begin{pmatrix} M_f^b \\ \sigma^b \end{pmatrix}$

The background values are defined as a mesh in the control parameter space (the percentages in parentheses represent the relative distance to the true value) :

$$0.4M_f^t = 0.04 \leq M_f^b \leq 1.6M_f^t = 0.16 \text{ i.e. (-60\%,+60\%)}$$

this range of values corresponds to the most varying interval of $\tau = \tau(M_f)$ in Figure 51;

$$0.4\sigma^t = 1968 \leq \sigma^b \leq 1.6\sigma^t = 7874 \text{ i.e. (-60\%,+60\%)}$$

this range of values corresponds to the interval of the sensivity study $\tau = \tau(\sigma)$ in Figure 52.

Error modeling

Background error covariance matrix $\mathbf{B}$

The background error standard deviation σ_b is a vector of length $n = 2$:

$$\sigma_b = \begin{pmatrix} \sigma_{b,M_f} \\ \sigma_{b,\sigma} \end{pmatrix} = \begin{pmatrix} M_f^b - M_f^t \\ \sigma^b - \sigma^t \end{pmatrix}.$$

The background errors are supposed to be uncorrelated. The background error covariance matrix $\mathbf{B}$ therefore reads

$$\mathbf{B} = \begin{pmatrix} \sigma_{b,M_f} & 0 \\ 0 & \sigma_{b,\sigma} \end{pmatrix}.$$

Observation error covariance matrix $\mathbf{R}$

The observation error covariance matrix is assumed to be diagonal (observation errors are not correlated) and every observation is given the same uncertainty σ_o. Therefore $\mathbf{R}$ reads

$$\mathbf{R} = \begin{bmatrix} \sigma_o^2 & & \\ & \ddots & \\ & & \sigma_o^2 \end{bmatrix} = \sigma_o^2 \mathbf{I}_p$$

where,

- $\mathbf{I}_p$ is the $p \times p$ identity matrix;
- p : is the number of observations.

Linear tangent calculation $\mathbf{H}$

As both control parameters are assumed to have uncorrelated errors, the linearization of H is separated into two independent computations, one for the perturbation of M_f, another for the perturbation of σ, while the other control parameter stays fixed. So the new linear tangent of observation operator has two columns, one column per control parameter, with $\mathbf{H} = [\mathbf{H}_{M_f}; \mathbf{H}_\sigma]$:

$$\mathbf{H}_{M_f} = \frac{H(M_f + \delta M_f, \sigma) - H(M_f, \sigma)}{\delta M_f}$$

and

$$\mathbf{H}_\sigma = \frac{H(M_f, \sigma + \delta\sigma) - H(M_f, \sigma)}{\delta\sigma}.$$

9.2.2 Assimilation configuration

The simulations are run on the same computationnal domain $\Omega = [0;200] \times [0;200]$ with the same mesh and the same integration time step. The initial fire is a semi-circle of radius $r = 5$, starting at $x = 100$ and $y = 0$.

The observation set is defined in Table 12.

Observations	Number of obs. points along the front	Time-frequency	Total observations
Front	$N_p = 200$	$f_t = 50$	$2 \times 200 \times 16 = 6400$

Table 12: Observation set.

9.2.3 Calibration with no-wind, no-slope conditions

A series of tests is carried out with the previous set up in the context of OSSE under no-wind no-slope conditions. Both a uniform and a random fuel distribution are tested. The true value is given by

$$\mathbf{X}^t = \begin{pmatrix} M_f^t & \sigma^t \end{pmatrix} = \begin{pmatrix} 0.1 & 4921 \end{pmatrix}.$$

Some results for a random fuel distribution are collected in Table 13. The percentages in parentheses represent the relative distance to the true value $\begin{pmatrix} M_f^t & \sigma^t \end{pmatrix}$.

Background $\mathbf{X}^b = \begin{pmatrix} M_f^b & \sigma^b \end{pmatrix}$	Analysis $\mathbf{X}^a = \begin{pmatrix} M_f^a & \sigma^a \end{pmatrix}$	RMS(OMB)	RMS(OMA)
$\begin{pmatrix} 0.04 & 1968 \end{pmatrix}$(-60%,-60%)	$\begin{pmatrix} 0.027 & 2975 \end{pmatrix}$(-73%,-40%)	2.94	0.117
$\begin{pmatrix} 0.08 & 5905 \end{pmatrix}$(-20%,+20%)	$\begin{pmatrix} 0.065 & 4036 \end{pmatrix}$(-35%,+18%)	2.38	0.117
$\begin{pmatrix} 0.16 & 1968 \end{pmatrix}$(+60%,-60%)	$\begin{pmatrix} 0.223 & 8039 \end{pmatrix}$(+123%,+64%)	4.46	0.120
$\begin{pmatrix} 0.16 & 7874 \end{pmatrix}$(+60%,+60%)	$\begin{pmatrix} 0.166 & 6177 \end{pmatrix}$(+66%,+25%)	2.24	0.115

Table 13: Calibration results for random fuel distribution.

In the control parameter space, the analysis is most of the time farther to the true value than the background value. Whereas in the observation space, the analysed front is always closer to the observations (here the true front) than the background: RMS(OMA) < RMS(OMB).

Given that the ROS depends linearly on the fuel depth δ, $R = \tau\delta$, finding an analysis matching the observed front is equivalent to finding an analysis leading to the same value of the constant of proportionality τ. Therefore the BLUE algorithm is implicitly solving the equation, *centeris paribus*,

$$\tau(M_f, \sigma) = \tau(M_f^t, \sigma^t) \tag{79}$$

which presents an infinity of solutions (see Figure 54).

Indeed equation (79) is an undetermined problem with one equation and two unknowns.

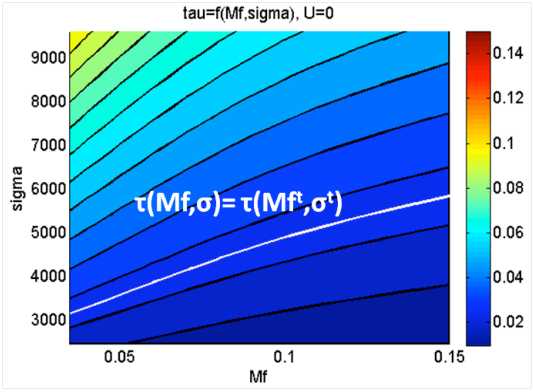

Figure 54: $\tau(M_f, \sigma)$ for no-wind conditions ($U = 0$). The white line represent the solutions of equation (79).

Therefore when searching for the minimum of J_{BLUE}, the BLUE algorithm finds the closest solution to the background in the direction of the linearization steps $(\delta M_f, \delta\sigma)$ which provides the same value of τ as $\tau(M_f^t, \sigma^t)$:

$$\tau(M_f^a, \sigma^a) = \tau(M_f^t, \sigma^t)$$

and

$$(M_f^a, \sigma^a) \neq (M_f^t, \sigma^t)$$

Figure 55 shows an example of an analysed front matching the true front with $(M_f^a, \sigma^a) \neq (M_f^t, \sigma^t)$

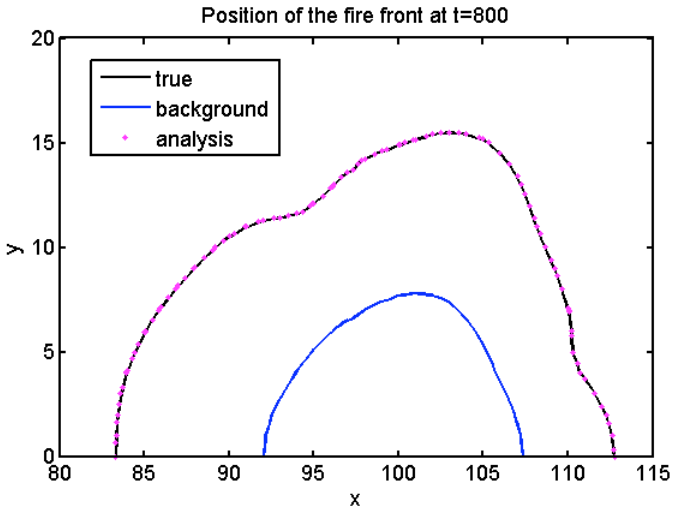

Figure 55: $\tau(M_f^a, \sigma^a) = \tau(M_f^t, \sigma^t) = 0.027$ and $(M_f^a, \sigma^a) = (0.02, 2974) \neq (M_f^t, \sigma^t) = (0.1, 4923.1)$

This behavior can be understood by visualizing the cost function $J_{3DVAR}(M_f, \sigma)$. As shown on Figure 56, the minima of $J_{3DVAR}(M_f, \sigma)$ coincides with the solutions of equation (79).

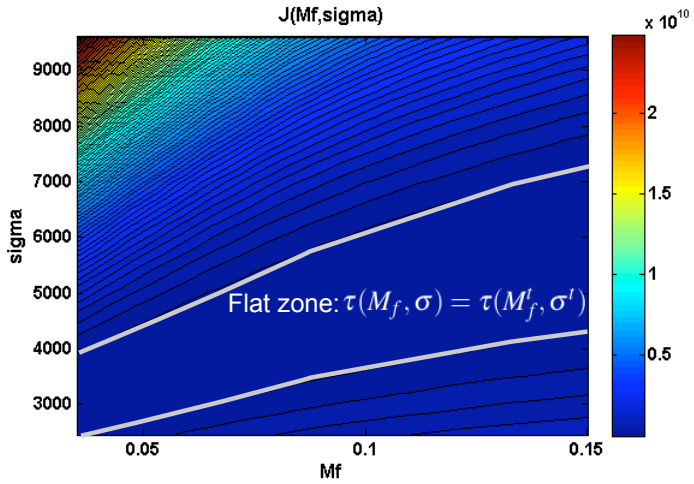

Figure 56: $J_{3DVAR}(M_f, \sigma)$

This multiple solution problem is also encountered for a uniform fuel distribution.

9.2.4 Calibration with wind-aided, no-slope conditions

A series of tests is carried out with a wind condition $\vec{V} = \begin{pmatrix} 0 \\ 0.5 \end{pmatrix} m.s^{-1}$ for a uniform and a random fuel distribution.

Table 14 collects the calibration results for a uniform fuel distribution.

Background $\mathbf{X}^b = \begin{pmatrix} M_f^b & \sigma^b \end{pmatrix}$	Analysis $\mathbf{X}^a = \begin{pmatrix} M_f^a & \sigma^a \end{pmatrix}$	RMS(OMB)	RMS(OMA)
(0.04 1968)(-60%,-60%)	(0.1 4921)(0%,0%)	11.4	0.04
(0.08 5905)(-20%,+20%)	(0.1 4919)(0%,0%)	3.55	0.04
(0.16 1968)(+60%,-60%)	(0.1 4921)(0%,0%)	5.92	0.04
(0.16 7874)(+60%,+60%)	(0.1 4916)(0%,-0.1%)	3.31	0.04

Table 14: Calibration results for random fuel distribution.

Contrary to no-wind condition, the analysis $\mathbf{X}^a$ matches perfectly the true value both in the parameter space and in the observation space. This behaviour can be explained by the addition of the wind condition. Indeed wind addition can be interpreted as a new restrictiction in the minimization problem. The time- and space-dependence of U introduces a time- and space-dependence in the expression of τ (cf. Section 3.3.1) whereas this quantity was constant for no-wind condition.

By deleting one degree of freedom in equation (79) the minimum of J_{3DVAR} is unique.

A more extensive work should be undertook to explain formally and completely with equations how the wind addition reduces the number of degree of freedom in equation (79).

The calibration behaviour is similar for a random fuel distribution. However the inhomogeneities in the vegetation slow the calibration process and the convergence is not always satisfied for background values far from the true value, typically (-60%,-60%). A change in the linearization step would probably improve the calibration performances for such sensitive cases.

9.3 Calibration of one input parameter M_f and one model parameter C_f

9.3.1 Calibration with wind-aided, no-slope conditions

The couple of parameters $\mathbf{X} = \begin{pmatrix} M_f \\ C_f \end{pmatrix}$ is calibrated with the same conditions and assimilation configuration. The true value of the moisture content is arbitrarily chosen to 10% of humidity: $M_f^t = 0.1$. And the true value of the wind coefficient is given by Rothermel's model: $C_f^t = 7.47$. Therefore $\mathbf{X}^t$ reads

$$\mathbf{X}^t = \begin{pmatrix} 0.1 \\ 7.47 \end{pmatrix}$$

As C_f can only be calibrated with a wind condition (otherwise it would not influence the ROS), the multiple solution problem does not appear in this case and the calibration performances are similar to the calibration of (M_f, σ) under wind condition:

- Efficient and accurate with a uniform fuel distribution;
- Slow but mostly consistent with a random fuel distribution.

9.4 Discussion

This section proves the feasibility of multiple parameter calibration. It also highlights some interesting assets of this technique. As both input and model parameters can be calibrated the data assimilation algorithm allows not only to adjust front positions by correcting input parameters but also gives a better fit of experimentally calibrated parameters and therefore improve the model itself.

10 Toward a real case application

The context of Observation System Simulation Experiments is a good validation framework. Once the robustness of the algorithm is proven, the calibration prototype must be validated with real observations.

As a first step, the algorithm can be tested by generating observations and background trajectory with different models.

Then, the data assimilation process is applied to real experimental data.

10.1 Parameter calibration using imperfect model

10.1.1 Framework

In this framework , the model to determine the rate of spread is supposed to be different to Rothermel's. Rothermel's model is still used to synthesized observations whereas the background rate of spread model does not depend linearly on the normalized fuel depth

$$R^b(x,y) = \tau^b \bar{\delta}(x,y)^n$$

with $n \neq 1$ ($n = 1$ for Rothermel's formulation).

This means that the background trajectory cannot stick completely to the observations as it does not result from the same description of the fire physics.

10.1.2 Results

The mesh and the time step are unchanged. The initial conditions are described on Figure 57.

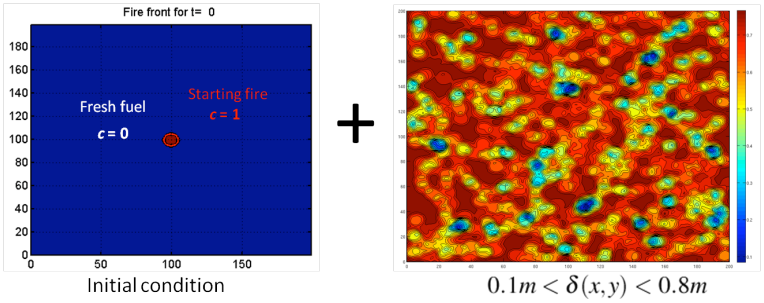

Figure 57: Initial condition with random fuel vegetation.

The true value of the constant of proportionality τ is unchanged: $\tau^t = 0.1$. The background is prescribed a fixed value:

$$\tau^b = 0.15\,(+50\%)$$

As series of test is carried out in the context of OSSE. Observations are granted a high level of confidence with the same assimilation configuration for different values of n in the background model. Results are shown in Figure 58.

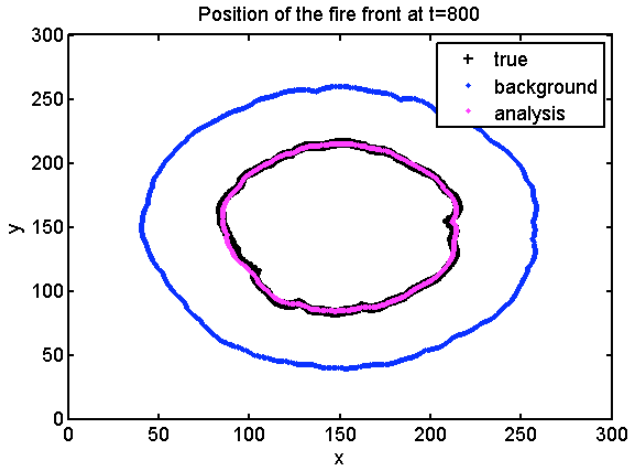

(a) Result for $n = 0.5$, $\tau^a = 0.0865$.

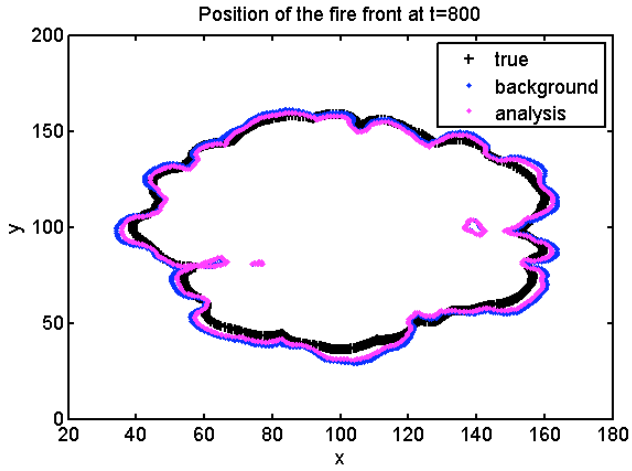

(b) Result for $n = 2$, $\tau^a = 0.146$.

Figure 58: Results for two different models: $n = 0.5$ and $n = 2$.

The results show that the BLUE algorithm manages to stick as close as possible to the observations whatever is the model used. When $n = 2$, the ROS is highly dependent on the fuel depth fluctuations and thus the front curvature is more variable than the observed front. On the opposit when $n = 0.5$, the front curvature is almost constant.

For both case the data assimilation process minimizes the mean distance to the true value by calibrating the parameter value.

10.1.3 Discussion

This proof-of-concept shows that the calibration technique is also efficient out of the OSSE context when using different models for observation generation and background trajectory. The next logical step is the application of the data assimilation algorithm to real experimental data.

10.2 Input parameter calibration using real experimental data

In this section real experimental observations provided by Ronan Paugam[6] are used to calibrate Rothermel's input parameters (M_f, σ).

10.2.1 Data description and numerical configuration

An experimental grassfire spread was filmed using an infrared camera. The resulting observations are front positions. A prior data treatment was performed to adapt the observations to the numerical requirements and to the assimilation framework (cf. Appendix B). All the experimental conditions are depicted in Table 15.

Grass height	Moisture content	Wind vector $\vec{V}$	Domain size	Time of spread	Number of frames
$\approx 8\,cm$	$M_f = 21.7\%$	$\alpha = (\vec{V}, Oy) = 307°$ $\left\|\vec{V}\right\|_2 = 1.3\,m.s^{-1}$	$\approx 4\,m \times 4\,m$ $= 90 \times 85$ pixels	$\approx 350\,s$	1347

Table 15: Experimental conditions.

From Table 15, the numerical configuration is defined so as to have an equivalent resolution to the camera's and a time step respecting the CFL condition (Table 16).

[6]Research associate in the Department of Geography, King's College London: *http://wildfire.geog.kcl.ac.uk/index.php/ronan*

Domain size	Discretization	Time step	Fuel distribution
$4\,m \times 4\,m$	$dx = dy = 4.7\,cm$	$dt = 0.02$	Homogeneous: $\delta(x, y) = 0.08\,m$

Table 16: Numerical configuration.

10.2.2 Assimilation configuration

Observation set

As a first step the calibration algorithm is tested using only one front observation. Only two frames are extracted from the data:

1. The first one defines the initial condition at $t = 0$: $c_0(x, y)$;

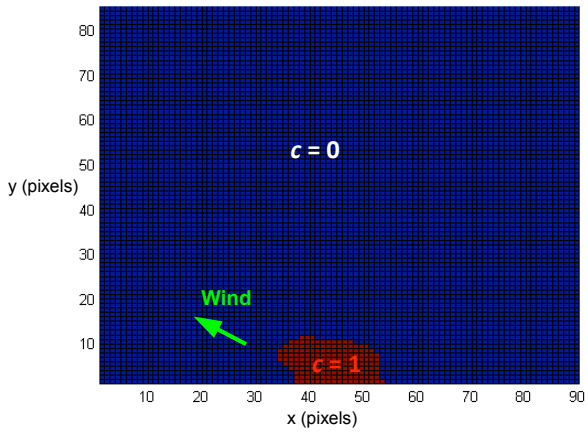

Figure 59: First frame: initial condition $c_0(x, y)$.

2. The second and last one contains $\mathbf{Y}^o$, the front positions to compare the simulations with.

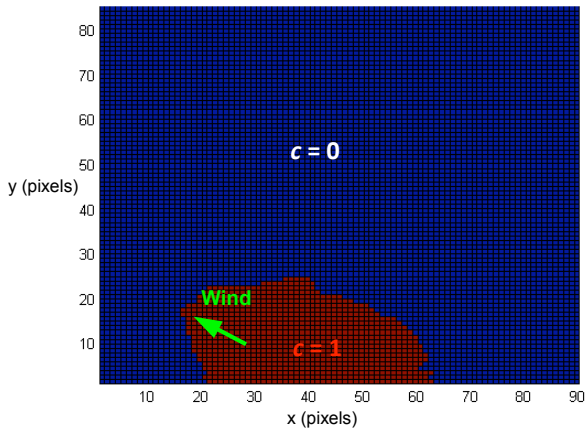

Figure 60: Second frame: $\mathbf{Y}^o$is the discretized boundary of the surface $c = 1$.

The time frequency between two observations is arbitrarily chosen to 100 frames. So the second frame provides the front positions at $t = 27\,s$.

The number of observation points along the front is fixed to 200:

$$N_p = 200$$

So the total number of observations p is

$$p = 1 \times 200 = 200$$

Formalism

Control vector $\mathbf{X} = \begin{pmatrix} M_f \\ \sigma \end{pmatrix}$

Out of the context of OSSE there is no true value but only the parameter estimation (background value) and the observations to correct it.

The background value is a first guess of $\begin{pmatrix} M_f & \sigma \end{pmatrix}$. The estimation of σ is provided by Rothermel's description of tall grass $\sigma^b = 4921\, m^{-1}$. The estimation of M_f is given by experimental measures collected in Table 15: $M_f^b = 0.217$.

Thus $\mathbf{X}^b$ reads

$$\mathbf{X}^b = \begin{pmatrix} M_f^b \\ \sigma^b \end{pmatrix} = \begin{pmatrix} 0.217 \\ 4921 \end{pmatrix}$$

Observation errors

As the discretization step is equal to the camera's resolution ($4.7\, cm$), the uncertainty on the observations is prescribed a value equal to the discretization step:

$$\sigma_o = dx = 0.047\, m$$

Again, the observation errors are assumed to be uncorrelated. Therefore the observation error covariance matrix reads

$$\mathbf{R} = 0.047^2 \mathbf{I}_p$$

Background error

The background error is difficult to estimate. The uncertainty on the measured moisture content M_f needs to be evaluated from the measurement devices. And the surface-area-to-volume ratio σ has been estimated only for one type of grass which might not be correctly describing the grass burnt during the experiment. Also, the uncertainty of this Rothermel's estimation is unknown.

So, the background is arbitrarily prescribed an uncertainty of 30% its value:

$$\sigma_b = 0.3\mathbf{X}^b = \begin{pmatrix} 0.065 \\ 1476 \end{pmatrix}$$

The determination of the standard deviation σ_b is not really important in this assimilation configuration. As the number of observations is greater than the number of parameters to calibrate ($p = 200 \gg n = 2$) and the observation error is small ($\sigma_o = 0.047$), the observations will be predominant whatever the background uncertainty is :

$$J^o_{3DVAR} \gg J^b_{3DVAR}$$

(cf. Section 6.7).

The background error covariance matrix therefore reads

$$\mathbf{B} = \begin{pmatrix} 0.065^2 & 0 \\ 0 & 1476^2 \end{pmatrix}$$

Table 17 summarizes the assimilation configuration.

Type of obs.	Assim. window	Number of obs.	Obs. uncertainty	Background $\left(M_f^b\ \sigma^b\right)$	Bck.uncertainty
Front	$[0\, s; 27\, s]$	$p = 1 \times 200$	$\sigma_o = 0.047$	(0.217 4921)	$\sigma_b = (0.065\ 1476)$

Table 17: Assimilation configuration.

10.2.3 Results

The numerical simulation is run for $27\,s$ and then compared with the front described in Figure 60. The resulting analysis after eight BLUE iterations reads

$$\mathbf{X}^a = \begin{pmatrix} M_f^a \\ \sigma^a \end{pmatrix} = \begin{pmatrix} 0.15 \\ 14619 \end{pmatrix}$$

Out of the OSSE context, no diagnostic in the control parameter space can be performed. A physical analysis reveals that while the analysed moisture content M_f^a is still in a "physical" range of values ($M_f^a \in [0; M_X]$), the analysed surface area to volume ratio σ^a is out of physical range. Usually σ varies from $2000\,m^{-1}$ to $8000\,m^{-1}$ depending on the type of vegetation.

However in the observation space the analysed front is closer to the observed front (see Figure 62).

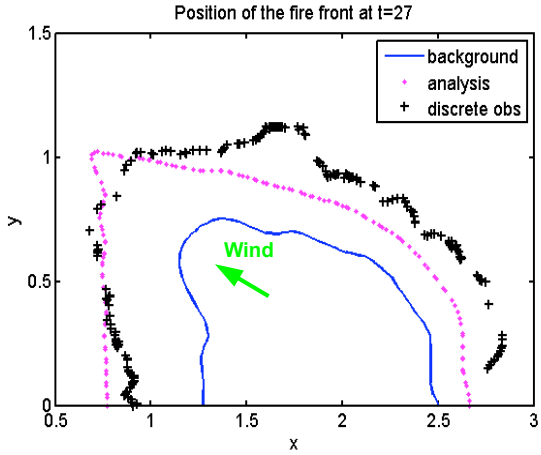

Figure 61: Background correction in the observation space.

10.2.4 Discussion

The calibration algorithm is consistent as the analysed front is closer to the observed front; but the parameter correction is out of physical range. Figure 62 shows that the background front underestimates the rate of spread. That is why the correction "accelerates" the front by diminishing the moisture content and increasing the surface area to volume ratio (cf. Section 9.1). However the errors on the modeled rate of spread do not only come from the two parameters M_f and σ:

- In addition to model fidelity errors, the 2D extrapolation leads to new uncertainties as Rothermel's model is designed for 1D configurations.
- Many other input and model parameters are uncertain:
  - Figure 62 clearly shows that the vegetation distribution is not strictly homogeneous;
  - the wind might not be constant. It might be space- and time-dependent;
  - ...

A change in one of the input parameters can indeed affect the calibration result. For example, by changing the fuel depth from $\delta = 8\,cm$ to $\delta = 14\,cm$, the background front is closer to the observed front and therefore, the corrected parameters $\mathbf{X}^a = \begin{pmatrix} M_f^a & \sigma^a \end{pmatrix}$ are closer to a "physical" value (see Figure 62)

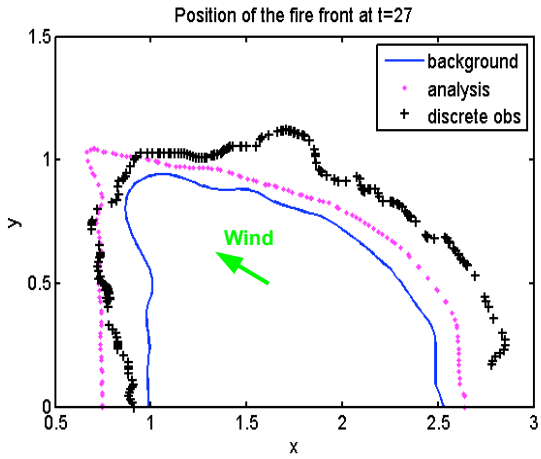

Figure 62: Background correction in the observation space. $\mathbf{X}^a = (0.22\ 11895)$.

However, as a first test using real experimental data with only one picture of front position, the results are encouraging. In order to improve the calibration results, a further study should focus on several aspects:

- set a real assimilation configuration by extending the assimilation window and diminishing the observation time-frequency (not only one frame);
- obtain more precise data about the experimental conditions and the fuel makeup to diminish some input parameter uncertainty;
- integrate the model with the resulting analysis ($\mathbf{X}^a$) at the end of the assimilation window $[0; t_f]$ to predict the trajectory of the fire front further in time ($t > t_f$). The predictions of the positions of the fire fronts further in time are called forecast. They will be compared with the future observations to check if and how the model deviates from the true trajectory and to establish a frequency of data assimilation to avoid a too large deviation.

Conclusions

Forecasting the behaviour of existing wildfires requires a degree of sophistication that the current models and our knowledge of fuels do not permit. However, this study has shown that data assimilation opens the possibility of predicting fires by reducing the forecast uncertainties.

Since Mélanie Rochoux's previous work [Roc10], some advances have been made both in the fire spread model and in the calibration algorithm.

At a regional scale, the Level-Set method presents strong assets for front propagation such as stability and accuracy for any configuration. However, at a local scale, the Rothermel's model shows its limits when considering 2D wind-aided configurations.

The data assimilation strategy has been improved on several aspects. First, by overcoming non-linearity impact, the external loop implementation allows parameter calibration with important background errors. Secondly, cost functions provide a better understanding of the calibration algorithm behaviour. Thirdly, the assimilation strategy associated with front observations is much more efficient than field assimilation for similar configurations. Lastly, two parameter calibrations provide good results as long as physical restrictions lead to a unique solution.

In order to improve the fire spread model, the use of a semi-empirical valid for 2D wind-aided configurations, such as Fendell and Wolff's [FW01], would avoid an approximative 2D extrapolation. On the long run, a physical model designed by Mélanie Rochoux should provide a better rate of spread estimation for any configuration.

Concerning data assimilation, the technique itself has to be improved. Notably

- keep observation points equidistant along the front, whatever is the length of its perimeter. This involves a dynamic change in the number of discretization points along the modeled fronts:

$$N_p = N_p(t).$$

- calibrate more than two parameters. But as shown in this study, if the number of parameters to calibrate is higher than the number of physical restrictions, the rate of spread equation leads to a multiple solution problem. However, tests should be carried out to see if the wind condition enables the calibration of more than two parameters...

- change the assimilation technique from BLUE to Ensemble Kalman Filter. This technique was first introduced by Evensen [Eve94][7]. It is now widely used for data assimilation, and notably for Lagrangian data (i.e. positions) [KIJ03]. It is known to be efficient when the number of state variables to correct is high: $n \gg 1$. So, the use of the Ensemble Kalman Filter would allow to assimilate both parameters and front positions. This way the control vector $\mathbf{X}$ would read:

$$\mathbf{X} = \begin{pmatrix} \text{Param}_1 \\ \vdots \\ \text{Param}_n \\ \text{Position}_1 \\ \vdots \\ \text{Position}_{N_p} \end{pmatrix}.$$

  By adding front positions in the control vector, the precision of the parameter correction would be enhanced.

Many work remain to do to make this technique fully operational. But, collaborations and knowledge sharing between different scientific communities such as firefighting, wildfire, combustion, data assimilation, climate, remote detection and image processing should enhance the research productivity in this field. For instance, in France, the Departmental Service of Fires and Assistance (SDIS) of Oriental Pyrenees, a public departmental establishment under the juridiction of the Ministry of Internal Affairs, uses an automated real-time geolocation system for wildfire fighting operations, called Livefire (www.livefire.aero). This tool aboard an aircraft system provides real-time thermal-infrared data, from which can be extracted the fire front positions [Cro10]. This type of data could be incorporated into a data assimilation system to obtain more accurate predictions of wildfire spread.). Hopefully this wide project will succeed in providing an efficient fire protection tool...

[7] A comprehensive theoretical presentation of the Ensemble Kalman Filter and its numerical implementation is provided in [Eve03].

Perspectives

"Don't be late for your fate."

Magic Hat.

This internship has been an exciting multidisciplinary project. Being at the interface between different scientific communities and interact with different research teams in different languages was a great profesionnal challenge and a rewarding personal experience.

It was also a deeper step in the research community. The former work conducted by Mélanie Rochoux [Roc10] has been presented in a poster session during the 10th International Symposium on Fire Safety Science at the University of Maryland, from 19 to 24 June 2011. Presenting this work to the fire scientific community and attending several talks on the subject was a great opportunity. Also the contribution of this internship has led to the writing of an article in a scientific journal.

Since my third year at the INSA Toulouse, I have been willing to pursue my studies with a Ph.D. My fourth year internship at HydroSciences Montpellier resulted with a poster publication at the European Geosciences Union General Assembly from 3 to 8 April 2011 in Vienna, and the writing of an article is now ongoing.

The coming year I will start a Master Degree in Fluid Mechanics applied to Geosciences and Biophysics at the *Université Paul Sabatier* in Toulouse. This training matches my strong interest in Mathematics, Geosciences and Biophysics and will strengthen my knowledge in these fields. Above all, it will allow me to meticulously look for a Ph.D. that correponds to my professional ambitions and personal expectations.

References

[Alb85] F.A. Albini. A model for fire spread in wildland fuels by radiation. *Combustion Science and Technology*, Vol. 42:pp 229–258, 1985.

[BA05] J. A. Bærentzen and H. Aanæs. Signed distance computation using the angle weighted pseudo-normal. *IEEE Transactions on Visualization and Computer Graphics*, Vol. 11:pp 243–253, 2005.

[BC99] F. Bouttier and P. Courtier. *Data assimilation concepts and methods*, March 1999.

[BMS+09] J.H. Balbi, F. Morandini, X. Silvani, J.B. Filippi, and F. Rinieri. A physical model for wildland fires. *Combustion and Flame*, Vol. 156:pp 2217–2230, 2009.

[BV06] P. Brasseur and J. Verron. *The SEEK filter method for data assimilation in oceanography: a synthesis.* Springer Berlin / Heidelberg, 2006.

[CGC98] N.P. Cheney, J.S. Gould, and W.R. Catchpole. Prediction of fire spread in grasslands. *International Journal of Wildland Fire*, Vol. 8:pp 1–13, 1998.

[CK07] K.N. Chaudhury and K.R.Ramakrishnan. Stability and convergence of the level set method in computer vision. *Pattern Recognition Letters*, Vol. 28:pp 884–893, 2007.

[CMD+10] R. Chabiniok, P. Moireau, J.F. Deux, P.F. Lesault, A. Rahmouni, and D. Chapelle. Estimation of tissue contractility from cardiac cine-mri using biomechanical heart model. 2010.

[Cro10] P. Crombette. Optimisation et poursuite des développements du système livefire de géolocalisation automatisée et temps-réel de prises de vues aéroportées. Technical report, Université de Toulouse, 2010.

[Del10] B. Delmotte. Etude hydrodynamique des contaminants dans les lagunages. Technical report, Hydro-Sciences Montpellier, 2010.

[Dup97] J.L. Dupuy. An analysis of semi-empirical and physical models for fire spread in wildland fuels. In *Wildfire Management*, 1997.

[Eve94] G. Evensen. Sequential data assimilation with a non-linear quasi-geostrophic model using monte carlo methods to forecast error statistics. *Journal of Geophysical Research*, Vol. 99:pp 10,143–10,162, 1994.

[Eve03] G. Evensen. The ensemble kalman filter: theoretical formulation and practical implementation. *Ocean Dynamics*, Vol. 53:pp 343–367, 2003.

[FMB09] J.B. Filippi, F. Morandini, and J.H. Balbi. Discrete event front-tracking simulation of a physical fire-spread model. *SIMULATION*, OnlineFirst, 2009.

[Fon46] W.L. Fons. Analysis of fire spread in light forest fuels. *Journal of Agricultural Research*, Vol. 72, 1946.

[Fra71] W.H. Frandsen. Fire spread through porous fuels from the conservation of energy. *Combustion and Flame*, Vol. 16:pp 9–16, 1971.

[FW01] F.E. Fendell and M.F. Wolff. *Forest Fires - Behavior and Ecological Effects*, chapter Wind-aided fire spread, pages 171–223. Academic Press, 2001.

[ICGL97] K. Ide, P. Courtier, M. Ghil, and A.C. Lorenc. Unified notation for data assimilation: operational, sequential and variational. *Journal of the Meteorological Society of Japan*, Vol. 75:pp 181–189, 1997.

[Jah10] W. Jahn. *Inverse Modelling to Forecast Enclosure Fire Dynamics.* PhD thesis, University of Edinburgh, 2010.

[Kal03] E. Kalnay. *Atmospheric Modeling, Data Assimilation and Predictability.* 2003.

[KAW88] A. Kernstein, W. Ashurst, and F. Williams. Field equation for interface propagation in an unsteady homogeneous flow field. *Physical Review*, Vol. 37:pp 2728–2731, 1988.

[KIJ03] L. Kuznetsov, K. Ide, and C.K.R.T. Jones. A method for assimilation of lagrangian data. *Monthly Weather Review*, Vol. 131:pp 2247–2260, 2003.

[Lel92] S.K. Lele. Compact finite difference schemes with spectral-like resolution. *Journal of Computational Physics*, Vol. 103:pp 16–42, 1992.

[Mac66] A.G. MacArthur. Weather and grassland fire behaviour. Technical report, Forest Research Institute Leaflet 100. Department of National Development, Forest and Timber Bureau, Canberra, CSIRO., 1966.

[MBB+08] J. Mandel, L.S. Bennethum, J.D. Beezley, J.L. Coen, C.C. Douglas, M. Kim, and A. Vodacek. A wildfire model with data assimilation. *Mathematics and Computers in Simulation*, pages pp 584–606, 2008.

[MD04] D. Morvan and J.L. Dupuy. Modeling the propagation of a wildfire through a mediterranean shrub using a multiphase formulation. *Combustion and Flame*, Vol. 138:pp 199–210, 2004.

[Mer09] N. Merlet. Géoolocalisation automatisée et temps-réel de prises de vues aéroportées dans le cadre de la lutte contre les feux de forêt. 2009.

[MKF09] V. Mallet, D.E. Keyes, and F.E. Fendell. Modeling wildland fire propagation with level set methods. *Computers and Mathematics with Applications*, Vol. 57:pp 1089–1101, 2009.

[OS88] S. Osher and J.A. Sethian. Fronts propagating with curvature-dependent speed: algorithms based on hamilton-jacobi formulations. *Journal of Computational Physics*, Vol. 79:pp 12–49, 1988.

[PD92] D.F. Parrish and J.C. Derber. The national meteorological center's spectral statistical interpolation analysis system. *Monthly Weather Review*, Vol. 120:pp 1747–1763, 1992.

[PD11] G. Puigt and H. Deniau. Cfd e-learning : Euler equations and discretization of convection. Technical report, CERFACS, 2011.

[PV05] T. Poinsot and D. Veynante. *Theoretical and Numerical Combustion, 2nd edition*. R.T. Edwards, 2005.

[Rab05] F. Rabier. Overview of global data assimilation developments in numerical weather-prediction centres. *Quarterly Journal of The Royal Meteorological Society*, Vol. 131:pp 3215–3233, 2005.

[Ric04] S. Ricci. *Assimilation variationnelle océanique : modélisation multivariée de la matrice de covariance d'erreur d'ébauche*. PhD thesis, Université Paul Sabatier - Toulouse III, March 2004.

[Ric10] S. Ricci. *Calage de paramètre sur un toy model*, February 2010.

[RJK+00] F. Rabier, H. Jarvinen, E. Kilnder, J.F Mahfouf, and A. Simmons. The e.c.m.w.f. operational implementation of four-dimensional variational assimilation. part i : Experimental results with simplified physics. *Quarterly Journal of The Royal Meteorological Society*, Vol. 126(126):pp 1143–1170, 2000.

[RM09] R.G. Rehm and R.J. McDermott. Fire-front propagation using the level set method. Technical report, National Institute of Standards and Technology, 2009.

[Roc10] M. Rochoux. Preliminary investigation of data assimilation methodologies for forest fire propagation. Technical report, Cerfacs - University of Maryland, November 2010.

[Rot72] R. Rothermel. A mathematical model for predicting fire spread in wildland fires. *USDA Forest Service*, 1972.

[Tar87] A. Tarantola. Inverse problem theory and methods for model parameter estimation. *SIAM: Society for Industrial and Applied Mathematics*, 1987.

[Thu10] O. Thual. Boucle externe sans oscillations. In *EPI-ALEZ, Échange de Projets et Idées "Assimilation de données pour le Lez"*, September 2010.

[TMM+10] G. Thirel, E. Martin, J.F. Mahfouf, S. Massart, S. Ricci, and F. Habets. A past discharges assimilation system for ensemble streamflow forecasts over france. *Hydrology and Earth System Sciences*, Vol. 14:pp 1623–1637, 2010.

[Vie98] D.X. Viegas. Forest fire propagation. *Philosophical Transactions: Mathematical, Physical and Engineering Sciences*, Vol. 356:pp. 2907–2928, 1998.

[Web91] R.O. Weber. Toward a comprehensive wildfire spread model. *International Journal of Wildland Fire*, Vol. 4:pp 245–248, 1991.